ENERGY SENSITIVE WASTEWATER TREATMENT USING INTEGRATED ANAEROBIC DIGESTION AND ADVANCED OXIDATION PROCESSES

Benton Otieno, Seth Apollo, John Akach, Janet Mabuza, George Ochieng, John Kabuba, Maurice Ndege, Ochieng Aoyi.



ENERGY SENSITIVE WASTEWATER TREATMENT USING INTEGRATED ANAEROBIC DIGESTION AND ADVANCED OXIDATION PROCESSES

Report to the

Water Research Commission

by

Benton Otieno, Seth Apollo, John Akach, Janet Mabuza, George Ochieng, John Kabuba, Maurice Ndege, Ochieng Aoyi.

Centre for Renewable Energy and Water,

Vaal University of Technology

WCR Report No. TT 813/19 ISBN 978-0-6392-0127-6

March 2020





Obtainable from

Water Research Commission Private Bag X03 GEZINA, 0031

orders@wrc.org.za or download from www.wc.org.za

DISCLAIMER

This report has been reviewed by the Water Research Commission (WRC) and approved for publication. Approval does not signify that the contents necessarily reflect the views and policies of the WRC nor does mention of trade names or commercial products constitute endorsement or recommendation for use.

© Water Research Commission

EXECUTIVE SUMMARY

In our previous study (WRC Report No. 2388/1/18; ISBN 978-1-4312-0998-9), it was shown that combined anaerobic digestion (AD) and photocatalytic treatment of industrial wastewater was effective for organic load and colour reductions and bioenergy production. The combined process, however, needed to be fully integrated, and energy, environmental and economic The study further recommended the use of simulation tools such as analyses done. computational fluid dynamics (CFD) to determine the hydrodynamics in a fluidized bed reactor for advanced oxidation processes (AOPs). Moreover, the application of an alternative AOP such as ozonolysis, which is not affected by turbidity, was found necessary. development on the findings in the previous WRC project, the aim of the current study was to integrate AD and ozonolysis for the effective treatment of distillery wastewater (DWW), and waste activated sludge (WAS); determine key optimum operating conditions, for the integrated system and carry out energy, environmental and economic analyses. The specific objectives were to: (i) apply CFD modelling to determine the optimal reactor hydrodynamic conditions, (ii) carry out an integrated anaerobic digestion and ozonolysis post-treatment of DWW, model the sludge production kinetics, and evaluate the performance of the integrated system, (iii) conduct energy, environmental and economic analyses of the integrated AD-AOP process treating DWW, and (iv) carry out an integrated ozonolysis pre-treatment and anaerobic digestion of WAS, determine the sludge disintegration mechanism and the effect of pretreatment on AD.

A fluidized bed reactor and a bubble column reactor was simulated using CFD. The phase mixing was evaluated through CFD hydrodynamic simulation of phase hold up. The simulation results were validated using experimental data. The ozonolysis process was carried out in a bubble column reactor while the anaerobic process was carried out in an upflow anaerobic sludge blanket (UASB) reactor. For the integrated processes, the ozonolysis unit either preceded or proceeded the anaerobic unit. Energy and economic analyses were evaluated from the potential application of the bioenergy produced to supplement the energy requirements of the integrated system. The environmental analysis was carried out based on the carbon dioxide emission reduction resulting from the use of renewable bioenergy instead of energy from the grid. The mechanism of sludge solubilization was determined from the release of nutrients such as proteins and carbohydrates into the supernatant, and by thermogravimetric and Fourier Transform Infrared analyses.

CFD simulations of the fluidized bed reactor showed that the radial variation of the catalyst loading was not significant. For instance, the difference between the highest and lowest solid holdup was only 4%. The axial variation of the solid holdup along the column was also observed to be insignificant since the catalyst was nanoparticulate in nature and could be easily fluidized in the reactor. Consequently, an assumption of uniform catalyst distribution in the reactor can be made.

The treatment of DWW using integrated AD and ozonolysis resulted in AD alone achieving a high reduction (75%) of chemical oxygen demand (COD) but with a considerable increase in the colour intensity of the digester effluent. Ozonolysis post-treatment effectively removed up to 80% of the biorecalcitrant colour and solubilized 80% of the sludge washed out from the anaerobic unit. From the kinetics study, the rate of COD degradation in the initial anaerobic digestion step was found to be 15 times slower than the ensued ozonolysis process. For a constant feed flow integrated system consisting of an anaerobic digester and a bubble column ozone reactor, the ratio of the AD reactor unit to the ozonolysis reactor unit is recommended to be 20:1. The total bioenergy produced from the anaerobic process, when converted to electricity, can adequately meet the energy requirement of the ozonolysis process. Moreover, application of the bioenergy to supplement the total energy requirement of the integrated system can lead to 50% savings on energy from the grid, and a carbon dioxide emission reduction of $122 \text{ kg CO}_2/\text{m}^3$.

For WAS treatment, ozonolysis was first applied as a pre-treatment followed by AD. WAS pre-treatment, through the rapture of hard cell walls, solubilized the extracellular polymeric substances, thereby releasing the biodegradable cellular contents. The soluble chemical oxygen demand (COD) increased by 35%, with a corresponding 58% increase in dissolved organic carbon (DOC). Also, the BOD₅:COD ratio significantly improved by 160%, confirming improved biodegradability. In the ensuing AD process, WAS pre-treatment led to improved reduction of the total suspended solids and COD and a 230% increase in the cumulative biogas production. In the integrated ozonolysis-anaerobic treatment, ozone pretreated WAS produced 0.21 L biogas/g feed COD while non-pretreated WAS produced 0.059 L biogas/g feed COD.

Overall, the study has established that the bed was homogeneous and that an integrated AD-ozonolysis system can be effective for the treatment of WAS and DWW with a potential bioenergy recovery. The configuration of the AD-ozonolysis process is, however,

substrate-specific with ozonolysis best applied as a pre-AD and post AD for WAS and DWW, respectively. For practical applications, the ozonolysis treatment unit can be retrofitted in existing treatment systems either before the AD unit for WAS or after the AD unit for DWW.

ACKNOWLEDGMENTS

We acknowledge the support, advice, and stimulating discussions, initiated by the Reference Group. Your invaluable contribution and dedication to the project enabled us to achieve our goals.

Reference group

Dr John Ngoni Zvimba Water Research Commission (Chairperson)

Dr Rembu Magoba City of Cape Town

Mr James Topkin Ekurhuleni Water Care Company

Prof. Stephen Ojwach University of KwaZulu-Natal

Dr Taile Leswifi Vaal University of Technology

Mr Thuto Ofentse Tshegofentse Facilities and Engineering

Prof. Freeman Ntuli University of Johannesburg

Prof. Geoffrey Simante University of the Witwatersrand

Prof. Craig Sheridan University of the Witwatersrand

Ms Ronell Viljoen Johannesburg Water (Pty) Ltd

CAPACITY BUILDING

Several students (listed in Table I) at different stages of schooling have benefitted from the WRC funded project. The BTech students listed are only those that work on research projects related to the current WRC project, and for which the running costs are partly paid by the project. The masters and PhD (postgraduate) students listed are currently actively involved in running the project and are benefiting through bursaries, conference funding and purchase of equipment and consumables. These postgraduate students are also actively involved in supervising their BTech. counterparts.

Table I: Students involved

| Name of Student | Level of study |
|---------------------|----------------|
| Mr M Khune | MTech |
| Ms JN Mabuza | MTech |
| Ms BP Matshediso | MTech |
| Mr JWJP Akach | PhD |
| Mr BO Otieno | PhD |
| Ms JF Mbatha | BTech |
| Ms MA Seretlo | BTech |
| Ms MI Mofokeng | BTech |
| Ms N Khanyisile | BTech |
| Mr Khanyie Mncube | BTech |
| Ms Nokulunga Mbatha | BTech |

PUBLICATIONS AND CONFERENCE PRESENTATIONS

The work contained in this report has been presented at several local and international conferences and published in peer-reviewed journals, as indicated in the lists below.

List of publications

- Otieno, B., Apollo, S., Kabuba, J., Naidoo, B., Simate, G. and Ochieng, A. (2019).
 Ozonolysis pre-treatment of waste activated sludge for solubilization and biodegradability enhancement. *Journal of Environmental Chemical Engineering*, 7, p. 1029-045.
- 2. Otieno, B., Apollo, S., Kabuba, J., Naidoo, B. and Ochieng, A. (2019). Ozonolysis Post-treatment of Anaerobically Digested Distillery Wastewater Effluent. *Ozone: Science & Engineering*, 41 (6), p. 551-561.
- 3. Otieno, B., Apollo, S., Naidoo, B. and Ochieng, A. (2019). Modeling ozonolysis pretreatment parameters of distillery wastewater for improved biodegradability. *Journal of Environmental Science and Health, Part A*, 54 (11), p. 1066-1074.
- 4. Otieno, B., Nomalungelo, M., Apollo, S., Naidoo, B., and Ochieng, A. (2019). Photodegradation of Phenol by Silver Doped TiO₂; Photodegradation of Phenol by Silver Doped TiO₂; A Comparative Study of the Efficiency of HPLC and UV-Vis Analyses, in Ramasami P., Gupta Bhowon M., Jhaumeer Laulloo S., Li Kam Wah H. (eds.) *Chemistry for a Clean and Healthy Planet*. Springer, Cham, p. 123-138.
- Otieno, B., Apollo, S., Naidoo, B. and Ochieng, A. (2019). Influence of zeolite support on integrated biodegradation and photodegradation of molasses wastewater for organic load reduction and colour removal, in Arora N., Kumar N. (eds.) *Phyto and Rhizo Remediation. Microorganisms for Sustainability*, vol 9. Springer, Singapore, 287-300.
- 6. Akach, J. and Ochieng, A. (2018). Monte Carlo simulation of the light distribution in an annular slurry bubble column photocatalytic reactor. Chemical Engineering Research and Design, 129, p. 248-254.
- 7. Apollo, S., Otieno, B., and Ochieng, A. (2018). Application of natural zeolite as catalyst and biomass support in an integrated photodegradation and anaerobic digestion of textile wastewater, in Mujtaba, I., Majozi, T. and Amosa, M. (eds.) Water Management: Social and Technological Perspective. London, p. 369-379.
- 8. Mabuza, J., Otieno, B., Apollo, S., Matshediso, B., and Ochieng, A. (2017). Investigating the synergy of integrated anaerobic digestion and photodegradation

using hybrid photocatalyst for molasses wastewater treatment. Euro-Mediterranean Journal for Environmental Integration, 2 (1), p. 17.

List of conference presentations

- 1. Otieno, B., Apollo, S., Naidoo, B. and Ochieng, A. (2019). Designing and Evaluating an Integrated Anaerobic and Ozonolysis Treatment System for Distillery Wastewater. 6th South African Young Water Professionals Biennial Conference. October 20-23, 2019, Durban-South Africa.
- 2. Otieno, B., Apollo, S., Naidoo, B. and Ochieng, A. (2019). A combined anaerobic digestion and ozonation treatment of vinasse. *Pan Africa Chemistry Network Congress* (*PACN*) 2019 Riches of the natural world: sustainable use of Africa's natural products and materials. November 5-7, 2019, Addis Ababa, Ethiopia.
- 3. Otieno, B., Apollo, S., Naidoo, B. and Ochieng, A. (2019). Combined Ozonolysis Pretreatment and Anaerobic Digestion of Municipal Waste Activated Sludge. *ANSO-MMU-SAJOREC International Conference*. September 4-8, 2019, Maasai *Mara University, Narok, Kenya*.
- 4. Otieno, B., Apollo, S., Naidoo, B. and Ochieng, A. (2019). Ozonolysis Post-treatment of Anaerobically Digested Vinasse; Color reduction and Sludge Solubilisation. 9th *International Young Water Professionals Conference*. June 23-27, 2019, *Toronto, Canada*.
- 5. Otieno, B., Apollo, S., Naidoo, B., and Ochieng, A. (2019). A combined Anaerobic Digestion and Ozonolysis Treatment of Vinasse for the removal of Organic Contaminants and Colour. *IUPAC Postgraduate Summer School on Green Chemistry*. June 12-19, 2019 *Dar es Salaam, Tanzania*.
- 6. Otieno, B., Apollo, S., Naidoo, B. and Ochieng, A. (2018). Ozonolysis of distillery wastewater for improved biodegradability; Effect of solubilization and reduced aromaticity on biodegradability. *International Conference on Pure and Applied Chemistry*. July 18-22, 2016 *Port Louis, Mauritius*.
- 7. Otieno, B., Apollo, S., Naidoo, B. and Ochieng, A. (2017). Application of natural South African zeolite as catalyst and biomass support in an integrated photodegradation and anaerobic digestion of textile wastewater. 9th International Conference of the African Materials Research Society (AMRS 2017) Dec. 11-14, 2017, Gaborone, Botswana.

TABLE OF CONTENTS

| Executive S | ummary iii |
|---------------|--|
| Acknowledg | gmentsvi |
| Capacity Bu | ildingvii |
| Publications | and Conference Presentations |
| Table of Co | ntentsxi |
| List of Figur | resxvi |
| List of Table | esxviii |
| Acronyms | xix |
| Symbols | xxi |
| CHAPTER | 1: INTRODUCTION AND BACKGROUND1 |
| 1 Study I | Background1 |
| 1.1 Pro | oblem statement |
| 1.2 Ge | neral research objective |
| 1.3 Spe | ecific objectives3 |
| CHAPTER | 2: LİTERATURE REVİEW5 |
| 2 Introdu | ction5 |
| 2.1 Dis | stillery wastewater5 |
| 2.1.1 | Generation of distillery wastewater6 |
| 2.1.2 | Characteristics of DWW |
| 2.1.3 | Distillery wastewater colourants and pollutants9 |
| 2.1.4 | Environmental and health effects of DWW |
| 2.2 Mu | nicipal wastewater and waste activated sludge |
| 2.2.1 | General characteristics of waste activated sludge |
| 2.2.2 | Special characteristics of waste activated sludge |
| 2.2.3 | Effects of waste activated sludge |
| 2.3 An | aerobic digestion treatment of distillery wastewater and waste activated sludge 15 |

| 2.3 | 3.1 | Overview of the anaerobic digestion process | 16 |
|-------|-------|---|----|
| 2.3 | 3.2 | Anaerobic reactors | 17 |
| 2.3 | 3.3 | Kinetic modelling of anaerobic digestion | 19 |
| 2.3 | 3.4 | Limitations of anaerobic digestion | 20 |
| 2.4 | Adv | vanced oxidation processes | 21 |
| 2.4 | 4.1 | The basic principle of AOPs | 22 |
| 2.4 | 4.2 | Fenton and photo Fenton | 23 |
| 2.4 | 4.3 | Photocatalysis | 23 |
| 2.4 | 4.4 | Ozonolysis | 24 |
| 2.5 | Sim | nulation and modelling of reactors | 25 |
| 2.5 | 5.1 | Hydrodynamics | 25 |
| 2.5 | 5.2 | Light intensity distribution. | 26 |
| 2.6 | Inte | egrated anaerobic digestion and advanced oxidation processes | 27 |
| 2.6 | 5.1 | Advanced oxidation pre-treatment | 28 |
| 2.6 | 5.2 | Advanced oxidation post-treatment | 28 |
| 2.6 | 5.3 | Factors to consider in an integrated anaerobic-ozonolysis process | 29 |
| СНАРТ | ΓER 3 | S: CFD SİMULATİON OF FLUİDİZED BED REACTOR | 30 |
| 3 Int | trodu | etion | 30 |
| 3.1 | Me | thodology | 30 |
| 3.1 | 1.1 | Governing equations | 30 |
| 3.1 | 1.2 | Numerical modelling | 31 |
| 3.2 | Res | ults and discussion | 34 |
| 3.2 | 2.1 | Grid size | 34 |
| 3.2 | 2.2 | Reactor geometry | 35 |
| 3.0 | 2.3 | Fluidized hed reactor | 37 |

| CHAPTER | 4: INTEGRATED ANAEROBÍC DÍGESTÍON AND OZONOLYSÍS |
|-----------|---|
| TREATME | NT OF DWW41 |
| 4 Introdu | action41 |
| 4.1 Ma | aterials and methods41 |
| 4.1.1 | Materials41 |
| 4.1.2 | Anaerobic digestion and ozonation processes |
| 4.1.3 | Chemical analyses |
| 4.1.4 | Ozone transfer |
| 4.2 Re | sults and discussion on anaerobic digestion of DWW44 |
| 4.2.1 | Bioreactor start-up44 |
| 4.2.2 | Organic load and colour reductions during anaerobic digestion44 |
| 4.2.3 | Kinetic parameters of anaerobic digestion |
| 4.3 Re | sults and discussion ozonolysis post-treatment of anaerobically digested DWW 47 |
| 4.3.1 | Characteristics of the distillery wastewater before and after AD47 |
| 4.3.2 | Effect of initial concentration |
| 4.3.3 | Energy utilization and ozone transfer at different initial concentrations48 |
| 4.3.4 | Effect of ozone dosage |
| 4.3.5 | Effect of initial pH51 |
| 4.4 Re | sults and discussion on kinetics of integrated AD and ozonolysis of DWW51 |
| CHAPTER | 5: ENERGY, COST AND ENVİRONMENTAL ANALYSİS OF |
| INTERGRA | ATED AD-OZONOLYSIS TREATMENT FOR DWW54 |
| 5 Introdu | action54 |
| 5.1 Me | ethodology55 |
| 5.2 Re | sults and discussion57 |
| 5.2.1 | Energy analysis57 |
| 5.2.2 | Cost analysis and carbon dioxide emission reduction |
| 5.2.3 | Comparison of integrated AD-ozonolysis with other treatment options59 |

| | | 6: OZONOLYSİS PRE-TREATMENT OF WASTE ACTİVATED | |
|-----|---------|---|----|
| | | BİLİZATİON AND BİODEGRADABİLİTY ENHANCEMENT | |
| 6 | Introdu | iction | 60 |
| 6. | 1 Ma | nterials and methods | 60 |
| | 6.1.1 | Materials and methods | 60 |
| | 6.1.2 | Waste activated sludge | 61 |
| | 6.1.3 | Ozonolysis experiments | 61 |
| | 6.1.4 | Anaerobic digestion of WAS | 61 |
| | 6.1.5 | Average oxidation state | 62 |
| | 6.1.6 | Chemical analysis | 62 |
| 6. | 2 Re | sults and discussion | 63 |
| | 6.2.1 | Characteristics of waste activated sludge | 63 |
| | 6.2.2 | Effect of ozone dosage | 63 |
| | 6.2.3 | Effect of initial pH | 64 |
| | 6.2.4 | Change in COD, biodegradability, and ozone transfer | 65 |
| | 6.2.5 | Sludge solubilization mechanism | 67 |
| | 6.2.6 | Effect of ozone pre-treatment on anaerobic digestion of WAS | 70 |
| | 6.2.7 | Comparison of ozonolysis with other pre-treatment methods | 71 |
| CHA | APTER | 7: CONCLUSION AND RECOMMENDATIONS | 72 |
| 7 | Project | conclusions and recommendation | 72 |
| 7. | 1 Co | nclusions | 72 |
| 7. | 2 Re | commendations | 74 |
| REF | ERENC | CES | 75 |
| APP | ENDIC | ES | 87 |
| A | ppendix | A: Anaerobic reaction kinetic models | 87 |
| | | B: Photocatalytic and ozonolysis reaction processes | |
| | | C: CFD modelling | 90 |

| Appendix D: Effect of turbulence CFD models | 95 |
|---|-----|
| Appendix E: Effect of interfacial forces during CFD modelling | 102 |
| Appendix F: Anaerobic reaction kinetics | 106 |

LIST OF FIGURES

| Figure 2.1: Process description for the generation of distillery wastewater | 6 |
|--|----|
| Figure 2.2: Basic structure of melanoidins. | 9 |
| Figure 2.3: Environmental impact of distillery wastewater | 10 |
| Figure 2.4: Basic flow diagram of a municipal wastewater treatment system | 13 |
| Figure 2.5: A sketch of EPS structure | 15 |
| Figure 2.6: Reaction steps of anaerobic digestion of complex organic matter | 16 |
| Figure 2.7: A schematic diagram of a UASB reactor. | 19 |
| Figure 2.8: Schematic representation of the photocatalytic process | 24 |
| Figure 3.1: Reactor geometry coordinate | 31 |
| Figure 3.2: Fluidized bed reactor mesh | 33 |
| Figure 3.3: RMSE of different turbulent models and cells. | 35 |
| Figure 3.4: Grid of reactor geometry | 35 |
| Figure 3.5: Effect of reactor geometry on simulation accuracy (RMSE) | 36 |
| Figure 3.6: Effect of reactor geometry on the time-averaged gas holdup contours | 37 |
| Figure 3.7: Radial axial liquid velocity profile | 38 |
| Figure 3.8: Radial gas and solid holdup profiles | 39 |
| Figure 3.9: Contour plots of phase holdups | 40 |
| Figure 4.1: Schematic representation of the anaerobic andozonation units | 43 |
| Figure 4.2: Daily biogas production, pH and VFA/Alkalinity. | 44 |
| Figure 4.3: Organic load reduction during the semi-continuous operation the digester | 45 |
| Figure 4.4: Determination of growth and decay rates | 46 |
| Figure 4.5: Effect of dilution on color and TOC reductions | 48 |
| Figure 4.6: Comparison of ozone transfer and color reduction, | 49 |
| Figure 4.7: Effect of ozone flowrate on color reduction | 50 |
| Figure 4.8: Effect of pH on color and TOC reductions during ozonolysis of DWW | 51 |
| Figure 4.9: Determination of first-order reaction kinetics of AD | 52 |
| Figure 5.1: Alternative uses for the biogas produced | 54 |
| Figure 5.2: Energy produced by anaerobic digestion | 57 |
| Figure 5.3: Carbon emission reduction scenarios | 58 |
| Figure 6.1: Effect of ozone dosage on; | 64 |

| Figure 6.2: Effect of pH on ozonolysis of WAS | 65 |
|--|----|
| Figure 6.3: Change in COD _T and COD _S during ozonolysis of WAS | 66 |
| Figure 6.4: Change in AOS during ozonolysis a | 67 |
| Figure 6.5: Change in proteins, carbohydrates and cations concentration | 68 |
| Figure 6.6: DTG and TGA curves of WAS. | 69 |
| Figure 6.7: COD and TSS reduction during anaerobic digestion of WAS | 70 |

LİST OF TABLES

| Table 2.1: Distillery wastewater generation in various alcohol plant operations | 7 |
|--|----|
| Table 2.2: Typical characteristics of distillery wastewater from different feedstocks | 8 |
| Table 2.3: Typical characteristics of wastewater from different streams | 8 |
| Table 2.4: Potential impacts of distillery wastewater on the environment | 11 |
| Table 2.5: Physicochemical characteristics of waste activated sludge | 13 |
| Table 2.6: Average special characteristics of waste activated sludge | 14 |
| Table 2.7: Performance of high rate anaerobic reactors | 18 |
| Table 2.8: Relative oxidation activity of common oxidants | 21 |
| Table 2.9: Relative oxidation activity of common oxidants | 23 |
| Table 4.1: Characteristics of the vinasse before treatment | 42 |
| Table 4.2: Characteristics of the distillery wastewater before and after anaerobic digestion | 47 |
| Table 5.1: Total energy requirement for the different units of the integrated system | 59 |
| Table 6.1: Physicochemical characteristics of municipal waste activated sludge | 63 |
| Table 6.2: Weight loss at different phases of combustion of dried WAS | 69 |

LIST OF ACRONYMS

AD Anaerobic digestion

ANOVA Analysis of variance

AOPs Advanced oxidation processes

AOS Average oxidation state

AST Activated sludge treatment

BOD Biochemical oxygen demand

BSA Bovine serum albumin

COD Chemical oxygen demand

COS Carbon oxidation state

DEHP Bis (2-ethylhexyl) phthalate

DOC Dissolved organic carbon

DTA Differential thermogravimetric analysis

DWW Distillery wastewater

EC Electrocoagulation

EDC endocrine disrupting compounds

EPS Extracellular polymeric substances

FTIR Fourier transform infrared

GHG Greenhouse gas

glc Glucosamine

HMW High molecular weight

HRT Hydraulic retention time

LB-EPS Loosely bound extracellular polymeric substances

LMW Low molecular weight

MR Malliard reaction

MW Molecular weight

MWTP Municipal wastewater treatment plant

MWW Molasses wastewater

NP Nonylphenol

OLR Organic loading rate

PS Polysaccharides

RO Reverse osmosis

S-EPS Slime extracellular polymeric substances

SS Suspended solids

TB-EPS Tightly bound extracellular polymeric substances

TGA Thermal gravimetric analysis

TOC Total organic carbon

TS Total solids

TSS Total suspended solids

UASB Upward flow anaerobic sludge blanket

UV Ultraviolet light

VFAs Volatile fatty acids

VOC Volatile organic compounds

VSS Volatile suspended solids

WAS Waste activated sludge

LIST OF SYMBOLS

| В | Biomass kinetic parameter (g COD/g biomass) |
|---------------------------|--|
| B_{p} | Biogas production potential (L) |
| B_t | Cumulative biogas produced (L) at a given time |
| C_{f} | Final concentration of target contaminant. |
| C_{i} | Initial concentration of target contaminant |
| I | Index number for patterns |
| j | Index number for patterns |
| k | Number of patterns |
| \mathbf{k}_1 | First order reaction rate constant (hr ⁻¹) |
| K_d | Biomass death rate (hour-1) |
| K_s | Monod-constant |
| O ₃ S | Supplied ozone (mg) |
| O ₃ T | Ozone transfer (%) |
| O_3U | Utilized ozone (mg) |
| P | Ozone reactor power (kW), |
| Q | Substrate inflow rate (L/hr) |
| R_b | Maximum biogas production rate (L/hr) |
| S | Effluent substrate concentration |
| $S_{ m g}$ | Fraction of the influent COD converted to biogas |
| S_{m} | Fractions of the influent COD used for cell maintenance. |
| S_o | Influent substrate concentration |
| S_{ss} | Fraction of the influent COD converted to suspended solids |

Retention time (hrs)

t

- V Reactor volume (L)
- X Biomass concentration (g/L)
- X_i Coded independent variable
- X_k Coded independent variable
- Y Dependent variable (response of choice)
- Y_{xs} Biogas yield coefficient (g/g)

GREEK SYMBOLS

- μ_{max} Biomass specific growth rate at saturation
- β_o Offset term
- μ Biomass specific growth rate (hr⁻¹)
- ε Random error
- βi Linear effect
- βii Quadratic effect
- βij Interaction effect
- λ Lag phase (hrs)

CHAPTER 1: INTRODUCTION AND BACKGROUND

1 Study Background

Alcohol distilleries are some of the major polluting industries as about 88% of the raw material used ends up as waste, mainly in the form of wastewater (Shivajirao, 2012). Most cane molasses-based distilleries produce about 15 liters of effluent (wastewater) per liter of ethanol produced. In 2008, approximately 79 billion liters of ethanol were produced globally, resulting in the generation of 2.4×10^{12} liters of distillery effluent (Rajagopal et al., 2014). The global annual production of the effluent is expected to reach 1.7×10^{15} liters by 2024 (Hoarau et al., 2018). When discharged into aquatic systems without proper treatment, distillery wastewater (DWW) can cause eutrophication and hinder the photosynthetic activity of aquatic plants (Navgire et al., 2012; Otieno et al., 2016). The increasing environmental hazards associated with the discharge of the recalcitrant compounds contained in industrial effluents has led to more stringent discharge standards set by governments and regulating bodies (Mantzavinos et al., 1999; Oller et al., 2011).

The stringent discharge regulations have also been extended to the effluents from municipal wastewater treatment plants (Mecha et al., 2016). Municipal wastewater, which is generally generated from different domestic sources is widely treated through the activated sludge process with waste activated sludge (WAS) generated in large volumes as a major by-product (Demir and Filibeli, 2012; Zhou et al., 2017). The WAS consists of biomass from cell growth, pathogens, heavy metals, and toxic chemicals, thus posing the risk of secondary environmental pollution if not stabilized (Yuan et al., 2016). The treatment and disposal of excessive sludge account for up to 60% of the total cost of a wastewater treatment plant (Demir and Filibeli, 2012). The problem of WAS disposal is escalating, given the rising and high costs for sludge storage, dewatering, transport, and landfilling (Wang et al., 2017).

The usually preferred anaerobic treatment for WAS and DWW is not sufficient in meeting the stringent discharge requirements for total suspended solids (TSS), micropollutants, colour and chemical oxygen demand (COD) (Kim et al., 2010). The WAS consist of heterotrophic substances not easily biodegradable, complex floc structure, hard cell wall, and large organic molecules which cannot be absorbed by microorganisms. A large amount of energy is therefore required to rapture the bacterial cell envelope, thereby limiting the hydrolysis step leading to incomplete degradation and increased degradation time during AD treatment of WAS (Bougrier et al., 2006; Yuan et al., 2016). In the case of DWW, the presence of biorecalcitrant

melanoidin compounds and suspended solids hinder the hydrolysis step of the AD. Moreover, in most instances during anaerobic digestion, the melanoidin compounds repolymerise, thereby intensifying the colour of the anaerobically digested effluent.

To enhance the AD process, its integration with other treatment technologies is required (Oller et al., 2011). Pre-treatment methods, such as chemical, thermal, and electrical treatments have been developed to accelerate the rate of digestion and improve biogas production during AD (Wang et al., 2017). Of the pre-treatment techniques, currently being employed, ozonolysis, which is an advanced oxidation process (AOP), is very effective in yielding the highest degree of organic solids disintegration and improved substrate biodegradability. It also improves sludge settling properties as well as reducing scum formation and bulking (Chu et al., 2009). Ozonolysis can also be applied as a post-treatment to eliminate the recalcitrant organic pollutants and colour that escape the AD process (Oller et al., 2011).

To overcome the high cost usually associated with the application of AOPs, the energy from the biogas can be used to operate the integrated system leading to cost reduction and environmental conservation. Also, improved performance of the integrated system could be achieved by applying fluidised bed reactors (FBR), which are robust due to their efficiency in achieving high multiphase mixing which results in improved mass transfer. It has been shown by Chen et al. (2015) that the performance of FBR can be improved by optimizing the hydrodynamic conditions. It is very expensive and sometimes unfeasible to determine experimentally the hydrodynamics, mass transfer, and photon distribution profiles in the whole reactor in the case of AOPs. Therefore, simulation tools such as computational fluid dynamics and Monte Carlo are normally used (Boyjoo et al., 2013).

1.1 Problem statement

Alcohol distilleries and municipal wastewater treatment plants produce large amounts of waste (DWW and WAS, respectively) requiring remediation before disposal to receiving streams. Anaerobic digestion, widely used for WAS stabilization and DWW treatment, suffers from limitations such as high retention time, low methanogenic production, and an overall 30-35% dry solids degradation in mesophilic conditions. The low solids degradation is caused by the hard cell walls and extracellular polymeric structure (EPS) of WAS, which are difficult to hydrolyse and digest (Zhen et al., 2017). In the anaerobic digestion of DWW, the presence of biorecalcitrant melanoidin compounds hinders the rate determining hydrolysis step. Moreover,

in most instances, the melanoidin compounds repolymerise, thereby intensifying the colour of the anaerobically digested effluent (Apollo and Aoyi, 2016).

Integrating AD with other treatment methods such as an advanced oxidation process (AOP) is thus important for achieving effective pollutant removal. Ozonolysis, an AOP, can be used as a pre-treatment process to reduce the biorecalcitrant melanoidins in DWW into biodegradable compounds, and solubilize the WAS. However, the determination of the not-well-understood mechanisms and intermediate compounds formed during ozonolysis is important for achieving an effective and optimized pre-treatment. The ozonolysis pre-treatment, in some instances, does not lead to a complete reduction of the biorecalcitrants into biodegradable compounds. The unreduced biorecalcitrant compounds escape into the AD process and later into the anaerobically digested effluent. The digested effluent, therefore, still contains the unreduced biorecalcitrants, including colour, thus requiring the introduction of a post-treatment phase to polish the effluent. Ozonolysis can still be introduced as a post-treatment to AD to remove the remaining biorecalcitrants. The process efficiency of the integrated AD-AOP needs to be improved by optimizing the individual processes and determining the best order of integration that would ensure effective wastewater treatment. The study of the reactor hydrodynamics using simulation tools such as CFD is important in overcoming the high cost associated with physical experiments. Moreover, for practical application of the integrated system, it is important to carry out energy, cost, and environmental analysis.

1.2 General research objective

To integrate anaerobic digestion and ozonolysis for effective treatment of distillery wastewater and waste activated sludge.

1.3 Specific objectives

- i. To apply CFD modelling to determine the optimal reactor hydrodynamic conditions,
- ii. To carry out anaerobic digestion of DWW and model the sludge production kinetics,
- iii. To carry out ozonolysis post-treatment of anaerobically digested DWW and optimise the operational parameters,
- iv. To design and evaluate the performance of an integrated AD and AOP system treating DWW,

- v. To conduct energy and economic analyses as well as analysis of carbon dioxide emission reduction of the integrated AD-AOP process treating DWW,
- vi. To carry out ozonolysis pre-treatment of WAS and determine best-operating conditions, analyze the sludge disintegration mechanism and biorecalcitrant reduction, and identify the ozonolysis products, and
- vii. To determine the biodegradability of ozone pre-treated WAS and determine the effect of ozonolysis pre-treatment on anaerobic digestion.

CHAPTER 2: LİTERATURE REVİEW

2 Introduction

Among the natural resources, water is the most important and is critical for food production, economic activities, and survival of all living things, including humans. Water quality (including surface and groundwater) and availability influence the environment, development, and economic growth. Human activities, increased urbanization, industrialization, population increase, and climate change have all created a decline in water quality. Industrial processes such as alcohol distillation, wine production, leather tanning, and textiles generate a copious amount of wastewater (Halder and Islam, 2015). Such industries use a large volume of water in the production processes and contaminate it with toxic chemicals, heavy metals, organic sludge, and even radioactive wastes. The pollutants are then dumped into receiving streams leading to massive pollution of rivers, lakes, and other aquatic systems.

Increased population and urbanization, and expanded sewer coverage have also led to the generation of large amounts of municipal wastewater, which is conveyed as sewage for treatment at municipal wastewater treatment plants (WWTP). The conventional municipal WWTP is not effective in removing emerging persistent micropollutants such as pharmaceuticals, detergents, and endocrine disrupting substances. These micropollutants, when discharged in the treated effluent into water systems, can bioaccumulate in organisms and adversely affect endocrine systems (Bechambi et al., 2015; Shivaraju, 2011). The present chapter presents an overview of the generation and characteristics of the distillery wastewater and municipal waste activated sludge, evaluates the anaerobic digestion technology currently used for wastewater remediation and its limitations, and thereafter presents the potential of integrating AD with an advanced oxidation treatment process to overcome the limitations.

2.1 Distillery wastewater

Agro-processing industries, including dairy, edible oils, breweries, distilleries, sugar factories, and pulp and paper, contribute significantly to economic growth and human development. Despite the positive contribution, these industries generate massive organic wastes (65-70% of the total industrial organic wastewater), causing environmental pollution if disposed of without proper treatment (Ray and Ghangrekar, 2018). Distilleries, alcohol and wine producing industries are the most important pollution load contributors among all agro-processing industries as about 88% of the raw material used ends up as waste mainly in the form of wastewater. In South Africa, wine production has increased in the last decade, applying more

pressure on natural resources such as soil, water, and vegetation (Green, 2007). In 2012, a total volume of 252.9×10^6 hL of wine was produced worldwide with 4% of the total amount (10×10^9 hL) coming from South Africa (Conradie et al., 2014).

2.1.1 Generation of distillery wastewater

Alcohol (ethanol) production consists of four major steps, including feed preparation, fermentation, distillation, and packaging, as shown in Figure 2.1 (Kharayat, 2012).

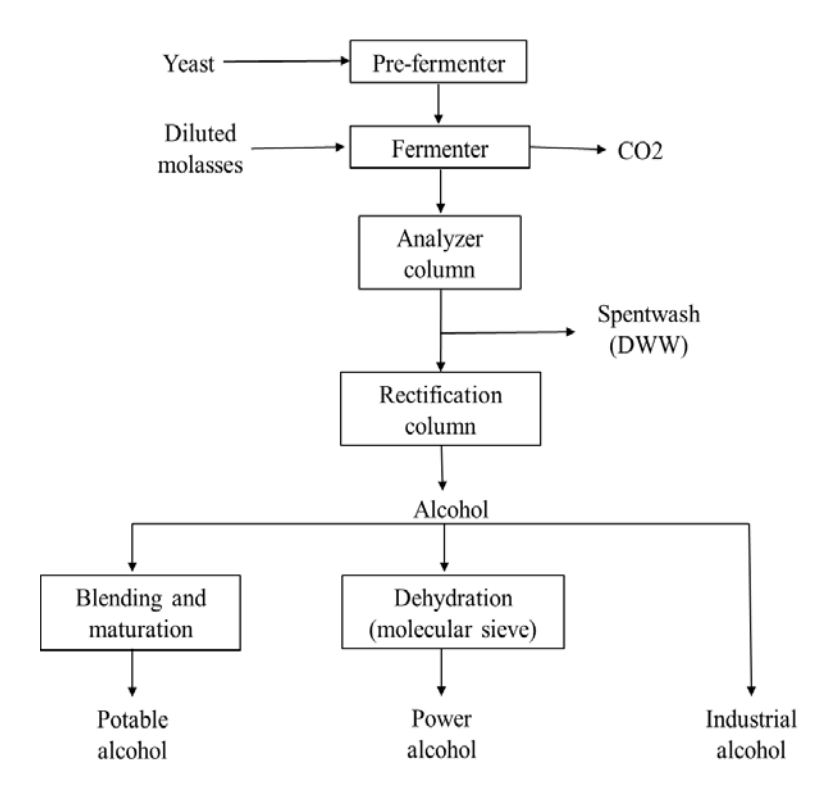


Figure 2.1: Process description for the generation of distillery wastewater.

A wide range of feedstock including sugar-based (beet and cane molasses, cane juice), cellulosic (sugarcane bagasse, wood, crop residues) and starch-based (cassava, wheat, corn, rice, barley) materials can be used. Generally, the sugar-based feedstock, which contains readily available fermentable sugars, are preferred with cane molasses having the highest application (Shivajirao, 2012; Satyawali and Balakrishnan, 2008). In the distillation process, molasses is diluted and taken to a fermenter to produce broth containing bioethanol (6-8% ethanol composition) with the addition of yeast in a batch or continuous mode. In the continuous mode, the cellulosic materials are first delignified, followed by subsequent hydrolyzation into simple sugars. The sugars are then fermented in the presence of yeast yielding carbon dioxide and ethanol. The fermentation broth is filtered and then distilled to

concentrate bioethanol (Satyawali and Balakrishnan, 2008). The final effluent after the distillation process is the distillery wastewater (DWW), a viscous hydrophilic dark coloured liquid with a strong objectionable odour (Arimi et al., 2014; Chavan et al., 2006). The amount of wastewater generated at the different stages of alcohol distillation is presented in Table 2.1.

Table 2.1: Distillery wastewater generation in various alcohol plant operations (Satyawali and Balakrishnan, 2008).

| Distillation process | Average DWW generated (kLD/distillery) | Specific DWW generated (kL DWW/kL alcohol) | | |
|----------------------|--|--|--|--|
| Spent wash | 491.9 | 11.9 | | |
| Fermenter cleaning | 98.2 | 1.6 | | |
| Fermenter cooling | 355.1 | 2.0 | | |
| Condenser cooling | 864.4 | 7.9 | | |
| Floor wash | 30.8 | 0.5 | | |
| Bottling plants | 113.8 | 1.3 | | |
| Others | 141.6 | 1.2 | | |

In the wine industry, the distillation process is employed by separating mixtures of different liquids, which becomes either alcohol, wine, or brandy. The wine distilleries use large volumes of water mainly for cooling and cleaning purposes generating heavily polluted wine distillery wastewater (WDWW) (Otieno, 2007). The demand for bioethanol is ever increasing due to its various applications, including transportation fuel, and its increased production will lead to a greater generation of DWW (Pradhan and Mbohwa, 2014). Moreover, the recent upsurge in global demand for wine and its products, such as spirit related beverages, has caused increased wine production leading to the increase in several problems related to the generation and disposal of large quantities of the high strength wine distillery wastewater (Buys, 2015).

2.1.2 Characteristics of DWW

The characteristics and level of pollutants of DWW vary depending on the raw materials and feedstock used as the substrate for bioethanol production, process efficiency, and handling of the wastewater (Ghosh and Ghangrekar, 2018). Some of the typical characteristics of DWW from various feedstocks and streams of alcohol distillation are given in Table 2.2 and Table 2.3, respectively.

Table 2.2: Typical characteristics of distillery wastewater obtained from different feedstocks

| Parameters | Feedstock | | | | | | |
|---------------------|---------------|------------|--------|-------------------|---------------------|------------------|----------|
| | Sugarcanea | Sugarcaneb | Corna | Rice ^c | Potato ^d | Winerya | Winerye |
| Total COD (g/L) | 92-100 | 70-98 | 85 | 56 | 51.7 | 3.1-3.4 | 0.86 |
| Soluble COD (g/L) | - | - | 57 | - | - | 7.6-16 | - |
| $BOD_5(g/L)$ | 52-58 | 45-60 | - | 26-31 | - | 12.3 | 0.2-0.8 |
| TSS (g/L) | 2.0-2.2 | (0, 00 | 26.2 | 25-30 | - | 2.4-5 | 0.2.0.5 |
| TDS (g/L) | 89-91 | 60-90 | 33.4 | - | - | 9-27 | 0.2-0.5 |
| TKN (g/L) | 1.6-1.8 | 1-1.2 | 3.4 | 2.2 | 1 | 0.1-6.4 | 0.1-0.6 |
| Phenol (g/L) | 0.4 | - | - | - | - | 0.5 | 0.03-0.5 |
| VFA (total) (g/L) | 2.3-2.4 | - | 10.8 | 10.8 | 24.5 | 1-6 | - |
| Phosphate (ppm) | 3038 | - | 363 | 4 | 165 | 130-350 | - |
| Sulphate (ppm) | 3800 | - | 527 | - | - | 3640 | - |
| Acidity (total) | 7.4-8.1 | - | - | - | - | - | - |
| Conductivity (mS/m) | 5100-5380 | - | - | - | - | - | - |
| pН | 4.2-4.3 | 3.8-4.4 | 3.7 | 3.1 | 3.8 | 3.9-4.5 | 3.5-5.4 |
| Colour | Dark brown | - | Yellow | Yellowish white | White | Reddish brown | - |

TSS total suspended solids, TDS total dissolved solids, TKN total Kjeldahl nitrogen, VFA volatile fatty acids ^aGhosh Ray and Ghangrekar. (2018), ^bOtieno. (2017), ^cTang et al. (2007), ^dCibis et al. (2006) and ^cMelamane et al. (2007).

Table 2.3: Typical characteristics of wastewater obtained from different streams of the distillation process (Kharayat, 2012).

| Parameter | | | Stream | | | |
|-------------------------|---------------|-------------------|--------------------|-------------------|----------------|----------------|
| | Spentwash | Fermenter cooling | Fermenter cleaning | Condenser cooling | Fermenter wash | Bottling plant |
| Colour | Dark brown | Colourless | Colourless | Colourless | Faint | Colourless |
| рН | 4-4.5 | 6.26 | 5.0-5.5 | 6.8-7.8 | 6 | 7.45 |
| Alkalinity (g/L) | 3.5 | 0.3 | Nil | - | 0.04 | 0.08 |
| Total solids (g/L) | 100 | 1-1.3 | 1-1.5 | 0.7-0.9 | 0.55 | 0.4 |
| Suspended solids (mg/L) | 10 | 0.22 | 0.4-0.6 | 0.18-0.2 | 0.3 | 0.1 |
| $BOD_5(g/L)$ | 45-60 | 0.1-0.11 | 0.5-0.6 | 0.07-0.08 | 0.015 | 0.005 |
| COD (g/L) | 80-120 | 0.5-1 | 1.2-1.6 | 0.2-0.3 | 0.025 | 0.015 |

The winery DWW consists of the least concentration of organic load as compared to the other feedstocks, but with a relatively high concentration of aromatic phenolic compounds. The DWW from corn, rice, and potato feedstocks have medium organic load ranging from 51-85 g/L COD and yellowish white coloured effluents. The DWW from sugarcane feedstock due to its high organic load is characterized by the highest biochemical oxygen demand (BOD) and chemical oxygen demand (COD), and a dark brown colour (Satyawali and Balakrishnan, 2008).

The spent wash stream imparts colour to the other colourless streams, such as the fermenter cooling and cleaning (Table 2.3), leading to the overall dark brown colour of the DWW discharged from distillation plants.

2.1.3 Distillery wastewater colourants and pollutants

The colour of DWW is caused by organic compounds such as carotenoids, chlorophyll, heme pigments, anthocyanins, betalains, riboflavins, quinone pigments, caramels, melanoidins, phenolics, and melanin. Since there are no inorganic pigments added in the process leading to the production of molasses, the occurrence of synthetic colourants is highly unlikely (Panthi et al., 2015). Melanoidin pigments, which have been reported to constitute 2% of cane molasses are mainly responsible for the characteristic dark brown colour (Chavan et al., 2006). Melanoidins are heterogeneous, nitrogen-containing brown pigments formed during a nonenzymatic reaction (Maillard reaction) involving amino compounds and carbohydrates. The reaction effectively proceeds at temperatures >50°C and pH 4-7 (Satyawali and Balakrishnan, 2008). Maillard reaction involves different amino acids in addition to the extended different levels of repolymerisations. Thus the characterization of the definite melanoidin structure has not been achieved (Arimi et al., 2015). Melanoidins are polymeric in nature, have a general empirical formula of C_{17} -18 H_{26} -27 $O_{10}N$, and with a high molecular weight (usually ≥ 5.0 kDa) making them anti-oxidative and thus recalcitrant to biodegradation (Liang et al., 2009; Liu et al., 2013). The basic structure of the melanoidin compound is given in Figure 2.2. Apart from the colourants, DWW also contains a variety of carcinogenic, cytotoxic, mutagenic, and endocrine disrupting substances (Chowdhary et al., 2018).

Figure 2.2: Basic structure of melanoidins (Santal & Singh, 2013).

2.1.4 Environmental and health effects of DWW

Given the large volume, high organic content, biorecalcitrant components, low pH, and other organic pollutants, DWW poses a great threat to the environment including water bodies, soil contamination, and atmospheric greenhouse gases to the general human health, as shown in Figure 2.3 (Hoarau et al., 2018). DWW was initially managed by discharge to water streams and then later used as fertilizer by irrigation of fields (Hoarau et al., 2018; Fuess et al., 2018). However, when discharged into aquatic systems without proper treatment, DWW can cause eutrophication and hinder the photosynthetic activity of aquatic plants (Otieno et al., 2016; Navgire et al., 2012). Inhabitants of areas contaminated with DWW have been reported to face several problems, including eye irritation, skin allergies, stomach pain, and vomiting sensation. These problems are due to the high concentration of dissolved impurities such as sulphates, carbonates, calcium chloride, bicarbonate, and magnesium ions (Chowdhary et al., 2018). The presence of the toxic melanoidins has also been reported to indirectly/directly cause severe health problems. Table 2.4 gives the various constituents/pollutants of DWW and the possible environmental and health impacts.

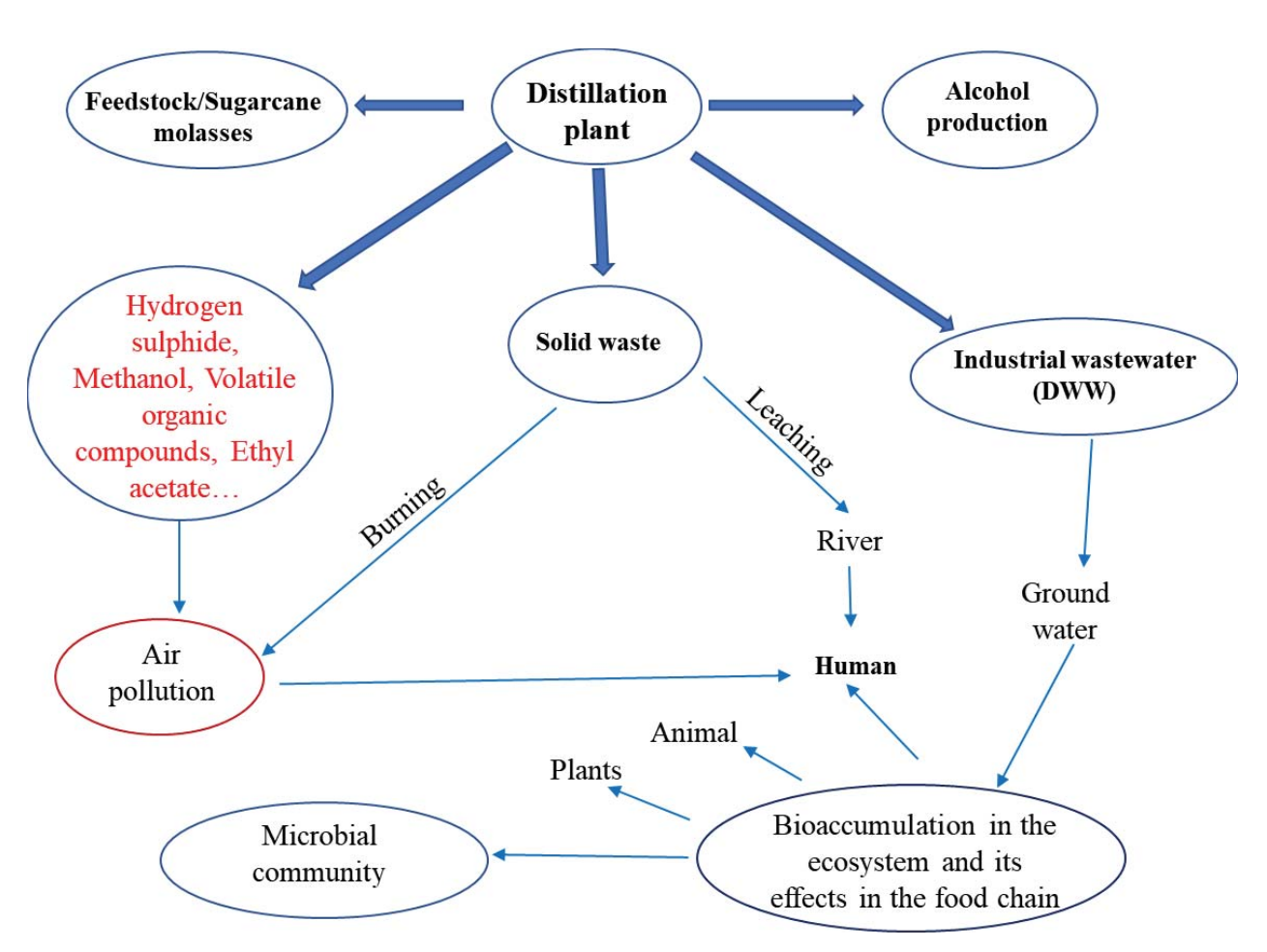


Figure 2.3: Environmental impact of distillery wastewater (Chowdhary et al., 2018).

Table 2.4: Potential impacts of distillery wastewater on the environment and human health

| Constituent | Indicators | Effects | | |
|----------------|---------------------------------------|---|--|--|
| Organic matter | BOD and COD | Oxygen depletion causing the death of aquatic life including fish odours resulting from uncontrolled anaerobic digestion | | |
| Acidity | рН | Extreme pH causes the death of aquatic life Affects microbial activity in biological wastewater remediation processes Hinders crop growth | | |
| Nutrients | Nitrogen, potassium, phosphorus | Eutrophication of water bodies leading to bad odours in lagoons Nitrite and nitrate in drinking water can intoxicate infants | | |
| | | Can be toxic to crops when in large quantities | | |
| Salinity | Electrical | Hinders water uptake by plants | | |
| | conductivity, TDS | Causes bad tastes to water | | |
| | | Toxic to aquatic life including microorganisms | | |
| Solids | Turbidity, TDS | Reduces oxygen uptake due to reduced soil porosity | | |
| 501145 | raioian, 125 | Hinders light penetration in aquatic systems | | |
| Melanoidins | Colour | Cytotoxic, mutagenic and carcinogenic effects on human cells | | |
| | | Eye irritation in humans | | |
| | | Increased immunogenicity | | |
| Heavy metals | Chromium, | Neurotoxicity | | |
| Heavy metals | cadmium, zinc | Toxic to animals and plants | | |

Adapted from Kharayat. (2012), Chowdhary et al. (2018) and Fuess et al. (2018).

2.2 Municipal wastewater and waste activated sludge

Municipal wastewater (MWW), also known as sewage, includes liquid waste generated from institutions and residences, usually discharged through pipes or sewer systems. The MWW contains a mixture of wastewater generated from different domestic sources such as from showers, sinks, kitchen, and toilets. MWW is mainly composed of water with a small concentration of dissolved and suspended inorganic and organic matter. The main components of organic matter include lignin, carbohydrates, fat, proteins, and detergents. In addition to the organic and inorganic matter, bacteria, helminths, protozoa, and pathogenic viruses are likely to be present MWW (Shivaraju, 2011). To prevent environmental pollution and overcome the increasing pressure on water resources, the reclamation of MWW has been considered. This can be achieved through the widely used conventional municipal wastewater treatment systems. There are several stages of treatment for MWW, which are, preliminary, primary, secondary, and tertiary, as depicted in Figure 2.4 (Hreiz et al., 2015). The preliminary stage includes screening and grit removal where big solids such as rags that would interfere with mechanical equipment are removed. Grit removal ensures the separation of sand-like heavy solids that usually settle in channels, thereby interfering with treatment processes.

The primary stage of treatment involves sedimentation of the screened and de-gritted wastewater stream to remove settleable solids (particulate pollutants). In this stage, more than half of the suspended solids are removed. The residue from primary treatment is a concentrated suspension of particles in water called primary sludge. The biodegradability of primary sludge is high and, thus, can be easily treated through biodegradation (Wang et al., 2017). Although the goal of the primary stage is to separate the readily-removable suspended solids, dissolved and colloidal wastes are not sufficiently removed, thus calling for a secondary treatment (Hreiz et al., 2015). The secondary MWW treatment stage is accomplished using a biological treatment process. Microorganisms in suspension (in the activated sludge process) attached to media (in a "trickling filter" or one of its variations) or in ponds or other processes are used to remove biodegradable organic material (Naidoo, 1999). Given its high efficiency, low cost, and simple operation, the activated sludge process (AST) is nowadays the most widely used biological secondary treatment method (Hreiz et al., 2015).

During the biological treatment in AST (Figure 2.4), part of the organic material is oxidized by the microorganisms to produce carbon dioxide and other end products, and the remainder provides the energy and materials needed to support the microorganism community (Naidoo, 1999; Zhen et al., 2016). The microorganisms biologically flocculate to form settleable particles and following biological treatment and this excess biomass is separated in secondary sedimentation tanks as a concentrated suspension called secondary sludge (also known as "biological sludge, waste activated sludge, or trickling filter humus) representing 1-2% of the total treated wastewater volume (Abelleira et al., 2012: Zhen et al., 2016). A major drawback of the AST system is the generation of the waste activated sludge (WAS) in large quantities (Manterola et al., 2008). The WAS consists of easily decomposable organic matter, pathogens, heavy metals, and toxic chemicals, thus posing the risk of secondary environmental pollution (Yuan et al., 2016). The remediation of the excess WAS is a major challenge legally, environmentally, and economically (Manterola et al., 2008). WAS treatment and disposal accounts for up to 60% of the total operational cost and 40% of the total greenhouse gas (GHG) emissions from wastewater treatment processes (Naddeo et al., 2009: Anjum et al., 2016;).

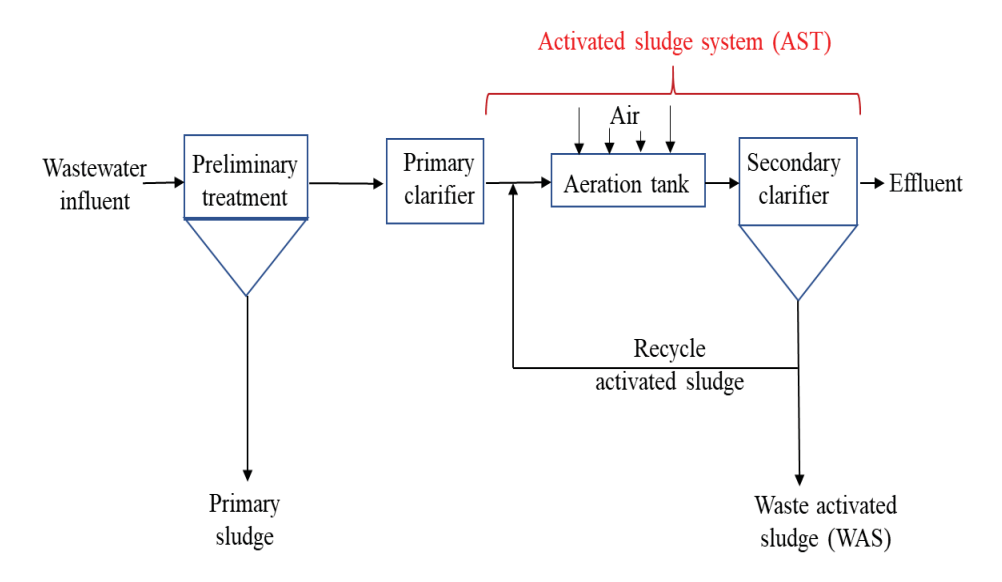


Figure 2.4: Basic flow diagram of a municipal wastewater treatment system employing an activated sludge system.

2.2.1 General characteristics of waste activated sludge

The WAS is mainly composed of microbial cells and biomass produced during the AST process. Overall, the biomass component of WAS contains proteins (30%), carbohydrate (40%), and lipids (30%) in particulate forms (Anjum et al., 2016). Table 5 presents the general physicochemical properties of WAS. Municipal WAS contains a high concentration of organic matter in the form of COD, as shown in Table 2.5 (Shao et al., 2013). Also present in WAS are nutrients such as nitrogen and phosphorus and heavy metals, including zinc, copper, nickel, lead, mercury, and chromium (Anjum et al., 2016).

Table 2.5: Physicochemical characteristics of waste activated sludge

| Parameter | Concentration | | | | |
|-------------------------|---------------|-------|-------|--|--|
| | WASa | WASb | WASc | | |
| pH | 6.38 | 6.7 | 6.83 | | |
| Total solids (g/L) | 22.87 | 7.48 | 7.48 | | |
| Volatile solids (g/L) | 17.26 | 5.0 | 5.0 | | |
| Total COD (g/L) | - | 18.24 | 16.25 | | |
| Soluble COD (g/L) | | 1.75 | - | | |
| Total nitrates (mg/L) | 1523 | - | - | | |
| AN (mg/L) | 197.7 | 5006 | 132.6 | | |
| Total phosphates (mg/L) | - | - | - | | |

^aShao et al. (2013), ^bLiu et al. (2013), and ^cLiu et al. (2015).

2.2.2 Special characteristics of waste activated sludge

The WAS is a multiphase medium constituting a variety of components including a large amount of water, particles (organic and inorganic) bacterial species, microbial aggregates, and extracellular polymeric substances (EPS), as shown in Table 2.6 (Zhen et al., 2017). The composition of the WAS varies based on the type and origin of constituents of the influent wastewater. The EPS originating from the AST microbial processes/or from the influent wastewater constitutes a major part of the WAS organic fraction. The EPS is mainly composed of polysaccharides (PS), proteins and humic substances accounting for up to 80%, in addition to uronic acids, lipids, nucleic acids and some inorganic complexes (Sheng et al., 2010; Anjum et al., 2016). EPSs are present in the interior part of microbial aggregates and outside of cells and are divided into three categories consisting of loosely bound (LB-), tightly bound (TB-) and slime (S-) EPS (Sheng et al., 2010).

Table 2.6: Average special characteristics of waste activated sludge (adapted from Zhen et al. (2017)

| Parameter | Units | Concentration |
|-----------------------------|--------------|---------------|
| VSS/SS | | 0.75 |
| Proteins | mg/g SS | 346 |
| Polysaccharides | mg/g SS | 101 |
| Humics | mg/g SS | 58 |
| Total EPS | mg/g SS | 130 |
| EPS proteins | mg/g SS | 76 |
| EPS polysaccharides | mg/g SS | 11.9 |
| EPS humics | mg/g SS | 36 |
| Iron | mg/L | 213 |
| Calcium | mg/L | 362 |
| EPS surface charge | meq/g SS | 0.33 |
| Zeta-potential | mV | -29.6 |
| Sludge surface charge | meq/g SS | 0.13 |
| Floc size | μm | 53 |
| Surface area C _s | $(m^2/g SS)$ | 15.6 |

The S-EPS, which consists of slimes, colloids, and soluble macromolecules, are uniformly distributed in the aqueous phase. The LB-EPS (loosely bound polymers, sheaths, and condensed gels), which extends from TB-EPS are characterized by a porous dispersible structure while the TB-EPS (attached organic materials) comparatively adheres to the bacterial cell surface inside the sludge flocs (Sheng et al., 2010; Li et al., 2013;). A basic sketch of the

EPS structure is given in Figure 2.5. The surface physical and chemical properties of WAS matrices are governed by the gel-like, three dimensional EPS bipolymers, which provide a protective shielding. The shielding prevents cell lysis and rapture thereby influencing the functional integrity, flocculation, strength, biodegradability, and dewaterability of the sludge (Zhen et al., 2017).

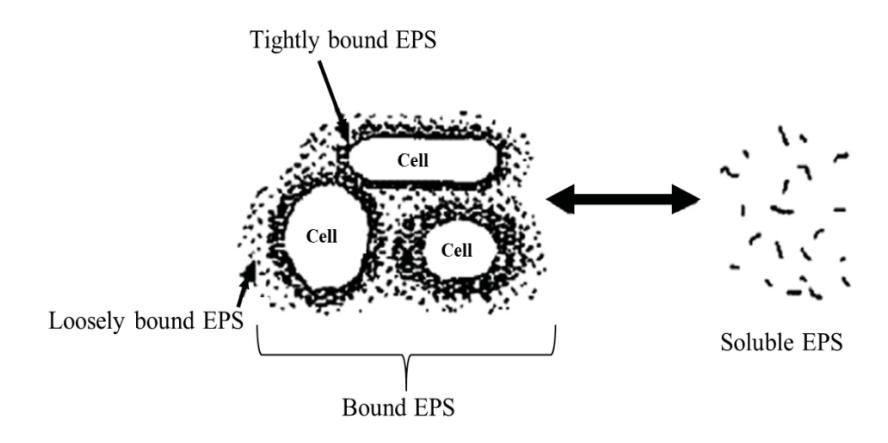


Figure 2.5: A sketch of EPS structure (adapted from Sheng et al., 2010)

2.2.3 Effects of waste activated sludge

The wide application of the AST process in wastewater treatment has led to the generation of large amounts of WAS. The WAS is linked to the major issues of high cost and difficulty of sludge treatment, and limited sludge disposal options. WAS in its original form emits a bad odour, contains pathogenic microorganisms (parasite eggs, enterovirus, pathogenic bacteria), harmful heavy metals (Pb, Cr, Hg, Cd) and refractory organic compounds (pesticides, chlorophenols, nitro-aromatic compounds) (Zhang et al., 2018). Moreover, hazardous pollutants including endocrine disrupting compounds (EDC), nonylphenol (NP), and bis (2-ethylhexyl) phthalate (DEHP), are retained in the sludge and may cause severe environmental risks (Guan et al., 2018). WAS must, therefore, be remediated to a more safe state to avoid environmental pollution and human health impacts (Semblante et al., 2017).

2.3 Anaerobic digestion treatment of distillery wastewater and waste activated sludge

Anaerobic digestion (AD) is widely applied as a first step treatment technique for several industrial wastewaters and forms an integral part of most modern wastewater treatment plants (Van Zyl et al., 2008; Apollo and Aoyi, 2016). Desirable features of AD include low energy and nutrient requirements, ability to operate at a high organic loading rate (OLR), an environmentally friendly technology, and bioenergy production. These features make AD a

feasible option for the treatment of high strength industrial wastewaters such as DWW and WAS (Abelleira-Pereira et al., 2015; Apollo and Aoyi, 2016). The removal of biodegradable organic matter during AD is determined by several factors including (i) the composition and nature of organic matter, (ii) environmental conditions, (iii) sludge retention in the AD reactor, (iv) mixing intensity, and (v) organic matter loading. Factors (i) and (ii) depend on the characteristics of the wastewater while (iii) to (v) relate to the design and type of AD treatment system. AD consists of a series of biological steps in which biodegradable organic matter is broken down by microorganisms in the absence of oxygen. The biological process can be distinguished into four different steps of hydrolysis, acidogenesis, acetogenesis, and methanogenesis (Braguglia et al., 2015).

2.3.1 Overview of the anaerobic digestion process

The AD process is a multi-step process consisting of parallel and series reactions, proceeding in the four successive stages of (i) hydrolysis, (ii) acidogenesis, (iii) acetogenesis, and (iv) methanogenesis as depicted in Figure 2.6 (Adekunle and Okolie, 2015). The overall bioconversion process involves direct and indirect interactions between varying groups of bacteria, where the product of one group is the substrate for another group. This creates a balance between the bacterial population and food/substrate concentration, which must be maintained.

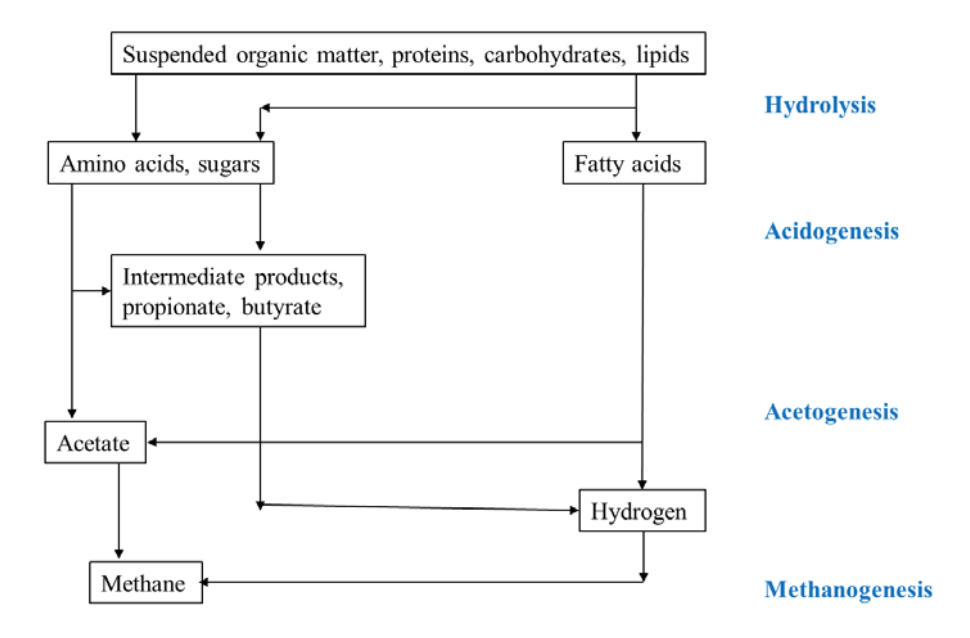


Figure 2.6: Reaction steps of anaerobic digestion of complex organic matter.

Hydrolysis is the first step of AD and is necessitated by the inability of bacteria to take up organic matter in particulate form (Adekunle and Okolie, 2015). In the surface phenomenon hydrolysis step, enzyme-mediated processes such as the disintegration of flocs, solubilization of insoluble organic materials, rapture of hard cell walls, and degradation of extracellular polymeric substances occur, releasing readily available organics which can cross the cell barrier (Braguglia et al., 2015). In the enzymatic process, proteins, lipids, and polysaccharides are hydrolyzed to amino acids, long chain fatty acids, and simple sugars, respectively. Hydrolysis of insoluble organic matter such as carbohydrates and suspended solids is the rate-limiting step for the overall AD process (Adekunle and Okolie, 2015; Yuan et al., 2016). In the subsequent acidogenic step, the soluble hydrolysis products consisting of amino acids and sugars are diffused through the cell membrane and converted through fermentation into organic acids (mainly volatile fatty acids, VFAs), hydrogen (H₂), carbon dioxide (CO₂) and ammonia (NH₃). Acidogenesis, which is a common reaction, is carried out by a group of hydrolytic and non-hydrolytic microorganisms (Buys, 2015).

In the third step of acetogenesis, the short chain fatty acids (except acetate) are further converted into acetic acid alongside additional H₂, CO₂ and NH₃ by the acetogenic bacteria. The two most important substrates for acetogenic bacteria are butyrate and propionate and are also key to the AD process (Buys, 2015). In the last step of methanogenesis, methanogenic bacteria convert the products from acetogenesis to CO₂ and methane (CH₄). A group of methanogenic archaea reduces the CO₂ using H as the electron donor and decarboxylate acetate, forming CH₄. It is at this final stage where the influent COD is converted to a gaseous form that leaves the digester system (Adekunle and Okolie, 2015; Braguglia et al., 2015).

2.3.2 Anaerobic reactors

Anaerobic lagoons offer the simplest option for anaerobic treatment of wastewater, including DWW. However, the lagoons suffer from large area requirements, higher chances of groundwater pollution, and odor problems (Satyawali and Balakrishnan, 2008). A recent phenomenon arising from new reactor designs has led to the successful and economic use of anaerobic digesters for liquid waste treatment. Several new configurations of high-rate anaerobic reactors such as filter bed, packed bed, fluidized bed, suspended bed, contact processes, and sludge blanket have allowed for higher retention of biomass concentration than traditional digesters (Zinatizadeh et al., 2017). In these high-rate reactors, where liquid retention and biomass retention are uncoupled, physical retention and /or immobilization of

anaerobic sludge allows for high sludge concentrations. The high biomass concentration allows for the application of high organic loading while maintaining short hydraulic retention times (HRTs). The performance of several high rate anaerobic reactors at the laboratory and commercial scales is summarised in Table 2.7.

Table 2.7: Performance of high rate anaerobic reactors

| Reactor configuration | COD loading (kg COD m ⁻¹ day ⁻¹) | HRT (days) | COD reduction (%) |
|--|---|------------|-------------------|
| UASB ^a | 24 | | 75 |
| UASBa | 15 | 2.1 | 90 |
| UASB ^a | 18 | | >90 |
| $UASB^b$ | 11 | | >92 |
| Diphasic fixed film ^a | 22 | 3 | 71.8 |
| Hybrid baffled reactor ^a | 20 | | 77 |
| Up-flow fixed bed reactor ^c | 11 | 28 | >75 |
| Downflow fludized beda | 4.5 | | 85 |
| Upflow blanket filter ^a | 9-11 | 11-12 | 70 |

Key: UASB – Upflow anaerobic sludge blanket

Of all the high rate anaerobic reactors, the upward flow anaerobic sludge blanket (UASB), which is a suspended bed reactor, offers several advantages such as high COD removal efficiencies greater than 80%, high organic loading rates (OLR) of 5 to 20 kg CODm⁻³d⁻¹, methane yields of up to 400 ml CH₄/gram of COD removed, low energy consumption, reduced excess sludge, stable operation under extreme conditions and simplicity in operation (Lopez-Lopez et al., 2015; Zinatizadeh et al., 2017). The success of UASB depends on the formation of active and settleable granules. These granules consist of an aggregation of anaerobic bacteria, self-immobilized into compact forms. This enhances the settleability of biomass and leads to effective retention of bacteria in the reactor. Particularly attractive features of the UASB reactor design include its independence from mechanical mixing of digester contents, recycling of sludge biomass, and ability to cope up with disturbances caused by the high loading rates and temperature fluctuations that are modified (Chen et al., 2015). A schematic diagram of the UASB reactor is presented in Figure 2.7.

^aSatyawali and Balakrishnan (2008), ^bChen et al. (2017) and ^cApollo et al. (2013)

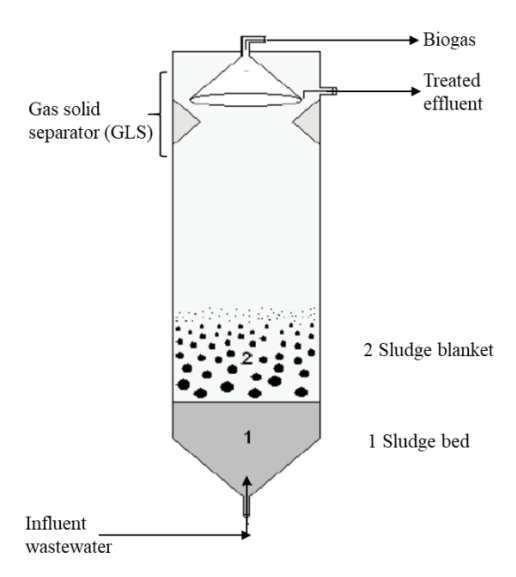


Figure 2.7: A schematic diagram of a UASB reactor.

2.3.3 Kinetic modelling of anaerobic digestion

The application of kinetic models to the anaerobic process is important in predicting the performance and optimization of digesters, in determining the relationships between variables and predicting the formation of the product. Moreover, the models could allow for a good understanding of the reaction mechanisms involved, thereby reducing the laborious and complex process of obtaining experimental data (Yetilmezsoy, 2012). Several kinetic models have been applied in the anaerobic treatment of varying wastewater streams. Models such as first order, Monod-type, Grau second order multi-component, Chen-Hashimoto, Contois, pseudo-mechanistic, Haldane, Stover-Kincannon, Sundstrom, Dewall and Chian, Benjes, and Young and McCarthy, have been applied to explore the biokinetics and identify important relationships between the design data and obtained experimental results (Sosnowski et al., 2008; Siles et al., 2008; Vavilin, 2010; Wardhani, 2017). For industrial application purposes, easily monitored simplified kinetics involving few parameters are needed (Işik and Sponza, 2005).

Most kinetic studies of anaerobic digestion have been based on the Monod, and first-order models with satisfactory practical application reported (Siles et al., 2008; Wardhani, 2017). The Monod models have allowed for the successful prediction of the performance of a UASB reactor treating slaughterhouse (Borja et al., 1994) and ice-cream (Borja and Banks, 1994) wastewaters. Despite the success of the Monod model, it has been found inapplicable to some systems where the effluent COD is not independent of the influent substrate concentration. This has led to the development of additional models such as Contois and Chen and Hashimoto,

which would be more suitable in predicting the process kinetics performance of anaerobic digesters (Hu et al., 2002). The additional models with multi-culture system kinetics are desirable based on the heterogeneity of the microbial population, which brings about several bioconversion steps involved. The various kinetic models used for anaerobic digestion are given in the Appendix A.

2.3.4 Limitations of anaerobic digestion

Despite being considered an economic and environment-friendly technology forming an integral part of modern wastewater treatment plants, AD suffers from certain limitations depending on the wastewater substrate type. In the case of WAS, AD suffers high retention times, low methanogenic production, and an overall 30-35% dry solids degradation in mesophilic conditions (Ali Shah et al., 2014). The low solids degradation is caused by the EPS protecting the structure of sludge, which is difficult to hydrolyze and digest in the process affecting the sludge biodegradability (Zhen et al., 2017). The waste activated sludge consists of heterotrophic bacteria not easily biodegradable, complex floc structure, hard cell wall, and large organic molecules which cannot be absorbed by microorganisms. The hard cell wall consisting of microbial cells inside extracellular polymers is a physical barrier that does not allow intracellular organic compounds to be biodegraded easily (Abelleira-Pereira et al., 2015). A large amount of energy is therefore required for the rapture of the bacterial cell envelope, thereby limiting the hydrolysis step (Bougrier et al., 2006). The low performance of the hydrolytic microorganisms is also contributed to by other factors such as the presence of recalcitrant lipids and proteins (Abelleira-Pereira et al., 2015). The hydrolysis step limits the rate of AD during the degradation of the complex organic substrate, such as the WAS, and the consequent biogas generation (Yuan et al., 2016). These limitations are the inherent consequences of low performance by microorganisms responsible for the processes involved in AD.

In the AD of DWW, the presence of the biorecalcitrant melanoidin compounds and suspended solids hinders the rate determining hydrolysis step (Chaiprapat and Laklam, 2011). Melanoidins, due to their polymeric nature and the high molecular weight (usually > 5.0 kDa) are anti-oxidative and thus recalcitrant to biodegradation (Liang et al., 2009; Liu et al., 2013). The recalcitrant nature of the melanoidin pigment is shown by the fact that it escapes from the conventional anaerobic wastewater treatment and finally ends up in the environment in the form of the coloured effluent. Only 6% to 7% melanoidin degradation has been achieved in

the anaerobic treatment processes (Satyawali & Balakrishnan, 2008; Ojijo et al., 2010). Moreover, in most instances during anaerobic digestion, the melanoidin compounds repolymerise thereby intensifying the colour of the anaerobically digested effluent (Mabuza et al., 2017). Thus, whereas the AD process can be effectively applied in removing the organic load of DWW, the biorecalcitrant characteristic brown colour remains unabated (Apollo and Aoyi, 2016).

The conventional anaerobic treatment system can effectively reduce the high organic load of most wastewaters but has been found to suffer some serious limitations. The increased industrial and human activities have led to the generation of wastewaters with varied characteristics and emergence of organic pollutants not amenable to conventional biodegradation. There is, therefore, an increasing concern for the development of effective treatment technologies to remove the low biodegradable and chemically stable pollutants. Advanced oxidation processes (AOPs) are highly competitive techniques that can remove recalcitrant pollutants (Oller et al., 2011).

2.4 Advanced oxidation processes

Advanced oxidation processes (AOPs), which are categorized under chemical treatment, are usually employed in oxidizing biorecalcitrant organic compounds/pollutants into simpler inorganic/organic end products (Otieno et al., 2017; Mecha et al., 2016). The AOPs are the most attractive substitutes for other alternative processes such as coagulation-flocculation, adsorption, and membrane technologies that would otherwise lead to secondary pollution in the form of sludge generation (Gnanaprakasam et al., 2015). The advanced oxidation proceeds through two routes, oxidation with O₂ and the use of high energy oxidants including ozone (O₃) and hydrogen peroxide (H₂O₂) and photons leading to the generation of highly reactive hydroxyl radicals (HO•) (Munter, 2001). The AOPs are mainly based on the generation of free hydroxyl radicals (HO•), a non-selective and powerful oxidant. The (HO•) radical has the highest relative oxidation activity in comparison to other oxidants, as shown in Table 2.8.

Table 2.8: Relative oxidation activity of common oxidants (Munter, 2001)

| Oxidant | Relative oxidation activity |
|-------------------|-----------------------------|
| Hydroxyl radical | 2.05 |
| Atomic oxygen | 1.78 |
| Ozone | 1.52 |
| Hydrogen peroxide | 1.31 |
| Chlorine | 1.00 |

2.4.1 The basic principle of AOPs

The HO[•], the most oxidizing agent known, rapidly reacts with most organic compounds with very high rate constants up to the order of 10¹¹ M⁻¹s⁻¹, as shown in Table 2.9. The radical can attack different organic species by radical addition/combination, electron transfer, and hydrogen abstraction. In radical addition, according to (Eq. 2.1), HO[•] reacts with aliphatic and unsaturated organic compounds producing organic radicals, which are further oxidized by ferrous iron or oxygen forming stable end products. In hydrogen abstraction according to (Eq. 2.2), hydrogen is removed by the generated HO[•] from an organic compound forming an organic radical. This initiates a chain reaction involving the reaction between the organic radical and oxygen, producing a peroxyl radical capable of reacting with another organic compound. Electron transfer (Eq. 2.3) leads to the formation of higher valent ions, where the oxidation of a monoatomic negative ion results in a free radical or atom. In the fourth route of radical recombination (Eq. 2.4), two radicals combine forming a stable product (Munter, 2001).

Radical addition

$$R + HO^{\bullet} \rightarrow ROH$$
 (2.1)

Hydrogen abstraction:

$$R + HO^{\bullet} \rightarrow R^{\bullet} + H_2O \tag{2.2}$$

Electron transfer:

$$R^{n} + HO^{\bullet} \rightarrow R^{n-1} + OH^{-}$$
(2.3)

Radical combination:

$$HO^{\bullet} + HO^{\bullet} \rightarrow H_2O_2$$
 (2.4)

Some of the widely employed AOPs include non-photochemical (Fenton oxidation and ozonolysis) and photochemical (photo Fenton oxidation and photocatalysis) methods (Liu et al., 2013; Amat et al., 2014).

Table 2.9: Relative oxidation activity of common oxidants (Munter, 2001)

| Organic compound | Rate constants (M/s) | | |
|-----------------------|----------------------|----------------------------------|--|
| | O_3 | НО• | |
| Alcohols | 10-2-1 | 10 ⁸ -10 ⁹ | |
| Aromatics | $10\ 10^2$ | $10^8 - 10^{10}$ | |
| Chlorinated alkenes | $10^3 - 10^4$ | $10^9 - 10^{11}$ | |
| Ketones | 1 | $10^9 - 10^{10}$ | |
| N-containing organics | $10-10^2$ | $10^8 - 10^{10}$ | |
| Phenols | 10^{3} | $10^9 - 10^{10}$ | |

2.4.2 Fenton and photo Fenton

In Fenton oxidation, hydrogen peroxide (H₂O₂) reacts with ferrous ions (Fe²⁺) generating highly reactive hydroxyl radicals (HO•) according to Eq. 2.5. The radicals having a high oxidation potential react with organic compounds/pollutants leading to their mineralization or formation of less harmful products (David et al., 2015; Titouhi and Belgaied, 2016). The second reaction given in Eq. 2.6, also known as photo-Fenton is enhanced by the introduction of UV/Vis light, which leads to the production of additional HO• radicals and the regeneration of the catalyst (David et al., 2015). Due to its ease of application and fast response, the Fenton oxidation process has been used for wastewater treatment including colour removal from DWW and enhanced digestion of WAS (Amat et al., 2014; David et al., 2015; Garcia-Segura et al., 2016). The Fenton process, however, suffers from high sensitivity to operational conditions and may require an additional process to remove iron after treatment. Moreover, the presence of other interfering pollutants in the wastewater may hinder the Fenton process (Liu et al., 2013; Amat et al., 2014; Titouhi and Belgaied, 2016).

$$Fe^{2+} + H_2O_2 \longrightarrow Fe^{3+} + OH^- + OH^{\bullet}$$
 (2.5)

$$Fe^{3+} + H_2O + hv \longrightarrow Fe^{2+} + H^+ + OH^{\bullet}$$
 (2.6)

2.4.3 Photocatalysis

Photocatalysis is a photo-induced reaction that is accelerated by the presence of a semi-conductor catalyst such as titania (TiO_2) or zinc oxide (ZnO). The photocatalytic reaction is initiated by the excitation of the semiconductor by electromagnetic radiation energy more than or equal to the band gap energy of the catalyst. The absorption of energy by the catalyst leads to the promotion of electrons (e^-) from the valence band (VB) to the conduction band (CB) thereby generating a hole (h^+) in the VB, as shown in Figure 4 (Akpan & Hameed, 2009). The

promoted electrons in the CB reduce oxygen to $O_2^{\bullet-}$, while the holes oxidize OH^- or H_2O leading to the formation of hydroxyl radicals (HO^{\bullet}). The radicals further oxidize the organic compounds/pollutants in addition to the minimal direct attack by h^+ .

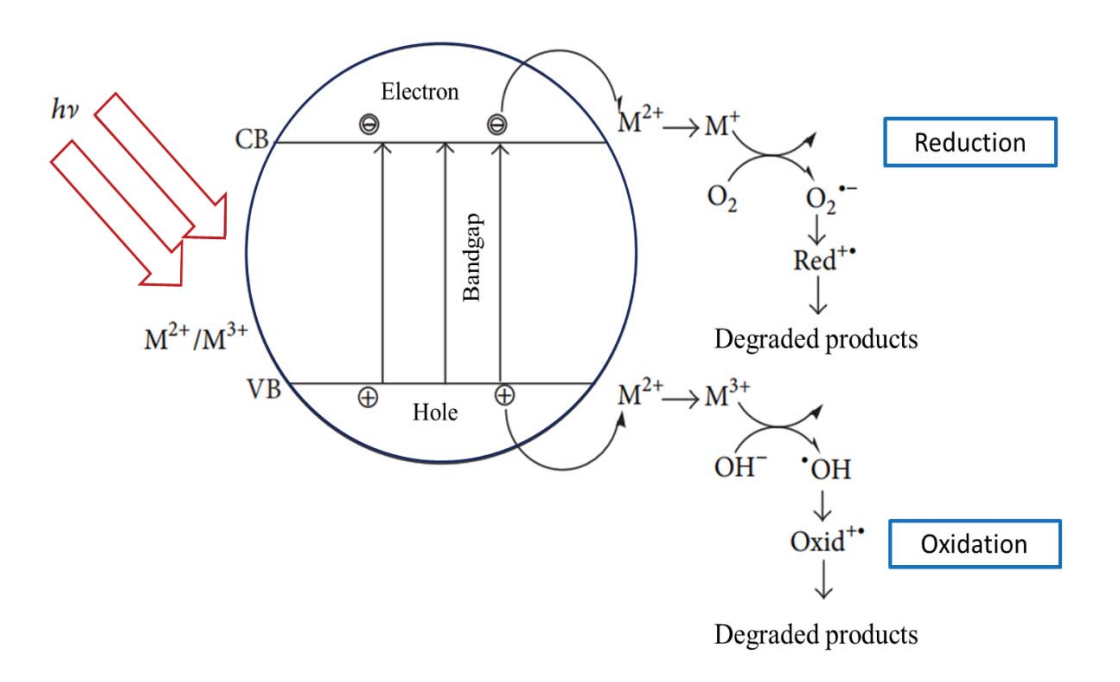


Figure 2.8: Schematic representation of the photocatalytic process (Akpan & Hameed, 2009)

The photocatalytic process can be combined in various ways forming hybrid systems that reduce the degradation time while increasing the scope of application. Apollo et al. (2014) used UV/H₂O₂/TiO₂/Zeolite hybrid system for the treatment of molasses wastewater for COD and colour. Navgire et al. (2012) successfully photodegraded molasses wastewater using a synthesized nanocrystalline composite of TiO₂ and MoO₃. The composite showed higher activity as compared to the TiO₂ and MoO₃ catalysts when used on their own.

2.4.4 Ozonolysis

Ozone gas (O₃) has a pungent smell with a moderate water solubility (110 mg/L at 25°C) (Travaini et al., 2016). The reactive O₃ (E = 2.07 V at 25°C) can be generated from air/oxygen via a high voltage corona discharge process. Due to its molecular electronic configuration, which makes it unstable, ozone once dissolved in water self decomposes and undergoes oxidation reactions. Ozonolysis has several advantages over other AOPs including (i) ability to remove turbidity, odour, taste, and colour, (ii) improved anaerobic degradation efficiency of several substrates at low temperatures and basic pH, (iii) easy installation and operation, (iv) control of waterborne pathogens, (v) oxidation of organic and inorganic compounds, and (vi)

fast decomposition of residual ozone to oxygen thus minimizing effects on the downstream processes (Sangave et al., 2007; Takashina et al., 2018). Ozonolysis of distillery wastewater has been tried to evaluate the process based on organic matter removal and decolourisation efficiencies. Ozone generation was based on the reaction of oxygen with UV light (Singh & Dikshit, 2012). The reaction mechanisms for photocatalysis and ozonolysis are given in Appendix B.

2.5 Simulation and modelling of reactors

Reactor modelling is usually divided into three parts: hydrodynamics, light intensity distribution, and reaction kinetics modelling (Boyjoo et al., 2013). In photoreactor modelling, hydrodynamics studies are used to analyse the distribution of catalyst particles in the reactor. Then, radiation field modelling is carried out to determine the light distribution in the photoreactor. Reaction kinetics modelling is then carried out to calculate the rate of photocatalysis.

2.5.1 Hydrodynamics

The bubble, catalyst, and wastewater flow in the reactor is the subject of reactor hydrodynamics. The fluidized bed photocatalytic reactor is a multiphase reactor with turbulent flow. The hydrodynamics modelling of fluidized bed photoreactors is like that of any fluidized bed photoreactor. An accurate analysis of the hydrodynamics in such a reactor cannot be determined analytically; instead, computational fluid dynamics (CFD) is normally used to model such a reactor due to its accuracy at low cost (Boyjoo et al., 2013). In CFD simulation, the reactor geometry is divided into a grid of several cells. The system of partial differential equations that govern fluid flow are the solved algebraically within the grid.

CFD hydrodynamics modelling of multiphase fluidized bed photoreactors can be carried out using either Eulerian or Langrarian models. In the Langrarian models, the distribution of phases is carried out through the tracking of individual phase particles. Langrarian modelling is very accurate; however, it is very computationally costly. An alternative model, the Eulerian model, treats the different phases as interpenetrating continua. The Eulerian model has been widely used to model fluidized bed reactors due to its accuracy and robustness at a low computational cost (Boyjoo et al., 2013). In the Eulerian model, the continuity and momentum equations are solved for all phases.

The turbulence in a multiphase reactor is normally solved using the k-ɛ equation due to its lower computational requirements and good accuracy. In case better accuracy is required, especially for swirling flows, reynolds stress models (RSM) can be used at higher computational cost. Momentum transfer between the gas, solid and liquid phases are usually accounted for by introducing drag forces. Other interfacial forces such as lift, virtual mass, and turbulent dispersion forces can also be included in the solution. A few studies have reported the hydrodynamics of fluidized bed photocatalytic reactors. Boyjoo et al. (2014) analysed the hydrodynamic of an annular pilot scale reactor with nanophase catalysts under air fluidization. Qi et al. (2011) investigated the hydrodynamics of an annular slurry bubble photocatalytic reactor.

2.5.2 Light intensity distribution

In addition to hydrodynamics, light photons travel in the reactor, where they interact with catalysts, bubbles, and reactor walls. This distribution of light in a photocatalytic reactor is always inhomogeneous (Camera-Roda et al., 2016). An analysis of the light distribution in the reactor is crucial as it is the basis of such important photocatalytic reactor design parameters such as the local volumetric rate of energy absorption (LVREA), photocatalysis intrinsic kinetics and efficiency parameters (Moreira et al., 2010). The LVREA determines the amount of light absorbed at specific points in the reactor which can be used to predict the local reaction rate. Experimental determination of the light distribution at every point in the reactor is not feasible due to the considerable amount of time that would be required. Instead, light distribution is usually established using validated models.

The most rigorous light distribution models solve the radiation transport equation (RTE) (equation 2.34). For photocatalysis systems, the scattering terms in the right-hand side of the RTE renders an analytical solution to the RTE impossible. Therefore, numerical methods have been developed for solving the RTE. The most rigorous of these numerical methods are the deterministic discrete ordinates/finite volume methods (Boyjoo et al., 2014) and the stochastic Monte Carlo method (Moreira et al., 2010; Valadés-Pelayo et al., 2014). Methods with several simplifying assumptions, such as the six-flux method (Li Puma et al., 2010) and P1 method (Orozco et al., 2009), have also been used to solve the RTE.

$$\frac{dI_{\lambda}(s,\Omega)}{ds} = -\kappa_{\lambda}I_{\lambda}(s,\Omega) - \sigma_{\lambda}I_{\lambda}(s,\Omega)
+ \frac{1}{4\pi}\sigma_{\lambda} \int_{0}^{4\pi} p(\Omega' \to \Omega)I_{\lambda}(s,\Omega')d\Omega'$$
(2.7)

where I_{λ} is a beam of light of wavelength λ travelling in direction Ω and distance s; κ_{λ} and σ_{λ} are the absorption and scattering coefficients of the medium, respectively; $p(\Omega' \to \Omega)$ is the scattering phase function which determines the probability that light from the direction Ω' will be scattered to direction Ω .

The accuracy of the Monte Carlo method for light distribution simulation has been highlighted by several researchers (Moreira et al., 2010; Valadés-Pelayo et al., 2014). The Monte Carlo method solves the RTE stochastically by tracking a statistically adequate number of photons from the lamp until they are absorbed in the slurry or lost in the reactor wall. Several studies have employed the Monte Carlo method to determine the light distribution in liquid fluidized bed photocatalytic reactors. Imoberdorf et al. (2008) used the Monte Carlo method to determine the light distribution in a fluidized bed reactor with TiO₂ coated spheres. Moreira et al. (2010) and Valadés-Pelayo et al. (2014) developed a Monte Carlo algorithm for establishing the light distribution in a slurry photocatalytic reactor with nanosized TiO₂ catalysts.

2.6 Integrated anaerobic digestion and advanced oxidation processes

Anaerobic digestion is considered the most promising technology of all other conventional biological treatment methods. The advantages of AD include sludge volume reduction (30-70%), bioenergy production, and reduced greenhouse gas emissions (Toczyłowska-Mamińska, 2017). However, AD suffers from limitations such as the inability to remove biorecalcitrant melanoidin compounds in DWW and long retention time during the degradation of WAS (Chaiprapat and Laklam, 2011). To effectively remove the colour, biorecaciltrant compounds, emerging pollutants, and the organic load, integrating the AD with other techniques becomes inevitable. In this context, the advanced oxidation processes (AOPs) such as ozonolysis and photodegradation are highly competitive techniques that can enhance or complement the AD process either as pre- or post-treatment techniques. These AOPs usually come with high costs, but their application alongside the widely used anaerobic digestion can significantly reduce the overall cost of operation (Oller et al., 2011; Brooms et al., 2018).

The integration is aimed at enhancing the AD process leading to maximum biogas recovery and ensuring that an effluent that complies with the set discharge standards is obtained. In integrating AD with AOPs, the overall aim should be to reduce cost by minimizing AOP treatment and maximizing the AD stage. Although the energy requirement plays a major role in selecting an appropriate pretreatment method, the primary aim for the case of substrates such as WAS should be to disintegrate sludge components and disrupt cell walls rendering the WAS components more accessible to the anaerobic treatment (Anjum et al., 2016). It is thus important to take into consideration the characteristics of each treatment step and its effect on the ensuing steps (Oller et al., 2011).

2.6.1 Advanced oxidation pre-treatment

Appropriate pre-treatments such as photocatalytic degradation and ozonolysis (AOPs) can improve the AD performance by breaking flocs and solubilizing particulates, improving microbial cell lysis and bioavailability, thereby accelerating the hydrolysis step (Braguglia et al., 2015). The photodegradation process is less selective and, therefore, not recommended for application as pre-treatment to AD. This is because of possible competition between the biodegradable components and the recalcitrant compound during photodegradation, resulting in a longer period of UV irradiation and high chemical consumption. Moreover, the highly turbid raw industrial DWW/WAS will hinder light penetration, thus limiting photodegradation (Apollo and Aoyi, 2016). Ozonolysis has been reported to improve wastewater biodegradability and hence it is suitable for application as a pre-treatment. Moreover, ozonolysis involves bubbling of ozone gas through the wastewater hence is minimally hindered by turbidity (Achisa et al., 2016). Through ozonolysis, biorecalcitrant polymeric HMW organic compounds can be broken down into easily biodegradable low molecular weight (LMW) compounds (Santos et al., 2013). During ozonolysis, the suspended organic matter can be released from the sludge in WAS into the solution as a result of the breaking and solubilization of the hard cellular membrane (Liu et al., 2017). Also, the low soluble volatile organic compounds (VOCs) in WAS can be oxidized and solubilized as well, thus contributing to improved biodegradability (Oller et al., 2011; Wei et al., 2013).

2.6.2 Advanced oxidation post-treatment

The need for time limitation and the high selectivity of some AOP pre-treatments such as ozonolysis can, in some instances, allow the biorecalcitrant compounds not fully ozonized to escape into the subsequent AD process and later into the digester effluent. Moreover, in the case of DWW, the repolymerisation of the colour causing melanoidins during AD may lead to the generation of a colour intense effluent (Apollo et al., 2013; Otieno et al., 2016; Mabuza et

al., 2017). In such instances, a further robust post-treatment method would be needed for the anaerobically digested effluent to ensure complete removal of the remaining micropollutants (Oller et al., 2011). The ozonolysis process still presents the best route for AD-posttreatment. Through ozonolysis, the biorecalcitrant polymeric HMW colour causing melanoidin organic compounds in DWW can be broken down into low molecular weight (LMW) colourless compounds (Santos et al., 2013; Amaral-Silva et al., 2016). The ozonolysis process is also capable of removing pathogens and hence has gained great interest in AD post-treatment (Ariunbaatar et al., 2014).

2.6.3 Factors to consider in an integrated anaerobic-ozonolysis process

The application of prolonged ozonolysis as a pre-treatment method has been reported to lead to the oxidation of biodegradable organic compounds instead of the targeted biorecalcitrant and toxic ones, and the formation of ozone products with a potential to inhibit the subsequent biodegradation process (Gomes et al., 2013; Ariunbaatar et al., 2014). The main role of ozonolysis as pre-treatment should, therefore, be to partially oxidise the biorecalcitrant part and release biodegradable intermediates (Oller et al., 2011). Previous studies have shown that the ozonolysis process is dependent on parameters such as initial pH, initial substrate concentration, ozone dosage, and reaction time (Kasiri et al., 2013; Wan Omar and Amin, 2016; Perrone et al., 2017). In these studies, the optimization of the processes was based on pollutant removal. However, in evaluating the effectiveness of the ozonolysis system, the determination of the efficiency of ozone contact with contaminants becomes a major interest. It is thus important to ensure effective ozone utilization by maximizing contaminants/colour removal while minimizing ozone in the off-gas. Recently, ozone transfer efficiencies of 24% and 51-56% have been reported, respectively, for ozonolysis processes treating secondary effluent and lake water (Crousier et al., 2016; Westerhoff et al., 1999). Based on the reported low efficiencies, the designing of processes aimed at maximizing ozone transfer is thus an interesting area of research.

CHAPTER 3: CFD SIMULATION OF FLUIDIZED BED REACTOR

3 Introduction

Fluidized bed reactors are used in photocatalysis to suspend catalyst particles and supply oxygen directly into the reactor. Such reactors are desirable due to their good mixing characteristics with no moving parts and low maintenance. In an air fluidized bed reactor, air induces liquid motion, which then suspends the catalyst. The hydrodynamics in such reactors are characterized by turbulence and multiple forces that influence bubble motion which results in very complex flows. In order to analyse, scale up and optimize fluidized bed reactors, the reactor hydrodynamics must be understood. The use of experimental techniques to analyse the hydrodynamics has been limited by cost and resolution. Instead, numerical methods such as computational fluid dynamics (CFD) have attracted increasing interest due to their mathematical rigour at low cost (Ekambara et al., 2010). Fluid flow in fluidized bed reactors is usually highly turbulent with bubbles and catalysts experiencing multiple forces such as drag, lift, wall lubrication, turbulent dispersion and virtual mass forces (Tabib et al., 2008). Therefore, the choice of the simulation strategies such as turbulent model and interface simulation is very crucial in order to ensure good accuracy at low cost.

The CFD simulation of bubble columns (Kulkarni et al., 2007; Tabib et al., 2008; Ekambara et al., 2010) and general three phase fluidized bed reactors (Schallenberg et al., 2005; Panneerselvam et al., 2009) have been carried out. However, very little has been done on the CFD simulation of the type of the reactor employed in this work: an annular fluidized bed reactor with nanoparticles (Feng et al., 2005; Qi et al., 2011; Boyjoo et al., 2014). In this chapter, the annular fluidized bed reactor employed was simulated using CFD technique. First, the reactor was simulated, and results validated using the experimental data of Kulkarni et al. (2007) to determine the most accurate turbulent models and interfacial forces. Then, the fluidized bed reactor was simulated using the best turbulent model and set of interfacial forces from bubble column simulation. The aim of this chapter was to analyse the catalyst distribution in the reactor using the computational fluid dynamic technique.

3.1 Methodology

3.1.1 Governing equations

In this work, two reactors were simulated: a bubble column reactor for validation and the fluidized bed reactor. The Eulerian model was used to simulate the hydrodynamics in the bubble column reactor. The bubble column and the fluidized bed reactor was simulated using

the two phase and three phase Eulerian models, respectively. The generic governing equations for the hydrodynamics model consisted of the continuity equation and the momentum equation, details of which are given in Appendix C.

3.1.2 Numerical modelling

Both the bubble column and fluidized bed were simulated in 3D using ANSYS CFX 17. CFX was chosen due to its robust solver in which pressure and velocity are solved in a coupled manner.

Bubble column reactor

An air-water bubble column reactor with a diameter of 150 mm and a height of 1000 mm (Figure 3.1) was simulated. The initial static liquid height in the column was 900 mm. A mass flow inlet boundary condition was specified at the air inlet with an air volume fraction of 1. A pressure outlet boundary condition with air backflow volume fraction of 1 was specified at the top of the reactor to keep liquid from exiting the reactor. At the reactor wall, a no-slip condition was specified for the liquid, while for the gas, a free-slip condition was specified. The gas and liquid properties are listed in Table 3.1.

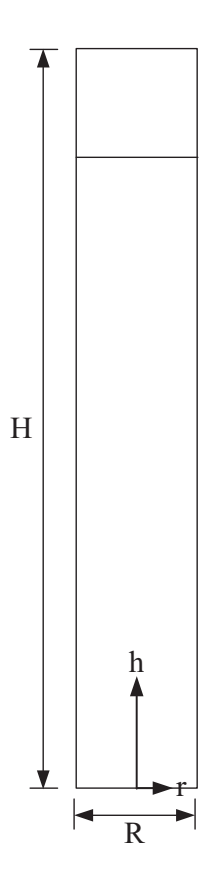


Figure 3.1: Reactor geometry coordinate

Meshing was carried out using ANSYS meshing software with a multizone scheme which utilizes hexahedral mesh for most of the reactor with tetrahedral mesh in areas in which hexahedral mesh cannot be used. The effect of grid size on simulation accuracy was investigated using grid sizes of 6837, 41356, 98264, and 231270 nodes. Due to the geometrical symmetry of the reactor, a full, half and quarter reactor models, along the axial direction, were investigated. The half reactor had one symmetry plane while the quarter reactor had two symmetry planes. Turbulence was modelled using the standard k-ε, RNG k-ε and Reynolds Stress Model (RSM). Most of the interfacial forces such as the drag, lift, wall lubrication, and turbulence dispersion forces, were modelled. Only the virtual mass force was not modelled since it has been found to be insignificant (Tabib et al., 2008; Masood and Delgado, 2014). This is because the acceleration and deceleration of the liquid by bubbles which give rise to the virtual mass force are predominant mainly at the extreme ends of the bubble column.

The governing equations were discretized using element based finite volume method. High-resolution scheme was applied for spatial discretization, while second order backward Euler scheme was used for temporal discretization. A time step of 0.001 s was used for the total simulation time of 120 s with time-averaging of the flow quantities being carried out in the last 100 s. Time averaging was crucial in order to enable comparison with time-averaged experimental data. Also, time-averaged flow properties are of more relevance for engineering purposes than instantaneous flow properties. Convergence was achieved when the mass flow residual dropped below 1.0×10^{-4} .

Table 3.1: Liquid and gas properties

| Property phase | Value |
|---------------------------------|-------------------------|
| Air density (kg/m³) | 1.185 |
| Air viscosity (kg/m s) | 1.7894×10 ⁻⁵ |
| Bubble diameter (m) | 0.006 |
| Superficial air velocity (m/s) | 0.020 |
| Water density (kg/m³) | 997 |
| Water viscosity (kg/m s) | 0.001003 |
| Air-water surface tension (N/m) | 0.072 |

Fluidized bed reactor

The annular fluidized bed reactor with a diameter of 60.6 mm and a height of 750 mm (Figure 3.1) was simulated. The initial static liquid height in the column was 600 mm with a uniform initial solid volume fraction within the liquid phase. The numerical methods for the bubble

column was used, with additional considerations for the solid phase. At the reactor wall, a free-slip condition was specified for the solid phase. In addition to the liquid and gas properties listed in Table 3.1, the required solid properties are listed in Table 3.2.

Table 3.2: Solid phase properties

| Property phase | Value | Reference |
|---|---------------------------------|--|
| Solid diameter (m) | 9×10 ⁻⁷ | Boyjoo et al. (2013) |
| Solid density (kg/m³) Solid volume fraction (-) | 4260 4.7279×10 ⁻⁵ | Boyjoo et al. (2013) |
| Packing fraction (-) Restitution coefficient (-) | 0.55 0 | Boyjoo et al. (2013) Boyjoo et al. (2013) |

Meshing was carried out using ANSYS meshing software with a multizone scheme, which resulted in a grid size of 52 224 nodes for the full reactor (Figure 3.2). Turbulence was modelled using the Reynolds Stress Model (RSM) as this was the best model from bubble column simulation. Most of the gas-liquid interfacial forces such as the drag, lift, wall lubrication, and turbulence dispersion forces were modelled as this was found to give the best results for the bubble column reactor. For the liquid-solid interfacial forces, only the drag force was modelled. The solids pressure due to the presence of the solid phase was modelled using the kinetic theory of granular flow in which the random movement of the solids is accounted for by an analogous comparison to similar movement of gas molecules. The solver settings for the bubble column reactor were retained during the simulation of the fluidized bed reactor.

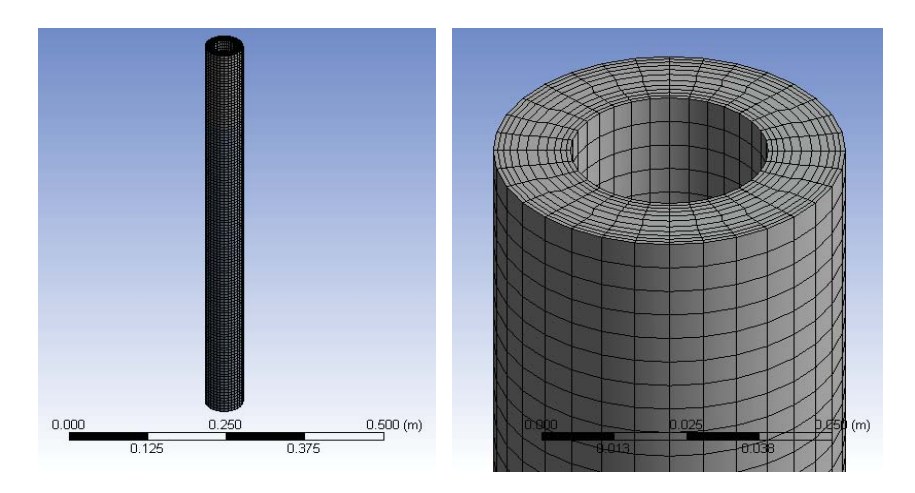


Figure 3.2: Fluidized bed reactor mesh

3.2 Results and discussion

The effect of the grid size, turbulent models, and interfacial forces on the simulated gas holdup, axial liquid velocity, turbulent kinetic energy, and turbulent dissipation rate was investigated. The CFD simulation results were compared to the experimental data reported by Kulkarni et al. (2007). They collected time-averaged radial profiles of flow quantities at different axial locations in a 150 mm diameter bubble column reactor using laser doppler anemometer (LDA).

3.2.1 Grid size

The accuracy of the CFD simulation using different turbulent models and grid sizes was evaluated by the comparison of experimental and simulated radial axial liquid velocity, gas holdup, turbulent kinetic energy, and turbulent dissipation rate profiles at three axial locations. In order to characterize the accuracy of the models at all points of comparison, the normalized root mean square error (RMSE) was used (You et al., 2016):

$$RMSE = \sqrt{\frac{1}{N} \sum_{i=0}^{N} (M_i - E_i)^2}$$
 (3.1)

where N is the number of data points, M_i are the model data points, E_i are the experimental data points. For all the turbulent models, the RMSE (Figure 3.3) shows a general decrease in simulation error with an increase in the grid size from 6837 to 98264 cells. Beyond 98, 264 cells, an increase in the simulation error was observed. Therefore, the optimum grid was taken as 98, 264 cells and used for all further simulations. This optimum has been observed by other researchers. For example, Ekambara et al. (2010) reported that the optimum grid was such that the cell to bubble diameter ratio should be around 1.5. They attributed the inaccuracy of finer grid to the fact that in such cases, bubble size is larger than the average cell size. From the error analysis, the RSM model was the most accurate, followed by the RNG k- ϵ model with the standard k- ϵ model showing the least accuracy. The explanation for this will be discussed in upcoming sections.

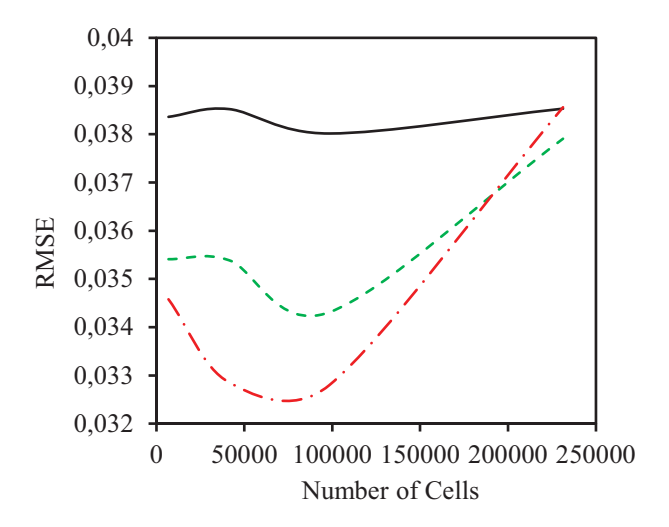


Figure 3.3: RMSE of different turbulent models and cells. (—) Standard k- ϵ , (- - -) RNG k- ϵ and (— · —) RSM models.

3.2.2 Reactor geometry

The tubular reactor geometry was observed to be symmetric along the axial line; therefore, only a section of the reactor could be simulated by specifying appropriate symmetry planes. In this work, three geometries were investigated: full, half, and quarter reactor (Figure 3.4) using the RNG k- ϵ turbulent model. Simulating only a part of the reactor, if accurate, is desirable, as it could markedly reduce the simulation time by reducing the grid size. In order to investigate the effect of geometry on the simulation accuracy, the RMSE methodology of section 3.1 was used. The results (Figure 3.5) show that significant errors were introduced by simulating only a part of the reactor geometry. The full reactor was the most accurate, followed by the quarter reactor with the half reactor exhibiting the least accuracy.

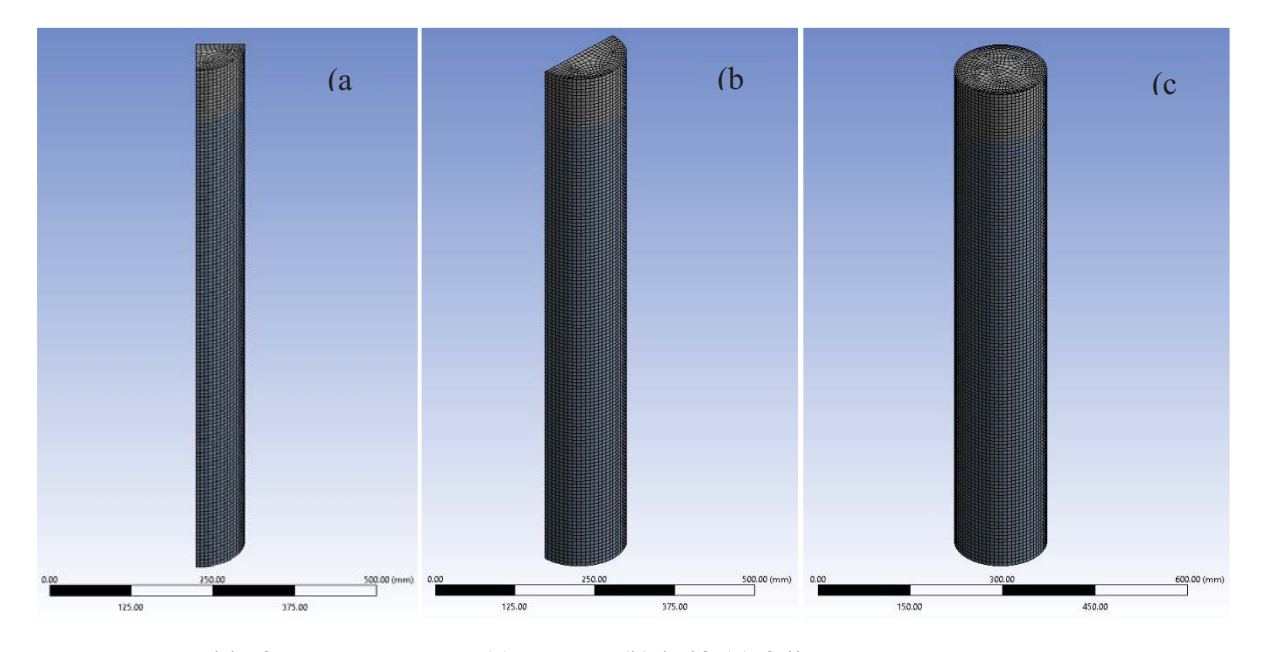


Figure 3.4: Grid of reactor geometry (a) quarter, (b) half, (c) full

A bubble column reactor exhibits a 3D fluctuation of the rising bubble plume under operation, as shown in the instantaneous liquid velocity vectors (Figure 3.6d). This suggests that, although the reactor was geometrically symmetric, it was not hydrodynamically symmetric due to some spatial and temporal variation of the bubble plume. Therefore, simulation accuracy depended on the geometry being able to capture as much of the fluctuating plume as possible. This was the case with the full geometry, in which, the highest gas holdup was located in the middle of the column as shown in the time-averaged gas holdup contours (Figure 3.6e-g). This was not the case with the half geometry, in which the high gas holdup region was restricted to a region between the wall and the centre of the reactor (Figure 3.6c-d). Moreover, an increase in the averaging time from 30 s to 240 s pushed the high gas holdup region further away from the middle of the column.

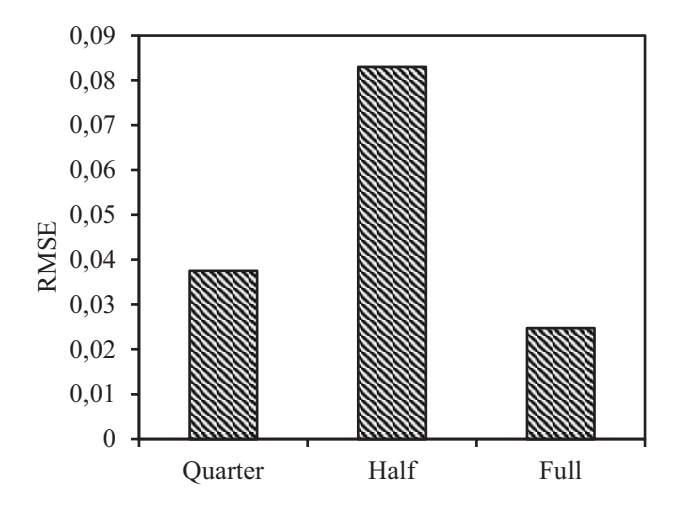


Figure 3.5: Effect of reactor geometry on simulation accuracy (RMSE)

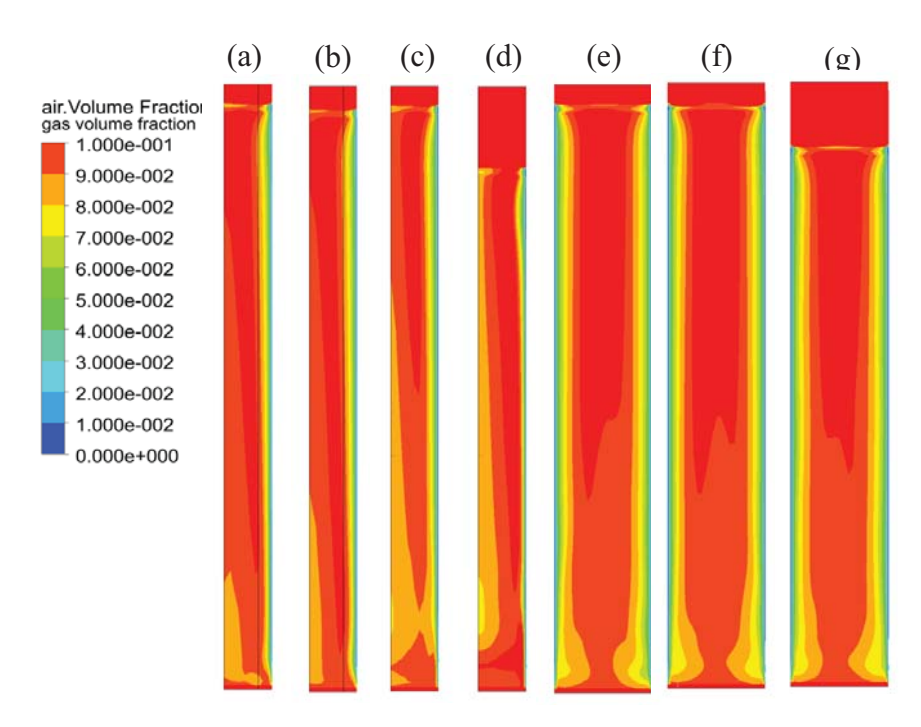


Figure 3.6: Effect of reactor geometry on the time-averaged gas holdup contours (a) quarter 30 s, (b) quarter 240 s, (c) half 30 s, (d) half 240 s, (e) full 30 s, (f) full 60 s, (g) full 120 s

An improvement was observed in the quarter geometry in which the high gas holdup region shifted towards the middle of the column (Figure 3.6a-b). However, the region of maximum gas holdup was located higher up the column than in the full geometry, an effect which increased with an increase in averaging time from 30 s to 240 s. Since the quarter and half reactor geometry were not able to accurately capture the flow characteristics, all further simulations were carried out using the full geometry. The findings of simulation focusing on the effects of turbulence models and interfacial forces are discussed in detail in Appendix D.

3.2.3 Fluidized bed reactor

The CFD model for simulating the fluidized bed reactor was validated using the bubble column of Kulkarni et al. (2007) in order to determine the best turbulent model and interfacial forces. The bubble column was chosen for validation of the CFD model instead of a three phase fluidized bed reactor for several reasons. First, most of the three phase fluidized bed reactors for which experimental data was available, utilized very large particles at high solid loading. For example, Panneerselvam et al. (2009) simulated fluidized bed reactors with a typical solid particle size of 3 mm and a solid volume fraction of 0.6. In contrast, the fluidized bed reactor used in this work had a particle size of 900 nm at a solid volume fraction of 4.7×10^{-5} corresponding to a catalyst loading of 0.2 g/L. Also, in such reactors, both the gas and liquid flow in and out of the reactor (Schallenberg et al., 2005; Panneerselvam et al., 2009). However,

in the fluidized bed reactor used in this work, both the liquid and solid were retained within the reactor.

In view of the factors discussed, the reactor in this work was much similar hydrodynamically to a bubble column than previously simulated three phase fluidized bed reactors. Boyjoo et al. (2013) also noted this similarity between a bubble column reactor and a fluidized bed reactor with nanoparticles. This fact has also been recognized by Feng et al. (2005), who simulated their gas-liquid-nanoparticle reactor essentially as a bubble column with the liquid properties modified in order to account for the nanoparticles. This work improved upon the work of Feng et al. (2005) by adapting the bubble column CFD model to three phase simulation by adding the catalyst as a separate solid phase.

The simulation conditions in the bubble column reactor, which gave the best results, were found to be the Reynolds Stress Model and the use of a combination of drag, lift, wall lubrication and turbulent dispersion forces. These simulation conditions were applied when carrying out the CFD simulation of the annular fluidized bed reactor. In an annular reactor, all the fluid is confined within the annulus between the inner and outer reactor wall. The axial liquid velocity plot along the radial coordinate (Figure 3.7) shows the liquid flowing upwards in the middle of the annulus and downwards towards both walls of the annulus. This flow reversal profile within the annulus is commonly observed in tubular reactors.

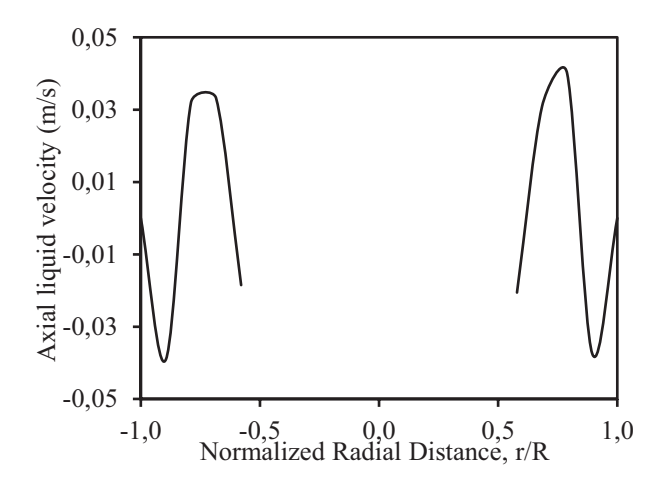


Figure 3.7: Radial axial liquid velocity profile

The radial gas holdup profile (Figure 3.8) shows that the highest gas holdup is in the middle of the annulus and dropping to zero at both walls of the reactor. This is further clarified by the axial and radial gas holdup contours (Figure 3.9a,c), which shows a high gas holdup in the

middle of the annulus. Vincent et al. (2011) reported a similar gas holdup profile in their annular reactor. This profile is due to the tendency of bubbles to move away from walls. In this case, the bubbles moved away from both walls and towards the centre of the annulus. The opposite trend was true for the solid holdup profile in which the highest solid holdup was observed at the reactor walls with the solid holdup reducing towards the middle of the reactor (Figure 3.8; Figure 3.9b,d). This was attributed to the fact that the reactor had only two dispersed phases and they could not occupy the same space. Therefore, the gas occupying the centre of the annulus pushed the solids towards the wall. From a photocatalysis perspective, this is desirable since a higher solid catalyst loading at the walls would expose more catalyst to the light from sunlight and UV lamp.

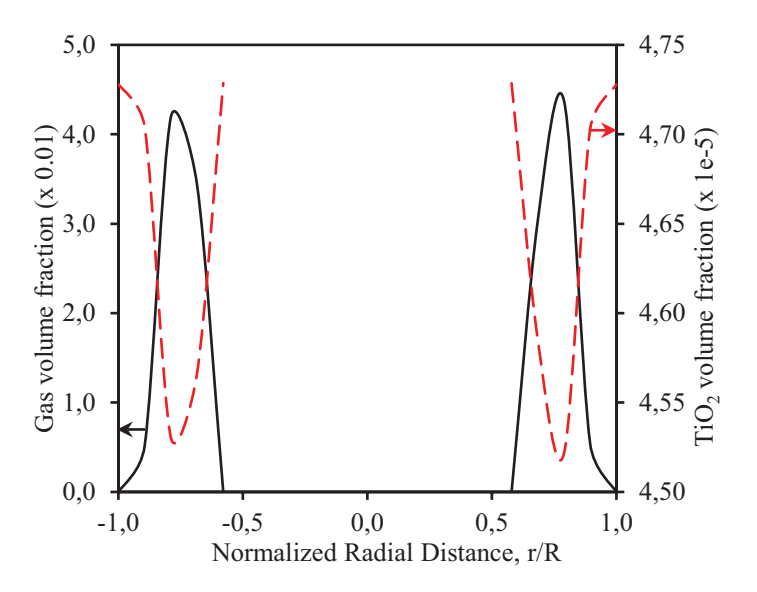


Figure 3.8: Radial gas and solid holdup profiles

Generally, the radial variation of the catalyst loading was not significant. For instance, in the radial section represented by Figure 3.8, the difference between the highest and lowest solid holdup was only 4%. The axial variation of the solid holdup along the column was also observed to be insignificant (Figure 3.9b). The insignificant variation of the solid holdup in the reactor was because the catalyst was nanoparticulate in nature and could be easily fluidized in the reactor. Consequently, an assumption of uniform catalyst distribution in the reactor can be made. The simulation of the photocatalytic reactor involves the modelling of the hydrodynamics, light distribution, and reaction. In such a simulation, the most important information to be obtained from hydrodynamics is the catalyst distribution. Therefore, an assumption of uniform catalyst distribution means that detailed hydrodynamics modelling can

be neglected. This can significantly simplify photocatalytic reactor simulation with huge time savings since hydrodynamics simulation is usually time consuming.

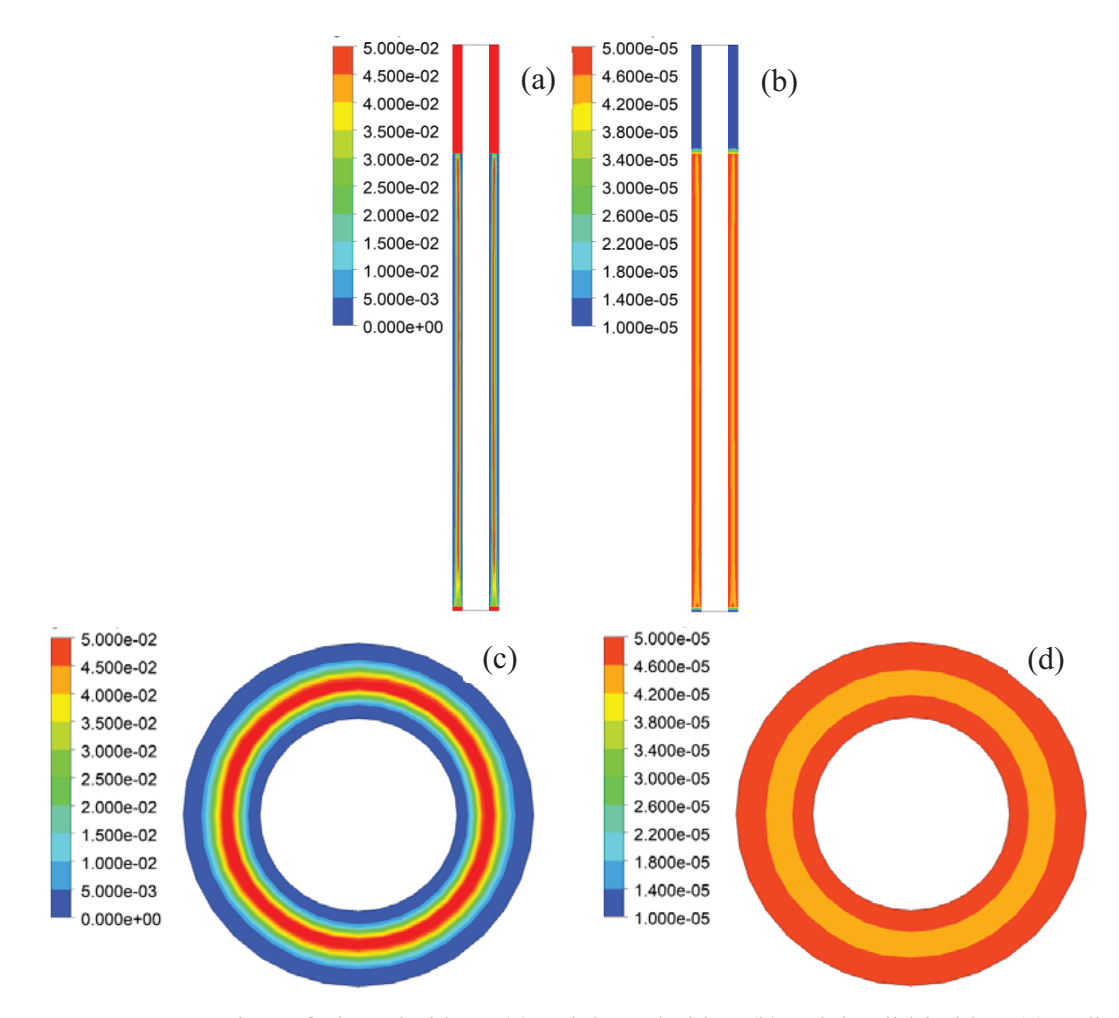


Figure 3.9: Contour plots of phase holdups (a) axial gas holdup (b) axial solid holdup (c) radial gas holdup (d) radial solid holdup

CHAPTER 4: INTEGRATED ANAEROBIC DIGESTION AND OZONOLYSIS TREATMENT OF DWW

4 Introduction.

Distillery wastewater (DWW), is characterized by a very high organic load (chemical oxygen demand, COD, 92-100 g/L, five-day biochemical oxygen demand, BOD₅, 52-58 g/L) and a dark colour (Ghosh Ray and Ghangrekar, 2018). The colour is caused by heterogeneous, nitrogen-containing biorecalcitrant brown pigments formed during the non-enzymatic reaction (Maillard) involving amino acids and carbohydrates (Satyawali and Balakrishnan, 2008). The biorecalcitrant nature of the melanoidin pigment is shown by the fact that it escapes from the usually applied conventional anaerobic wastewater treatment and finally ends up in the environment in the form of a coloured effluent. If the effluent is discharged into aquatic systems such as rivers, lakes or dams without further treatment, the colour can block light and prevent photosynthesis by aquatic plants leading to the eutrophication of the receiving streams (Navgire et al., 2012).

For effective removal of the colour and the organic load, integrating the anaerobic process with a post-treatment technique is necessary. Ozonation, an advanced oxidation process (AOP), is a highly competitive treatment technique that can be easily applied to remove the biorecalcitrant colour (Takashina et al., 2018). In this chapter, integrated anaerobic digestion and ozonolysis treatment of DWW has been carried out. The AD was carried to reduce organic load followed by ozonolysis posttreatment to remove the biorecalcitrant colour. For design and integration purposes, the kinetic study of the individual processes was carried out.

4.1 Materials and methods

4.1.1 Materials

Sodium thiosulphate, potassium iodide (KI), sulphuric acid, hydrochloric acid, silver sulfate, potassium dichromate, and sodium hydroxide were all purchased from Merck Ltd, South Africa. The chemicals, which were of analytical grade, were used as received. Standard and working solutions were prepared using ultra-pure distilled water. Real vinasse was obtained from an alcohol distillation plant in Durban, South Africa, diluted to a desired initial concentration and then subjected to anaerobic digestion followed by ozonation. The physical and chemical characteristics of the vinasse are given in Table 4.1.

Table 4.1: Characteristics of the vinasse before treatment

| Parameter | Units | Value |
|-----------------------|-------|--------|
| pН | | 4.59 |
| COD | g/L | 120.00 |
| TOC | g/L | 46.40 |
| TSS | mg/L | 16.34 |
| BOD ₅ | g/L | 57.6 |
| BOD ₅ :COD | | 0.48 |
| Colour/absorbance | a.u. | 12.22 |

Key; TOC – Total organic carbon, TSS – Total suspended solids

4.1.2 Anaerobic digestion and ozonation processes

Anaerobic digestion was carried out in an up-flow anaerobic sludge blanket (UASB) digester (Figure 4.1a). The 3.5 L digester was made of an acrylic glass column with a working volume consisting of 1 L sludge bed and 2 L substrate solution. The digester was inoculated with 1 L of anaerobic sludge granules sourced from a local full-scale UASB digester treating vinasse, then 2 L of distilled water added for stabilization for 24 hours. At the beginning of the batch start-up after stabilization, an aliquot of the supernatant was withdrawn and a similar volume of vinasse dosed. For instance, on day 1 of start-up, the reactor was fed with 15 ml of the vinasse representing an OLR of 0.0867 kg COD/d/m³. The daily OLR was increased gradually while monitoring the pH, biogas production, and volatile fatty acids (VFA)/Alkalinity (Alk) ratio. After 33 days, the reactor was stable at best organic loading rate of 15 kg CODm⁻³d⁻¹ as was determined by a stable pH of about 7.5 and desired VFA/Alk ratio of 0.4. The digester was thereafter operated semi-continuously at the OLR of 15 kg CODm⁻³d⁻¹; the treated effluent was subjected to ozonation.

Ozonation post treatment of the anaerobically digested effluent was carried out in an ozone reactor of 4 L capacity at different ozone dosages. Ozone gas was generated from the air using an ozone generator coupled to an air compressor then bubbled in an up-flow mode via a gas diffuser (Figure 4.1b). To obtain different ozone dosages, the airflow rate to the generator was controlled using a manual valve, and the flow measured using an air rotameter. For instance, an airflow rate of 2 L/min generated an air-ozone mixture with a dosage of 45 mg O₃ per minute supplied to the reactor. The unutilized ozone gas from the reactor was passed through an ozone

trap containing potassium iodide (KI) solution for destruction. Samples were withdrawn at a pre-determined time interval and analyzed.

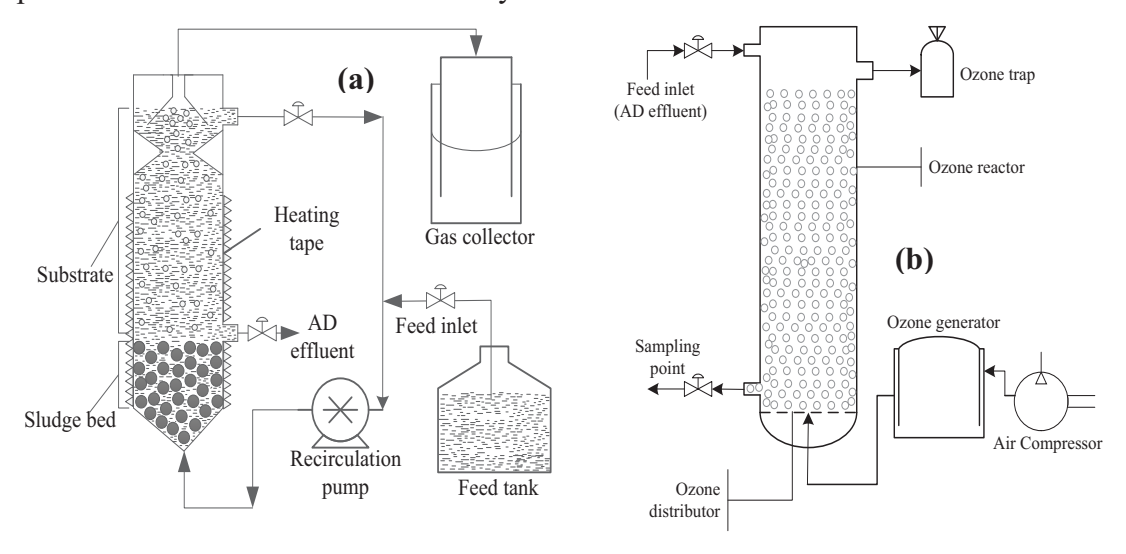


Figure 4.1: Schematic representation of the (a) anaerobic and (b) ozonation units.

4.1.3 Chemical analyses

The COD and five days BOD were determined according to standard methods (APHA-AWWA-WEF, 2005). A well-mixed sample was filtered through a weighed filter paper and the residue dried to constant weight at 105° C to determine total suspended solids (TSS). The TSS was given by the increased weight of the filter paper. To analyze color, the absorbance of samples was measured using a UV-Vis spectrophotometer (T80+ UV/VIS Spectrometer, PG Instruments Ltd) at a maximum absorption wavelength (λ_{max}) of 475 nm (Navgire et al., 2012). The total VFAs and alkalinity were determined by a simple, low cost and fast titration method, which involved titration of samples with HCl and back titration with NaOH (Yang and Anderson, 1992). Total organic carbon (TOC) was determined using a TOC analyzer (TELEDYNE Tekmar). The composition of the produced biogas was analyzed using a gas chromatograph (GC Trace 1310).

4.1.4 Ozone transfer

The ozone transfer was determined by;

$$O_3 T = \frac{o_3 s}{o_3 u} X 100 \tag{4.1}$$

where, O_3T , O_3S and O_3U are the ozone transfer (%), supplied, and utilized ozone (mg), respectively.

4.2 Results and discussion on anaerobic digestion of DWW

4.2.1 Bioreactor start-up

In the start-up period that lasted 33 days, the performance of the reactor was monitored by measuring the pH, daily biogas production, and VFA/Alk ratio, as shown in Figure 2. The low OLR during the initial period resulted in low biogas production (0.35 L/day). As the OLR was increased, the daily amount of biogas increased gradually from 0.95 to 3.22 L/day and finally to 5.9 L/day after which a gradual decline was observed from day 31 (Figure 4.2a). The declined gas production could have resulted from overloading of the reactor, which hindered the activity of the microorganisms, as shown by a sharp increase in the VFA/Alk ratio (Figure 4.2b). The VFA/alkalinity ratio increased steadily from 0.02 to 0.6 with the recommended 0.4 exceeded from day 31 indicating reactor instability resulting from possible overloading (Lopez-Lopez et al., 2015). The maximum biogas production was thus achieved on day 31 when the OLR was 15 kg CODm⁻³d⁻¹. The pH (Figure 4.2b) remained relatively stable with a slight gradual increase from 7.0 to 7.8 in the entire course of start-up indicating a healthy environment for the microorganisms. Whereas the pH can be a good indicator of reactor stability, in a highly buffered system as was the case during the start-up (as shown by the stable pH), more indicators such as VFA/Alk ratio should be used for accurate reactor assessment (Hampannavar and Shivayogimath, 2010).

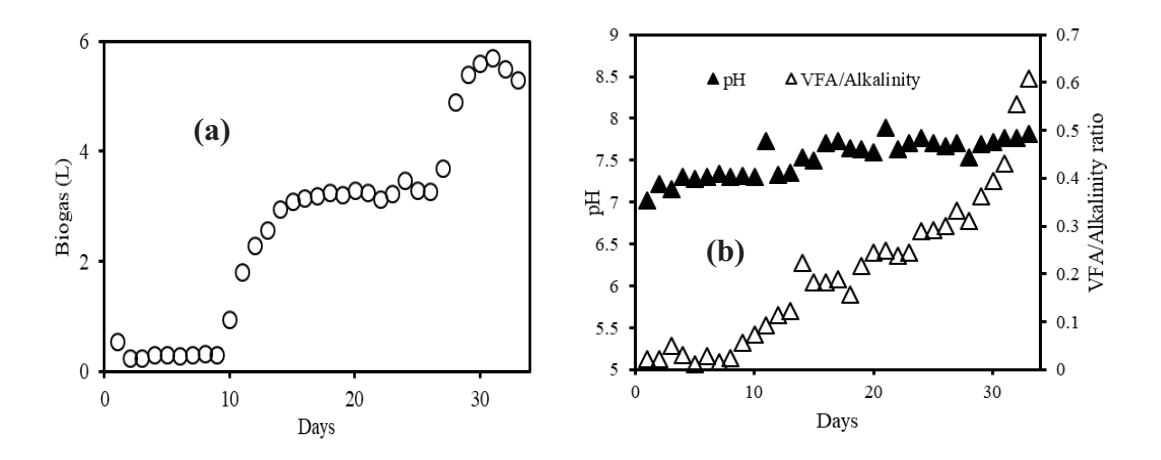


Figure 4.2: (a) Daily biogas production and (b) pH (\blacktriangle) and VFA/Alkalinity (Δ) ratio during anaerobic digester startup.

4.2.2 Organic load and colour reductions during anaerobic digestion

The COD, colour and BOD reductions were monitored at the best OLR of 15 kg CODm⁻³d⁻¹. From Figure 4.3a, the COD removal increased from 32% on day 34 to 57% on day 35 and 63%

on day 37. The low reduction of COD at the beginning of the semi-continuous operation was partly due to residual organics accumulated during the start-up that still existed in the reactor and acclimatization of the microorganisms with the new feeding method (transiting from batch to a semi-continuous feeding). The highest COD removal of around 75% on day 41 was attained after all the residuals had been removed. For the remaining days, the COD removal averaged at around 75%. The anaerobic process was also monitored by changes in BOD₅ and BOD₅:COD ratio, as shown in Figure 4.3b. An average final BOD₅ of 550 mg/L representing a reduction of up to 92%.

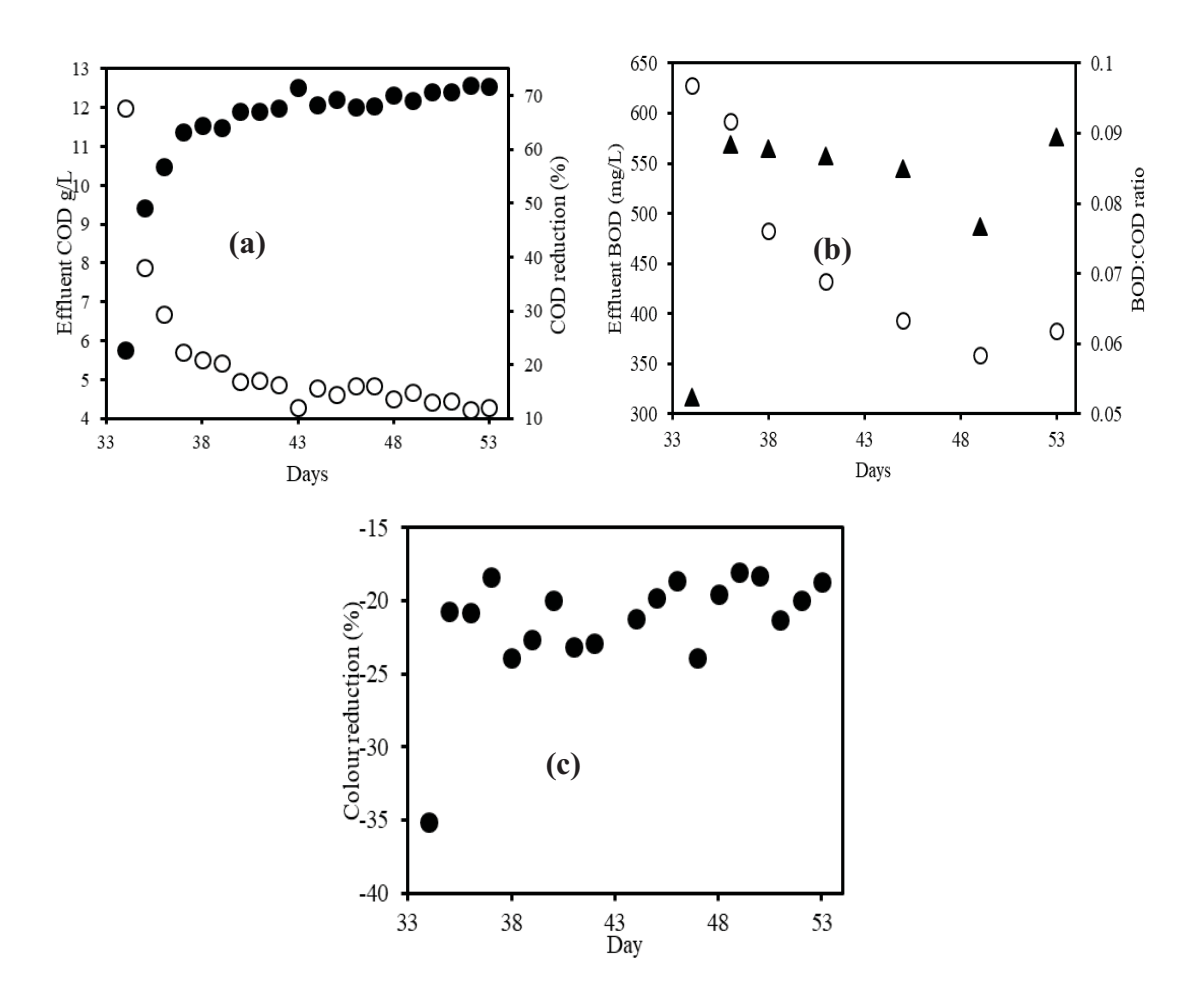


Figure 4.3: (a) Effluent COD (\circ) and COD reduction (\bullet) , (b) effluent BOD (\triangle) and BOD:COD ratio (\circ) , and (c) colour reduction during the semi-continuous operation of the UASB digester

The BOD₅:COD ratio of the AD treated effluent averaged at around 0.09 from an initial value of 0.48 (before AD), signifying the near complete removal of the biodegradable constituents of the vinasse. Given that up to 92% of the BOD was removed, the remaining organic matter contributing to the average residual COD of 4 g/L COD was, therefore, attributed to the biorecalcitrant colour causing pigments such as melanoidins as evidenced by a poor colour

reduction in the AD step (Figure 4.3c). The negative colour reduction observed implied an increase in colour intensity in the AD process. During AD, the melanoidin compounds repolymerizes into high molecular weight long chain organic compounds with increased colour intensity (Liu et al., 2013). To remove the biorecalcitrant colour, the AD effluent was subjected to ozonation treatment.

4.2.3 Kinetic parameters of anaerobic digestion

The Monod and Contois models were used determine the kinetic parameters of anaerobic digestion. The values of biomass death rate (K_d) , yield coefficient (Y), specific growth rate at saturation (μ_{max}) and kinetic parameter (B) were determined from the linear derivatives of the models as developed in Appendix F. An average of five sets of data from the steady-state were used to obtain the parameters for applying the kinetic models (Figure 4.4).

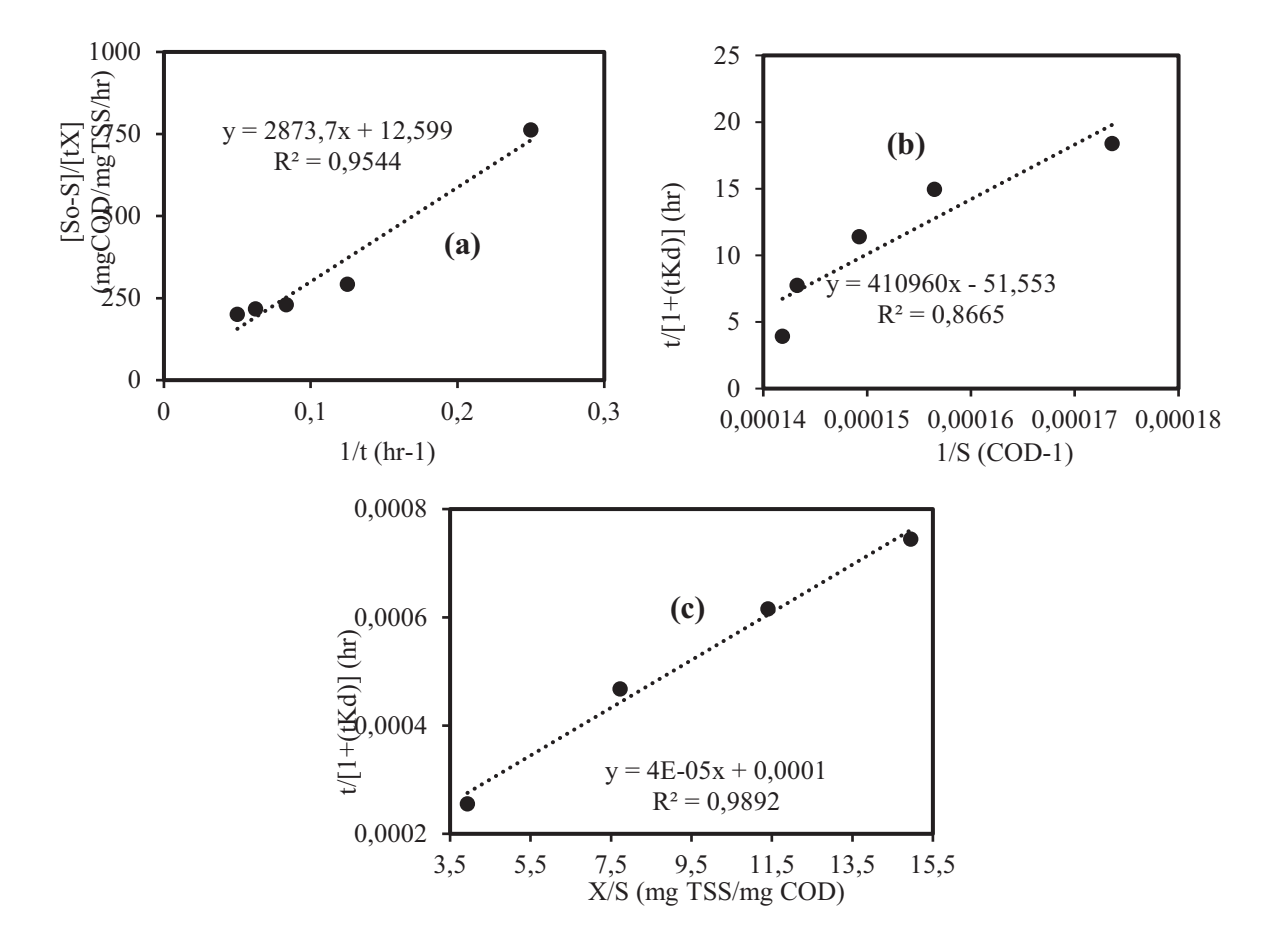


Figure 4.4: Determination of (a) growth and decay rates, (b) maximum specific growth rate based on Monod model, and (c) half saturation constant based on Contois model.

The plot given in Figure 4.4a was used for determining Y and K_d , while μ_{max} and K_s based on the Monod model were determined from Figure 4.4b. The μ_{max} and B based on the Contois model were obtained from Figure 4.4c, from the intercept and slope, respectively. The biomass yield coefficient (Y) obtained was 0.0004 g/gCOD with a K_d value of 0.005 hr⁻¹. From the R² values, the anaerobic process was less described by the Contois model (R²=0.08665) as compared to the Monod model (R²=0.9892). The Monod model adequately predicts anaerobic digestion of simple substrates. However, for heterogeneous complex substrates such as the DWW which contains several biorecalcitrant compounds, the Contois model has been found suitable (Kythreotou et al., 2014). The biomass yield of 0.0004 g/g COD calls for a posttreatment method capable of sludge reduction prior to effluent disposal to receiving streams.

4.3 Results and discussion ozonolysis post-treatment of anaerobically digested DWW

4.3.1 Characteristics of the distillery wastewater before and after AD

The DWW before AD had a high organic load (COD 15 000 mg/L, BOD₅ 7200 mg/L), and BOD₅:COD ratio of 0.48, Table 4.2. The ratio indicated favorable biodegradability. Upon biodegradation, up to 75% of the COD and 95% of BOD₅ were removed but with an increased color intensity of 40%. A considerable amount of COD of 4000 mg/L remained after AD, indicating the presence of biorecalcitrant melanoidin compounds responsible for the intense color of the AD effluent. The biorecalcitrant part was confirmed by the BOD₅:COD ratio of 0.05 indicating non-biodegradability of the AD effluent since all the biodegradable organics had been removed in the AD step. Also observed was a two-fold increase in total suspended solids (TSS) after AD indicating sludge washout from the AD reactor. The anaerobically digested DWW effluent obtained was subjected to ozonolysis post-treatment to remove the color and solubilize the solids.

Table 4.2: Characteristics of the distillery wastewater before and after anaerobic digestion

| Parameter | Units | Before AD | After AD | Change, % |
|-----------------------|-------|-----------|----------|-----------|
| pН | | 4.59 | 7.45 | +62 |
| COD | mg/L | 15000 | 4000 | -75 |
| TOC | mg/L | 5800 | 1700 | -72 |
| TSS | mg/L | 2.34 | 4.46 | +110 |
| BOD ₅ | mg/L | 7200 | 190 | -95 |
| BOD ₅ :COD | | 0.48 | 0.05 | -90 |
| Colour/absorbance | a.u. | 3.20 | 4.50 | +41 |

Key; TOC - Total organic carbon

4.3.2 Effect of initial concentration

The effect of dilution on decolorization, TOC reduction, and ozone transfer during ozonolysis of the DWW is given in Figure 4.5. The colour reduction efficiency increased from 29% to 90% with an increase in dilution from ×1 to ×8, as shown in Figure 4.5a. The lowest color removal of the undiluted (×1) DWW signifies the importance of diluting the color intense DWW before ozonolysis. The color reduction is attributable to the oxidation of the color causing biorecalcitrant brown polymeric melanoidin pigments, which have been reported to constitute 2% of cane molasses (Chavan et al., 2006). Similarly, the TOC reduction increased with decreasing initial concentration, Figure 4.5b. However, even at the highest dilution factor of ×8, only a paltry 16% of TOC was removed. The undiluted DWW had no significant TOC reduction. The ozonolysis process is thus effective in decolorizing the DWW but with minimal mineralization of TOC.

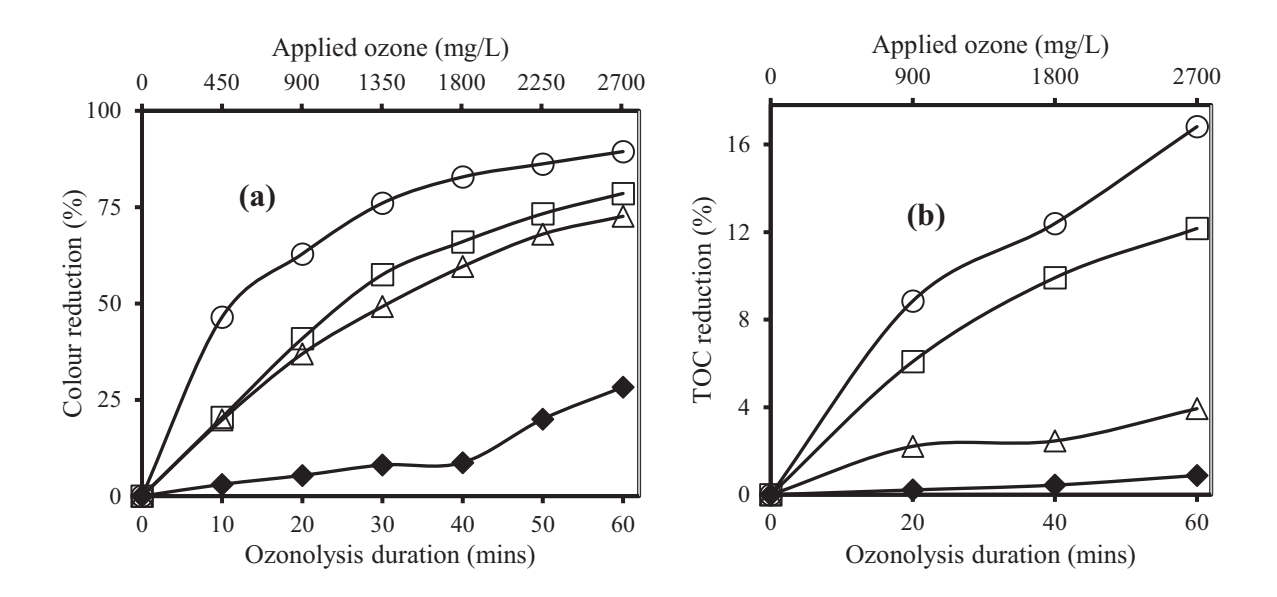


Figure 4.5: Effect of dilution on (a) color and (b) TOC reductions at different dilutions of $\times 1$ (\spadesuit), $\times 2$ (\triangle), $\times 4$ (\square) and $\times 8$ (\circ)

4.3.3 Energy utilization and ozone transfer at different initial concentrations

In Figure 4.6a, the ozone transfer reduced with reducing initial concentration (increasing dilution) with the ×1 and ×2 dilutions achieving transfer efficiencies above 95%. At high initial concentration, there are more organic compounds to be readily attacked by the supplied ozone molecules and hence the high ozone transfer observed. The determination of the optimum dilution factor (DF) was also evaluated based on energy consumed to remove 75% of the effluent colour for the different dilutions. The electrical energy consumption of the ozone

reactor taking into consideration dilution was analyzed using a modified electrical energy per order (E_{OZ}) equation by Shu et al. (2013);

$$E_{OZ} = \frac{Pt}{V\log(\frac{C_{i}}{C_{f}})} \times DF$$
 (4.2)

where P is the ozone reactor power (kW), t is the ozonolysis duration (hours), V is the volume (m^3) of DWW treated, C_i and C_f are the initial and final concentrations of the target contaminant. The DF of $\times 2$ was found to be the optimum based on its least energy consumption of 2 kWh/M³, as shown in Figure 4.6b. The $\times 8$ dilution despite achieving the 75% colour removal within the shortest duration of 30 minutes, still consumed the highest amount of energy due to the high dilution factor. The ozone transfer efficiency which is closely related to the O_3 mass transfer and the energy consumption, justified the selection of the $\times 2$ dilution (Zhen et al., 2017).

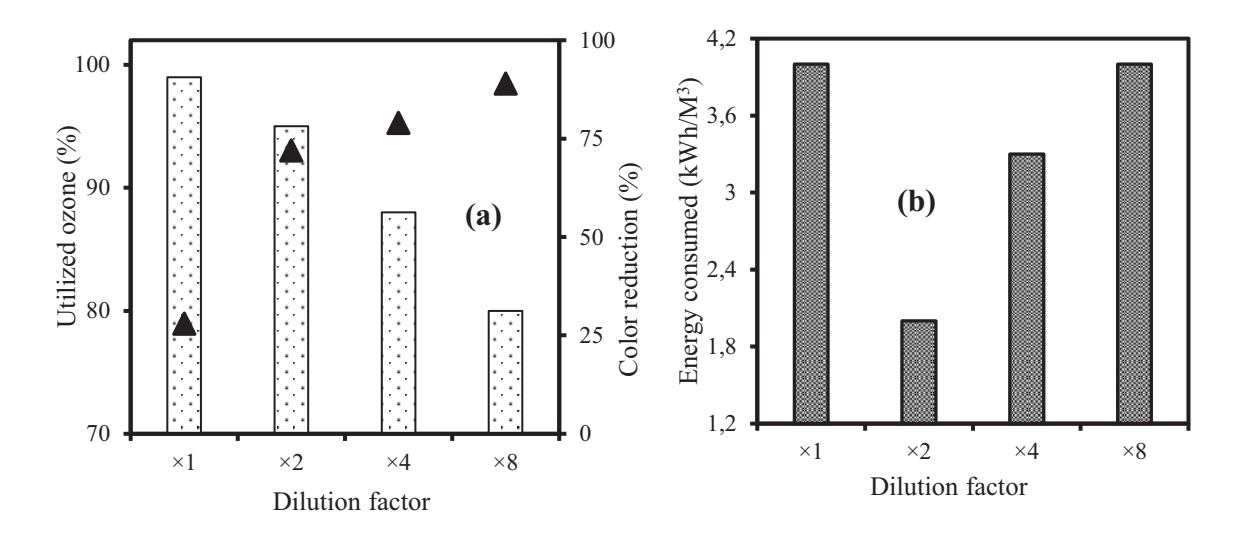


Figure 4.6: Comparison of; (a) ozone transfer (a) and color reduction (\triangle), and (b) energy consumed to remove 75% of the colour, at different dilutions

4.3.4 Effect of ozone dosage

Selecting an appropriate ozone dosage is very important in optimizing the ozonolysis process by maximizing the ozone transfer. The effect of ozone dosage (achieved at varying ozone flowrates) on decolorization, ozone transfer, and TOC reduction is given in Figure 4.7. The highest color removal of 80% was achieved at a flow rate of 45 mg O₃/L/min, while the lowest flow rate of 22.5 mg O₃/L/min removed 60% of the color after 60 minutes, Figure 4.7a. The higher flow rates of 67.5 and 90 mg O₃/L/min had color removals of 70 and 66%, respectively. As the flow rate increased from 22.5 to 45 mg O₃/L/min, the number of ozone molecules

attacking the organic aromatics increased as well, leading to increased color removal. In Figure 4.7b, it was observed that the change in ozone dosage did not have any significant effect on the TOC reduction as compared to color removal. At the optimum dosage of 45 mg $O_3/L/min$, 18% of TOC reduction was achieved as compared to the 80% of color removed. This could be attributed to the low oxidation of TOC by ozone as compared to the reduction of color-causing compounds.

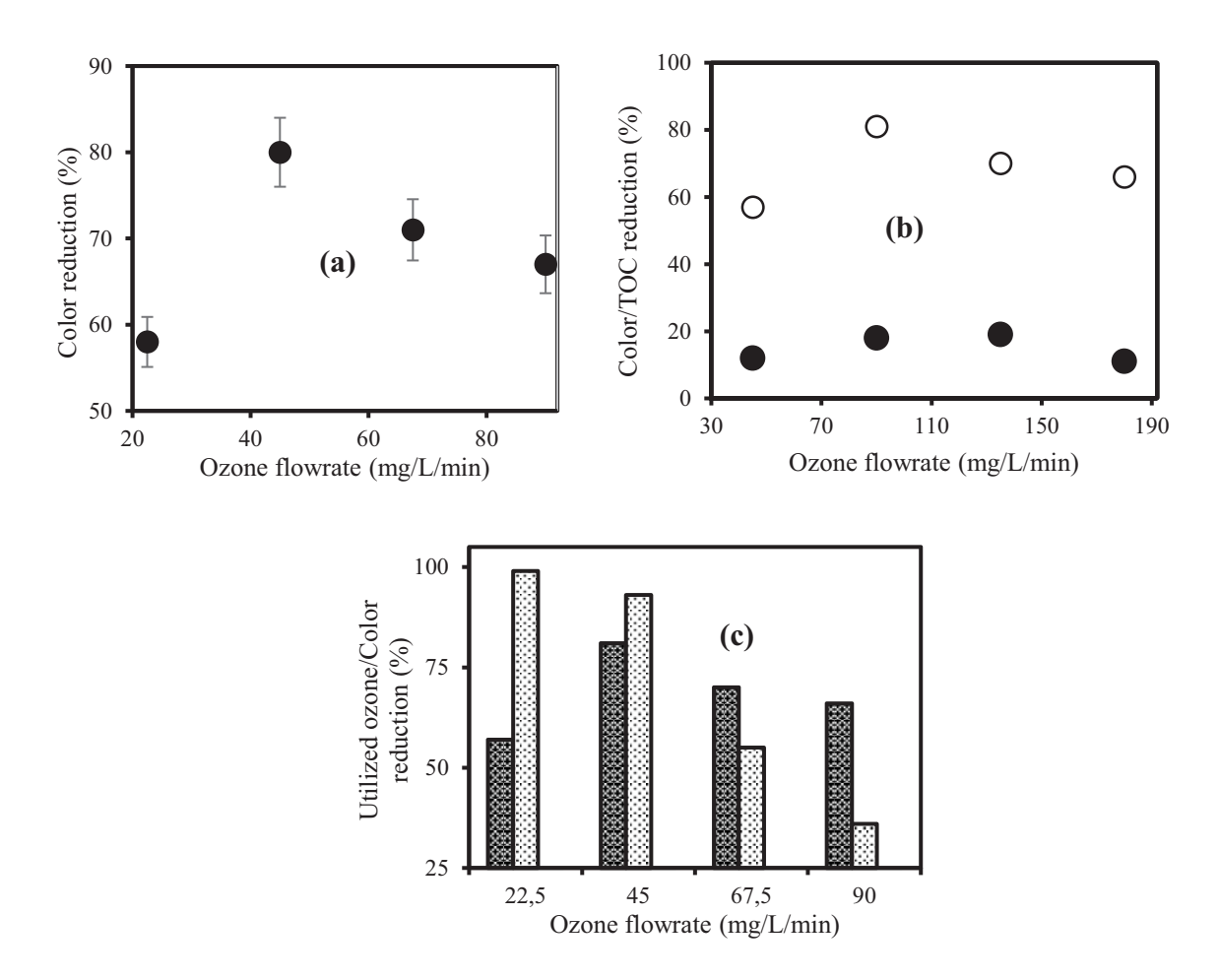


Figure 4.7; (a) Effect of ozone flowrate on color reduction and, comparison of (b) TOC (•) vs. color (○) reduction and (c) ozone transfer (◎) vs. color reduction (■) at the different ozone flowrates after 60 minutes of ozonolysis.

Increased flowrate increases the ozone dosage, which increases the surface area for ozone mass transfer to the substrate thus accelerating the ozonolysis process (Mecha et al., 2016). At higher flow rates, however, the supplied gas forms big bubbles in the reactor column thus minimizing the contact between the O₃ molecules and the organic compounds and hence significantly reducing the mass transfer of O₃. This ultimately allows most of the ozone to escape in the offgas. The low ozone transfer at high flowrates is not economical.

4.3.5 Effect of initial pH

The effect of pH on the ozonolysis process is given in Figure 4.8. At an acidic pH of 4, the highest color removal of 80% was obtained as compared to 67% removal at the pHs of 7 and 10 (Figure 4.8a). In contrast, for the reduction in TOC (Figure 4.8b), the highest reduction of 16% was achieved at the alkaline pH of 10, while the lowest reduction of 5% was at pH 7. The reductions in color and TOC are attributable to oxidation of the color causing melanoidin compounds and degradation of organic compounds. The ozonolysis process is highly affected by the pH of the substrate. Under acidic conditions, ozone selectively attacks parts of the colour causing organic compounds containing C=C double bonds, aromatic rings, functional groups such as OH and OCH₃, negatively charged atoms such as N, P, O, S (Bar Oz et al., 2018). The selective attack leads to a rapid color disappearance but with the formation of stable intermediates and end products such as carboxylic acids, which are still detected as TOC hence the low reduction in TOC of 13%. Also, the intermediates and products are refractory to further ozone oxidation (Peña et al., 2003).

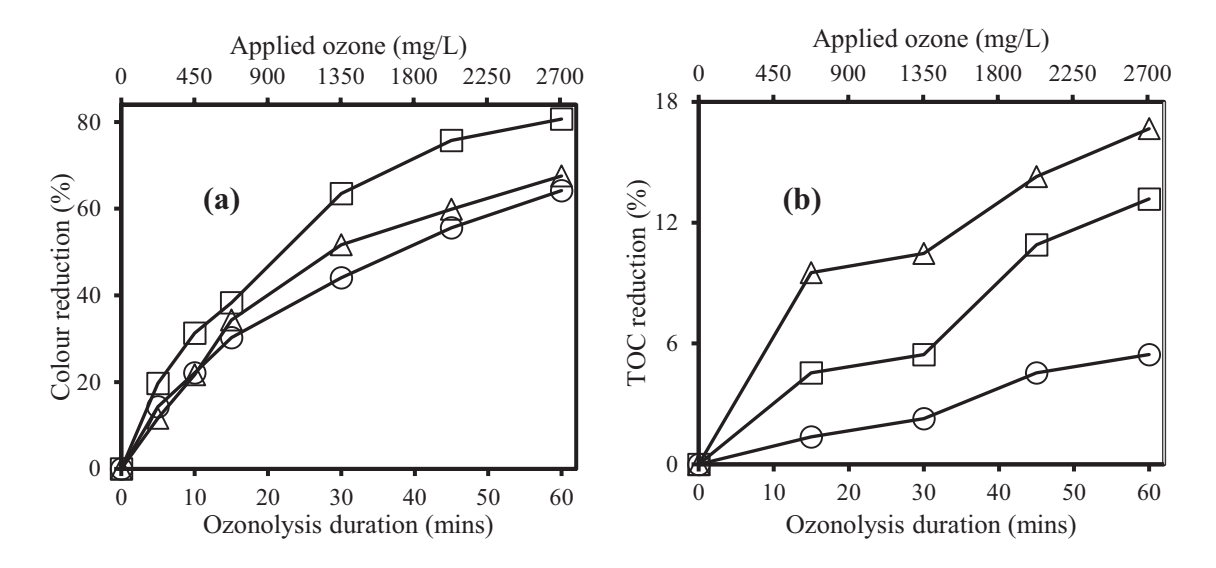


Figure 4.8: Effect of pH 4 (\square), 7 (\circ), and 10 (Δ) on (a) colour and (b) TOC reductions during ozonolysis of DWW anaerobic effluent.

4.4 Results and discussion on the kinetics of integrated AD and ozonolysis of DWW

In an integrated AD-AOP where ozonolysis is applied as posttreatment after the anaerobic digestion of DWW, the kinetics study of the two processes is necessary for reactor design purposes. The AD process is aimed at the reduction of high organic load (COD) followed by decolourisation of the effluent through ozonolysis. The kinetics of AD was determined from

the first order substrate removal model at steady-state (-dS/dt) as (Ibrahim, 2014; Ebrahimi et al., 2018);

$$\frac{S_o - S}{t} = k_1 S \tag{4.3}$$

where, t, S_o , S and k_1 are the retention time (hrs), initial substrate concentration, substrate concentration at time t, and reaction rate constant, respectively. The substrate removal rate was determined by a plot of $S_o - S$ against t (Figure 4.9a) as 0.83 g COD/h. Based on the rate, it was further determined that a HRT of 15 hours would be required to reduce the COD of the DWW by 75% in the AD unit before subjecting it to ozonolysis.

A pseudo-first order reaction model (Eqn. 4.4) was used to determine the rate of ozonolysis decolourization of the anaerobically digested distillery wastewater.

$$-\frac{dA}{dt} = k^1 A \tag{4.4}$$

where t is the duration of ozonolysis (mins) and k^1 is the reaction rate constant (min⁻¹). Integrating equation (4.4) yields;

$$ln\frac{A}{Aa} = -k^1t \tag{4.5}$$

The pH of 4 with the highest colour reduction had the highest rate constant of 0.0326 min⁻¹, as shown in Figure 4.9b. From the rate constant, a colour removal of < 75% would require ozonolysis duration of 15 minutes.

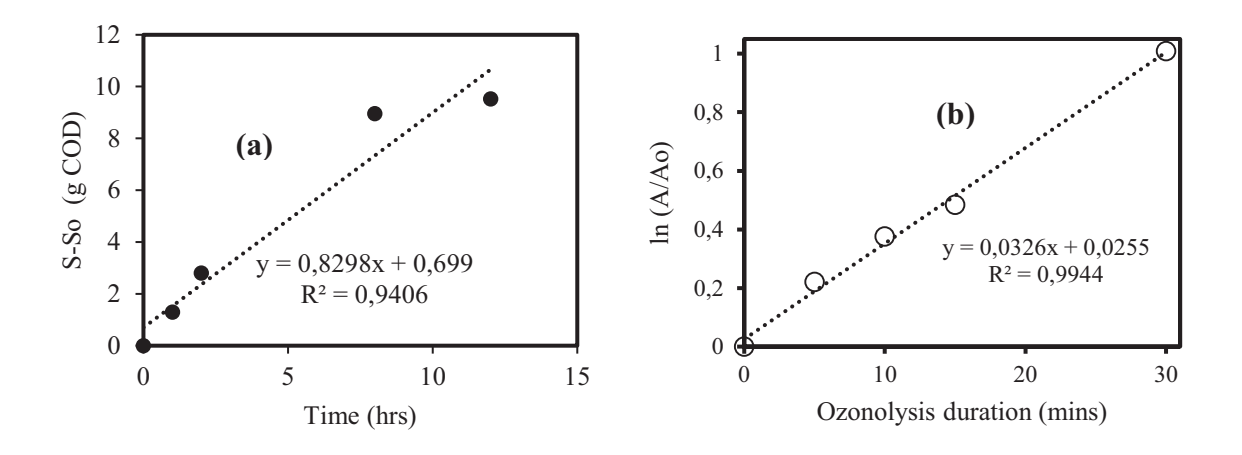


Figure 4.9; (a) Determination of first-order reaction kinetics of AD and (b) colour removal kinetics of Ozonolysis post-treatment of the AD effluent at pH 4.

The rates of both the preceding AD step and that of the ensuing ozonolysis post-treatment show that the time required for AD treatment of DWW is 20 times that required for ozonolysis

decolourization post-treatment when an optimum OLR of 15 kg COD/m³.d is applied. Therefore, for effective integration of the two processes, the ozone reactor should be 20 times smaller than that of the AD for a complete continuous process. Alternatively, a reservoir can be installed to contain the anaerobically digested effluent prior to ozonolysis for easy flow regulation.

CHAPTER 5: ENERGY, COST AND ENVİRONMENTAL ANALYSİS OF INTERGRATED AD-OZONOLYSIS TREATMENT FOR DWW

5 Introduction

The AOPs are usually high cost, but their application alongside the anaerobic digestion can significantly reduce the overall cost of operation (Oller et al., 2011; Brooms et al., 2018). When integrating AD with AOPs, the overall aim should be to reduce costs by minimizing AOP treatment and maximizing the AD stage. The bioenergy produced from the anaerobic process can be used to provide or supplement the energy requirement of the ozonation and anaerobic processes as depicted in Figure 5.1, and offset the energy demand from the national grid. Appropriately using the biogas to generate energy may reduce GHC emissions by avoiding the release of the biogenic CH₄ with a polluting potential 22 times higher than CO₂ (Moraes et al., 2014). Moreover, there is a possibility of selling certificates of avoided greenhouse gasses emissions (carbon credits) by utilizing the biogas instead of fossil fuels. Distillery wastewater (DWW) has a high biomethane potential of 0.4 L CH₄/g COD with an energy potential of about 15.2 kJ/g COD (Salomon et al., 2011; Apollo et al., 2016; Apollo and Aoyi, 2016). The biomethane energy can be utilised in different ways, including: (i) as alternative vehicular fuel, (ii) cogeneration of heat and electricity, and (iii) electricity generation in internal combustion engines (Moraes et al., 2014).

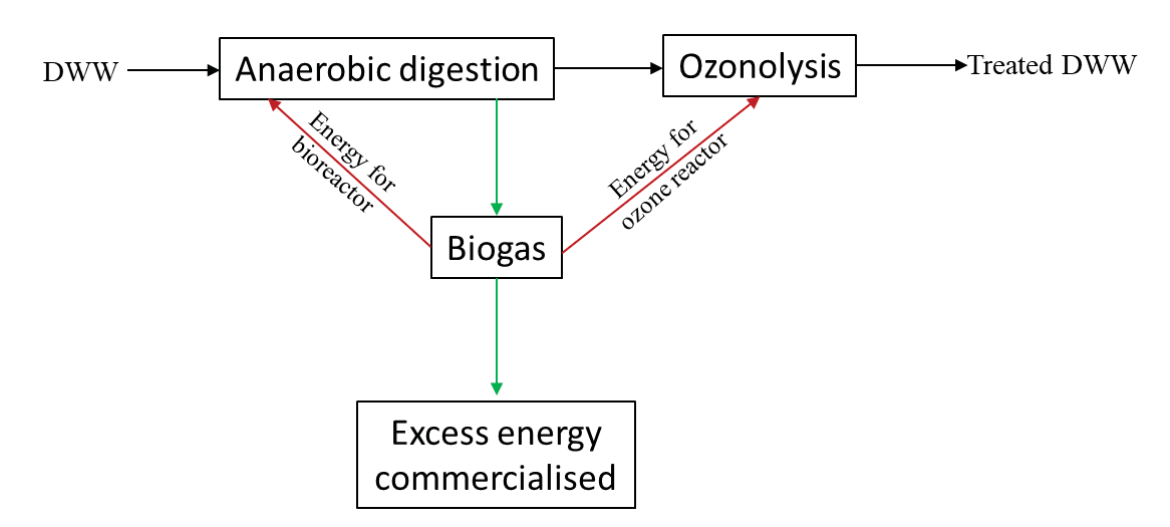


Figure 5.1: Alternative uses for the biogas produced in the integrated anaerobic digestion and ozonolysis treatment of DWW.

In this chapter, the energy analysis of the integrated process was carried out to determine if the bioenergy produced from the anaerobic process could be used to supplement the energy requirement of the ozonolysis post-treatment. The cost analysis of using the bioenergy instead

of energy from the grid to run ozonolysis and meet other electrical energy requirement of the anaerobic process was carried out. By using the bioenergy produced instead of the energy from the grid, the reduction in carbon dioxide emission was determined.

5.1 Methodology

Performing a full economic evaluation of an integrated AD-ozonolysis system treating DWW, should take into consideration all the costs, including biodigester construction, engine generators installation and other accessories (Nogueira et al., 2015). In the current study, however, the economic analysis was only restricted to the biomethane produced and the energy demand of the major reactor components of the integrated system. Energy analysis based on laboratory-scale experiments was carried out to determine if the energy produced from the anaerobic process could be enough to supplement the energy requirement of the ozonolysis process. Electrical energy per order (EE/O) was used to calculate the energy consumption of the ozonation process (Eoz). The EE/O (kWhm⁻³order⁻¹) is defined as the electrical energy (kWh) required to degrade a contaminant by one order of magnitude in 1.0 m³ water, and it is expressed by (Shu et al., 2013):

$$E_{OZ} = \frac{P \times t \times 1000}{V \times 60 \times \log{\binom{C_i}{C_f}}}$$
 (5.1)

where P is the ozone generator power (kW), t is the ozonolysis duration (minutes), V is the amount of substrate (L), C_f and C_i , respectively, are the final and initial substrate concentrations (Apollo et al., 2016). Dilution of the anaerobic effluent is sometimes necessary before ozonolysis post-treatment. Also, since the ozone reactor was coupled to an external air compressor, the electrical energy requirement of the compressor had to be taken into consideration. Thus, the electrical energy consumption of the ozone reactor taking into consideration dilution and the air compressor was determined using a modified electrical energy per order (E_{OZ}) as;

$$E_{OZ} = \frac{(P_{ozone} + P_{compressor}) t \times 1000}{V \log \frac{C_{i}}{C_{c}}} \times DF$$
(5.2)

where P_{ozone} and $P_{compressor}$ are the ozone reactor power (kW) and air compressor power, respectively, and DF is the dilution factor.

The energy produced by the anaerobic process was calculated as (Moraes et al., 2014):

$$E_{bio} = LHV_{CH_4} \times E_{COD} \times C_{COD} \times \alpha_{CH_4}$$
 (5.3)

where E_{bio} is the AD energy production kWh/m³, LHV_{CH_4} is the low heating value of methane which is 38 MJ/m³ (10.55 kWh/m³), E_{COD} is the COD removal efficiency, C_{COD} is the total COD fed to the reactor (kg COD) and α_{CH_4} is the methane production coefficient (m³/kg COD removed).

Energy ratio (ε) , which is the efficiency indicator, of the integrated system was calculated as

$$\varepsilon = \frac{E_{bio}}{E_{oz}} \times 100\% \tag{5.4}$$

where E_{OZ} is the ozonolysis process energy consumption (kWh/m³), and E_{bio} is the bioenergy produced by the anaerobic process (kWh/m³).

To evaluate the energy efficiency and the environmental impact of the integrated process, the electricity from the national grid that was saved as a result of the application of electricity from bioenergy was determined. The conversion of biomethane to electricity was estimated assuming cogeneration (biogas combustion for heat and electricity) and using a generator with an overall output efficiency of 78%, of which 33% was electricity and 45% heat (Moraes et al., 2015). The electricity generated from biomethane was given as;

$$El_{bio} = 0.33[E_{bio}] ag{5.5}$$

where El_{bio} is the electricity generated from biomethane per unit effluent volume (kWh/m_{feed}³), and E_{bio} is the total bioenergy from the anaerobic digestion (kWh/m $^{3}_{feed}$).

The heat energy (EH_{bio}) produced during the conversion of biomethane to electricity was determined as:

$$EH_{bio} = 0.45[E_{bio}] ag{5.6}$$

The carbon dioxide emission (CE) when electricity from the national grid was applied to power ozonolysis process was calculated as a product of electricity requirement of the ozone generator (kWh/m³) and the baseline grid emission factor of 0.957 kg CO₂equivalent/kWh of electricity used (Spalding-Fecher, 2011). The carbon dioxide emission reduction (CER) when electricity from biomethane was presumably used to power the ozone generator as an alternative energy source, replacing that from the national grid was calculated as;

$$CER = GEF * El_{bio} ag{5.7}$$

where CER is the carbon dioxide emission reduction (kg CO₂e/m³), GEF is the grid emission factor (0.957 kg CO₂e/kWh), and El_{bio} is the electricity generated from biomethane (kWh/m³) and presumably applied to power the ozone generator.

5.2 Results and discussion

5.2.1 Energy analysis

The energy analysis for AD was done based on potential electrical energy generated from the biogas produced by the anaerobic process at the OLR of 15 kg COD/m³/d, total biogas production of 10 L/d at steady state for every COD reduction of 75%. The biogas had an average methane composition of 70%. The total bioenergy produced from the anaerobic process (E_{bio}) was equivalent to 78.33 kWh/m³. If a biogas conversion to heat and electricity using a generator with 78% efficiency is assumed, then the total electricity from biogas (El_{bio}) will be 25.85 kWh/m³ and thermal energy (EH_{bio}) of 34.47 kWh/m³ (Figure 5.2).

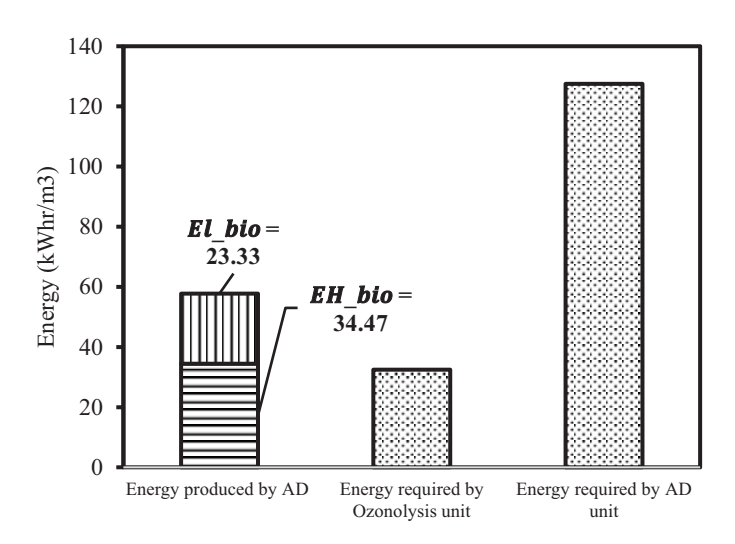


Figure 5.2: Energy produced by anaerobic digestion and required by ozonolysis and AD units in the integrated process treating of DWW.

For the ozonolysis posttreatment, the energy required for decolourising the anaerobic effluent by up to 75% was determined to be 32 kWh/m³ (Figure 5.2). The total electricity from biogas (El_{bio}) of 23.33 kWh/m³ can be used to meet up to 75% of the energy requirement of the ozonolysis posttreatment, while the thermal energy (EH_{bio}) of 34.47 kWh/m³ can meet up to 90% of heat energy requirement for the AD reactor. The use of the electricity and heat energy

produced from biogas to supplement the total energy requirements of the integrated system could achieve up to 50% energy savings.

5.2.2 Cost analysis and carbon dioxide emission reduction

The application of the bioenergy to supplement the energy requirements of the integrated process instead of relying solely on the electricity from the grid could reduce the carbon dioxide emission, as shown in Figure 5.3a. Using the electricity from biogas of 25.85 kWh/m³ to supplement the energy requirement of the ozonolysis process could lead to a CER of 24.73 kg CO₂e/m³. The thermal energy from biogas of 34.47 kWh/m³, if used for heating the bioreactor, could lead to a CER of 32.98 kg CO₂e/m³. Application of the total Ebio to 78.33 kWh/m³ could achieve a maximum CER of 74.65 kg CO₂e/m³.

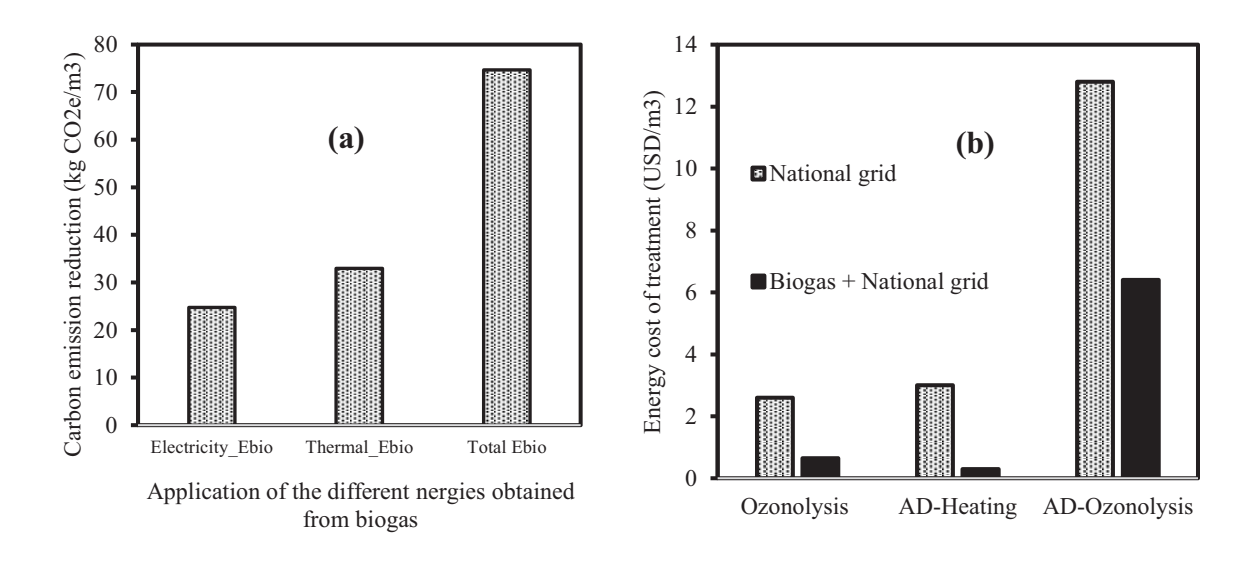


Figure 5.3: (a) Carbon emission reduction scenarios resulting from the use of the bioenergy produced to supplement different energy requirements of the integrated AD-ozonolysis system, and (b) Comparison of costs when using energy from national grid vs. supplementing the energy requirements with the energy produced from biogas.

The cost analysis was based on the cost reduction resulting from the possible application of the electricity generated from biomethane to run the anaerobic and ozonolysis processes, by applying the cost of electricity unit of 0.08 USD/kWh (Yasar et al., 2015). The total electricity requirement of the integrated system, including ozone generator, anaerobic unit, and other major electrical components, was determined to be 159.96 kWhr/m³ costing approximately 15.83 USD/m³ (Table 5.1). Using the total bioenergy produced of 78.33 kWh/m³ to supplement the energy requirement of the integrated system could result in up to 50% savings on the total energy cost as shown in Figure 5.3b.

Table 5.1: Total energy requirement for the different units of the integrated system

| Unit | Components | Power Rating (kW) | Duration (Hours) | Energy Requirement (kWhr/m³) | Energy cost (USD/m³) |
|------------|--------------------|-------------------|------------------|------------------------------|----------------------|
| Anaerobic | Heating | 0.5 | 0.15 | 37.5 | 3 |
| | Recirculation pump | 0.012 | 15 | 90 | 7.2 |
| Ozonolysis | Reactor + Air | 0.12 | 0.75 | 32.46 | 2.6 |
| | compressor | | | | |
| | Total | | | 159.96 | 12.8 |

5.2.3 Comparison of integrated AD-ozonolysis with other treatment options

In the current study, the bioenergy from AD could meet up to 75% of energy requirement of the ozonolysis process and meet > 90% of the heat energy requirement of the AD unit, leading to 50% savings on energy from the grid, and a CER of 122.33 kg CO₂e/m³. In our previous study focusing on an integrated AD-photodegradation treatment process, the electricity from biogas could only meet 25% of the energy requirement for the photodegradation post-treatment process with a CER of 68.8 kg CO₂e/m³ when heat produced was used to heat the AD unit (Apollo et al., 2016). In a study where the electricity from biogas obtained from an industrial scale plant was used to power homes, a CER of 55 kg CO₂e/m³ was reported (Yasar et al., 2015b). Based on the comparisons, the integrated AD-ozonolysis system is the most promising given the highest CER of 122 kg CO₂e/m³ and lower energy demand for ozonolysis posttreatment than photodegradation. For large-scale-industrial applications, the capital cost which depends on the reactor size should be considered. Moreover, it may be necessary to install a desulphurisation unit for biogas cleaning before conversion into electricity and heat.

CHAPTER 6: OZONOLYSİS PRE-TREATMENT OF WASTE ACTİVATED SLUDGE FOR SOLUBİLİZATİON AND BİODEGRADABİLİTY ENHANCEMENT

6 Introduction

The management of the excess waste activated sludge (WAS) from municipal wastewater treatment plants accounts for between 25-60% of the total treatment costs (Demir and Filibeli, 2012; Zhou et al., 2017). Recently the enhancement of anaerobic digestion (AD) process for WAS stabilization, reduction, and energy recovery in the form of methane gas has aroused great interest (Silvestre et al., 2015). However, anaerobic digestion of WAS suffers from high retention times, low methanogenic production, and an overall 30-35% dry solids degradation (Ali Shah et al., 2014). To improve the AD process, implementation of a pre-treatment method is necessary (Demir and Filibeli, 2012; Zhou et al., 2017).

Ozonolysis, which is an advanced oxidation process (AOP) is considered most effective for sludge disintegration because it does not lead to a significant increase in salt concentration and has no chemical residues in comparison to other pre-treatment techniques (Chu et al., 2009). Through ozonolysis, organic matter can be released from the sludge into the solution as a result of the breaking and solubilization of the hard cellular membrane (Liu et al., 2017). The role of ozonolysis pre-treatment is to partially oxidize the biorecalcitrant component of WAS to release biodegradable products (Dobslaw et al., 2017). To avoid over-oxidation of the released biodegradable components, the ozonolysis dose and time have to be optimized (Chaiprapat and Laklam, 2011).

The aim of this chapter was to carry out ozonolysis pre-treatment of WAS for sludge solubilization and to monitor the effect of pre-treatment on anaerobic digestion. Of major interest was the understanding of the ozonolysis process based on the rapture of the proteinaceous cell wall leading to nutrients (proteins, carbohydrates, nitrates, and phosphates) speciation, their release into the supernatant and suitability for a possible ensued AD process. Also, the sludge properties were determined before and after ozonolysis through thermogravimetric and infrared spectroscopic studies.

6.1 Materials and methods

6.1.1 Materials and methods

Sodium thiosulphate, phenol, bovine serum albumin (BSA), methanol, phosphoric acid, Bradford reagent, Coomassie brilliant blue, potassium iodide (KI), sulphuric acid, hydrochloric

acid, silver sulphate, potassium dichromate, starch, and sodium hydroxide were all purchased from Merck Limited, South Africa. The chemicals were of analytical grade and were used as received. All standard and working solutions were prepared using ultra-pure distilled water.

6.1.2 Waste activated sludge

The waste activated sludge (WAS) was sourced from a secondary settler of a local municipal wastewater treatment (WWT) plant in Vanderbijlpark, Gauteng, South Africa. The WAS was filtered through a 450 microns microfilter to remove large solid particles then further analyzed to determine its physical and chemical characteristics. Table 6.1 gives the determined characteristics of the sludge.

6.1.3 Ozonolysis experiments

The waste activated sludge was treated in a 4 L ozone reactor batch-wise for sludge solubilization and improved biodegradability. For every batch experiment, 2L of WAS was transferred to the reactor then subjected to ozonolysis. Gaseous ozone was generated from the air using an ozone generator coupled to an air compressor. The resulting ozone air mixture was then bubbled in an up-flow mode in the ozone reactor via a gas diffuser. To obtain different ozone dosages, the ozone flow rate was controlled using a manual valve, and the flow measured using an air rotameter.

6.1.4 Anaerobic digestion of WAS

For the anaerobic digestion of WAS, an already active upflow anaerobic sludge blanket (UASB) reactor of 3 L working volume of which 1 L consisted of sludge granules from an anaerobic digester treating municipal wastewater was used. Anaerobic digestion of the WAS was done in semi-batch mode with manual sampling and feeding. Each batch lasted six days (as determined by near-constant COD reduction and diminished biogas production after the 6th day), after which a new feed was introduced. The digestion temperature was maintained at 37°C using a heating tape wrapped around the reactor. In the first three batches, the reactor was fed with raw WAS (no pre-treatment), while in the subsequent three batches, ozone pre-treated WAS was fed. Daily biogas production was monitored. Also, samples were collected and analyzed.

6.1.5 Average oxidation state

The average oxidation state (AOS) of the DWW during ozonolysis was used to estimate the degree of oxidation of the substrate containing the oxidation by-products as well as the initial compounds. The AOS was calculated by;

$$AOS = 4 \times \frac{DOC - \frac{12}{32} \times COD}{DOC}$$
 (6.1)

where COD and DOC, respectively, are the total chemical oxygen demand and the dissolved organic carbon. The numbers 4, 12, and 32 represent the number of H atoms in a fully oxidizable state of C, the atomic mass of C and the atomic mass of O_2 , respectively. The AOS values range from -4 (fully oxidizable for CH₄ the most reduced state of C) to +4 (completely oxidized for CO_2 the most oxidized state of C). In the ozonolysis process, however, the increment observed in AOS (\triangle AOS), which was calculated by;

$$\Delta AOS = AOS_f - AOS_i = 4 \times \left(\frac{coD_i}{DOC_i} - \frac{coD_f}{DOC_f}\right) \times \frac{12}{32}$$
 (6.2)

6.1.6 Chemical analysis

Aliquot samples were withdrawn and analyzed for pH, total organic carbon (TOC), COD, BOD, total suspended solids (TSS), total solids (TS), dissolved organic carbon (DOC) total volatile solids (VSS), nitrates, phosphates, proteins, carbohydrates, and chlorides. The COD, BOD, TSS, TS, and VSS were analyzed according to the standard methods of analysis (APHA-AWWA-WEF, 2005). The cation concentration was determined from Ion Chromatography (882 Compact IC plus – Cation: intelligent ion chromatograph for determining anions and cations without chemical suppression). Fourier transform infrared, FTIR, analysis (Perkin-Elmer FT-IR/NIR Spectrometer, PerkinElmer, Waltham, MA, USA) was used in determining the presence of functional groups in the WAS. Differential thermal gravimetric (DTG) and thermal gravimetric (TGA) analyses were performed on the Perkin-Elmer Thermogravimetric analyzer TGA 400 instrument, to determine the thermal decomposition behavior of the dried WAS before and after ozonolysis. The amount of unutilized ozone captured in KI iodide solution was determined by the titrimetric method (Venkatesh et al., 2015; Bletterie et al., 2012). The concentration of carbohydrates and proteins in the supernatant was determined using the Bradford assay and phenol-sulphuric acid methods, respectively (Gong et al., 2009; Xiao et al., 2015).

6.2 Results and discussion

6.2.1 Characteristics of waste activated sludge

The physical and chemical characteristics of the obtained waste activated sludge are given in Table 6.1. The WAS had a soluble COD (COD_S) of 1400 mg/L, which was 20% of the total COD (COD_T) indicating that up to 80% of the COD was in the suspended solids. The DOC value of 122 mg/L also indicated a low concentration of the organic compounds in soluble form. With the DOC of 122 mg/L, a soluble COD value of 600 mg/L was expected. However, the higher soluble COD value of 1408 mg/L reported was partly contributed by the oxidation of ammonia, soluble proteins (20 mg/L) and other soluble inorganic compounds present in the WAS. The BOD₅:COD ratio of 0.1 confirmed the poor biodegradability of the WAS. The low biodegradability is attributed to the proteinaceous biomass cell wall, which hinders the rate determining hydrolysis step of AD (Ali Shah et al., 2014). Therefore, ozonolysis should be applied for the solubilization of the biorecalcitrant biomass cells.

Table 6.1: Physicochemical characteristics of municipal waste activated sludge

| Parameter | Units | Value | |
|-----------------------|-------|-------|--|
| рН | | 6.7 | |
| TSS | mg/L | 12.4 | |
| COD_T | mg/L | 6860 | |
| COD_S | mg/L | 1408 | |
| DOC | mg/L | 122 | |
| BOD_5 | mg/L | 901 | |
| TS | mg/L | 65.3 | |
| VSS | mg/L | 42.1 | |
| BOD ₅ :COD | | 0.1 | |
| Sulphate | mg/L | 18 | |
| Phosphate | mg/L | 67 | |
| Chloride | mg/L | 55 | |
| Soluble proteins | mg/L | 20 | |
| | | | |

6.2.2 Effect of ozone dosage

The effect of ozone dosage at different ozone flowrates is given in Figure 6.1. Selecting an appropriate ozone dosage is very important in optimizing the ozonolysis process. Low ozone dose would achieve low solubilization while an over-dose would lead to mineralization of already solubilized organics and a high concentration of ozone in the off-gas. As a result, the

process will not be economical. After 60 minutes of ozonolysis, the highest TSS reduction of 53% (12.4 to 5.6 mg/L) was achieved at a flow rate of 90 mg/min, while the lowest flow rate of 45 mg/min removed 47% of the TSS (Figure 6.1a). A corresponding observation was made with the evolution of DOC with the highest increase of 25% (from 120 to 152 mg/L) attained at the 90 mg/min flow rate (Figure 6.1b).

An increase in ozone flow rate from 45 to 90 mg/min led to an increase in ozone concentration in the reactor, which adequately dissolved the organic suspended solids leading to the reduced TSS. However, as the flow rate increased further, the TSS reduction decreased despite the increasing amount of supplied O₃ molecules. At high ozone flow rates above the optimal dose, the supplied gas forms larger bubbles, which significantly reduces gas hold-up resulting in reduced contact time between O₃ and the suspended solids leading to reduced efficiency (Quan et al., 2017; Ochieng et al., 2003).

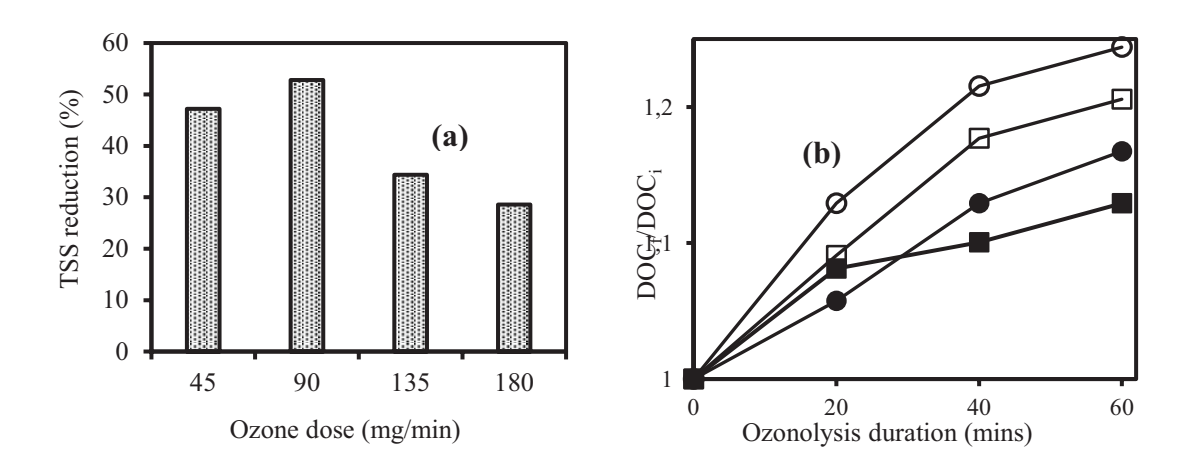
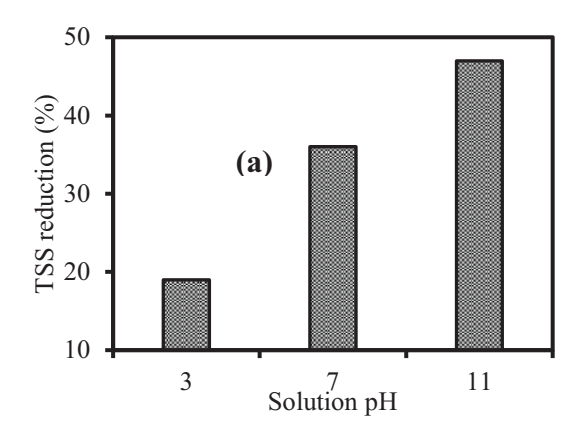


Figure 6.1: Effect of ozone dosage on; (a) TSS reduction after 60 minutes of ozonolysis and (b) evolution of DOC at different flow rates of 45 (\blacksquare), 90 (\circ), 135 (\square) and 180 (\bullet) mg/min.

6.2.3 Effect of initial pH

The highest TSS reduction of 47% (12.4 to 6.5 mg/L) was obtained at pH 11 as compared to 36% and 19% reductions at pHs of 7 and 3, respectively (Figure 6.2a). Similarly, the highest increase in DOC evolution of 55% (122 to 190 mg/L) was achieved at pH 11 and the lowest value of 23% at pH 3 (Figure 6.2b). The reduction in TSS and increase in DOC are attributable to the solubilization of the suspended organic matter. Under acidic conditions, ozone selectively attacks parts of organic compounds containing C=C double bonds, aromatic rings, and negatively charged centres/sites containing atoms such as N, P, O, S (Bar Oz et al., 2018). The selective attack leads to partial solubilization hence the low increase in DOC

(Peña et al., 2003). The performance of ozone is superior under alkaline conditions because its half-life increases from 15 minutes, which is the case in an acidic/neutral condition, to 25 minutes after which it decomposes, leading to the formation of the highly reactive hydroxyl radicals (OH•). The OH• radicals unselectively react with all the organic compounds hence the highest increase in DOC at pH 11 (Egra et al., 2014; Kasiri et al., 2013; Bögner et al., 2018).



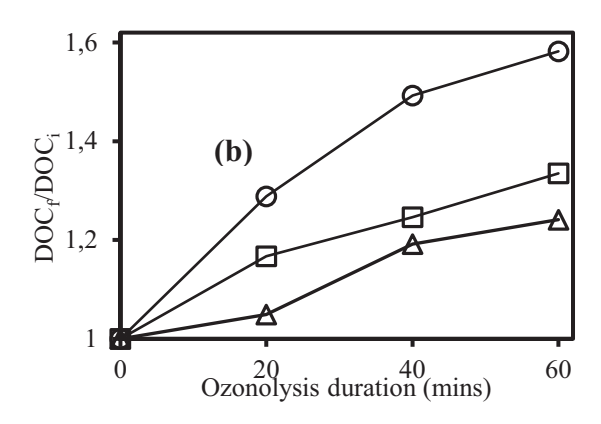


Figure 6.2: Effect of pH on ozonolysis of WAS on; (a) TSS reduction after 60 minutes of ozonolysis and (b) evolution of DOC at different pHs of 3 (Δ), 7 (\Box) and 11 (\circ) at ozone dosage of 90 mg/min.

6.2.4 Change in COD, biodegradability, and ozone transfer

Ozonolysis of the WAS was carried out at the optimal conditions of pH 11 and ozone flow rate of 90 mg/min. Figure 6.3 shows the changes in total COD (COD_T) and soluble (COD_S), and ozone transfer. The COD_T decreased by 42% after 2 hours of ozonolysis (Figure 6.3a). Consequently, the COD_S increased by 41% after 60 minutes of ozonolysis then reduced with additional ozonolysis time. The decrease in COD_T and the subsequent increase in COD_S was attributed to the solubilization of the suspended solids (sludge) present in the WAS. However, the extended ozonolysis period past the 60th minute could have led to mineralization of the already solubilized organic matter hence the observed decrease in COD_S (Gomes et al., 2013; Ariunbaatar, Panico and Frunzo, 2014). Also, the low reduction in COD_T during the extended period from the 80th minute indicates that most of the oxidizable organic solids had already been solubilized within the first 60 minutes. Based on these findings, the duration of ozonolysis should be minimized to reduce excessive energy consumption and depletion of organic carbon if anaerobic digestion is to be applied downstream to the ozonolysis process. (Fatoorehchi et al., 2018; Yan et al., 2009; Lee et al., 2005).

As observed in Figure 6.3b, the ozone transfer efficiency decreased with increasing duration of ozonolysis after every 20 minutes interval. In the first three intervals (60 minutes of

ozonolysis), more than 90% transfer was achieved and was considered efficient. As the ozonolysis continued beyond the 60th minute, more of the target organic contaminants were already degraded leading to reduced ozone transfers of 84, 81 and 76% in the 4th, 5th and 6th intervals, respectively.

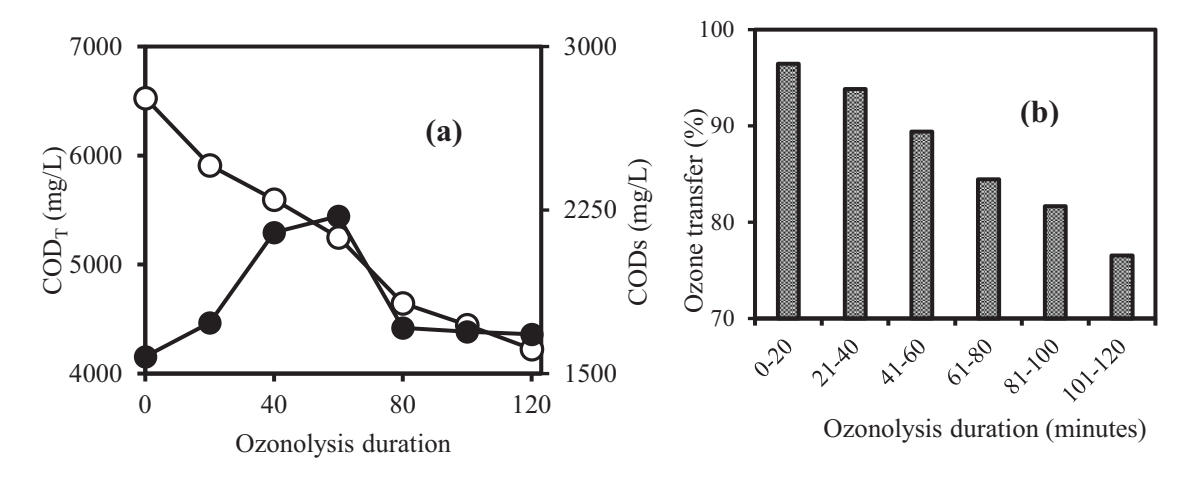


Figure 6.3: Change in; (a) COD_T (\circ) and COD_S (\bullet), and (b) ozone transfer during ozonolysis at pH 11 and 90 mg/min ozone dosage.

Improved biodegradability due to ozonolysis was confirmed by the increases in AOS from -1.5 to 0.9, as shown in Figure 6.4a. Also, in Figure 6.4b, the BOD₅:COD ratio increased from 0.1 to 0.21 while the pH decreased from 11 to 9.68. The increase in oxidation state could be attributed to the solubilization of the organic solids by the degradation of the aromatic groups and formation of aliphatic structures with functional groups such as -COOH, -OH, and -CHO as indicated. Aliphatic structures contain higher oxidation state carbons than aromatic carbons. Moreover, the decrease in basicity could be due to the formation of easily biodegradable acidic intermediate compounds such as acetic acids and humic substances (Sangave et al., 2007).

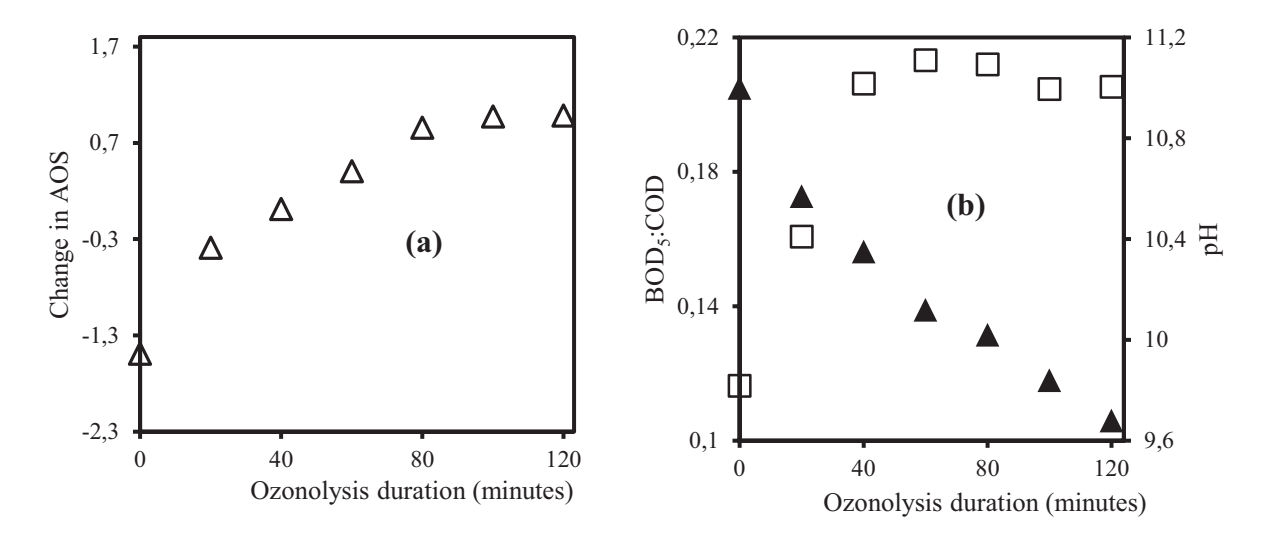


Figure 6.4: (a) Change in AOS during ozonolysis at pH 11 and 90 mg/min ozone dosage, and (b) change in BOD₅:COD (\square) and pH (\blacktriangle), during ozonolysis at pH 11 and 90 mg/min ozone dosage.

6.2.5 Sludge solubilization mechanism

Anions, proteins, and carbohydrates speciation

The mechanism of WAS solubilization was monitored through changes in cations, proteins, and carbohydrates concentration in the supernatant, as shown in Figure 6.5. The WAS organic fraction majorly consists of a biomass cell with a structure that includes hard cell walls, membrane cell nuclei, and extracellular polymeric substances (EPS). The hard cell walls and EPS, which are the major constituents of the WAS organic fraction, are mainly composed (up to 80%) of polysaccharides (PS), proteins (PS), and humic substances. Moreover, during the AST process, the microorganisms absorb nutrients such as phosphates, sulphates, and nitrates leading to the development of the hard cell walls (Sheng et al., 2010; Zhang et al., 2015; Anjum, Al-Makishah et al., 2016; Zou et al., 2017). The ozonolysis of WAS caused the hard cell walls to rapture and solubilized the EPS, thereby releasing the cellular contents. This led to the observed increase in sulphates (18 to 45 mg/L) and nitrates (0 to 85 mg/L) as shown in Figure 6.5a, and carbohydrates from 0 to 102 mg/L (Figure 6.5b).

Whereas an increase in protein concentration was expected as reported by Zang et al. (2015), the observed decrease from 20 to 0.5 mg/L (Figure 6.5b) could have resulted from the oxidation of the released protein by ozone into nitrates hence the significant increase in the dissolved nitrate concentration observed (Figure 6.5a). Ozonolysis did not affect the chloride while the phosphate concentration reduced from 67 to 37 mg/L despite an expected increase given the release of the cellular phosphorus content. Metal elements such as Al, Fe, Mg, and Ca present

in WAS could have combined with the phosphate ions forming poorly soluble compounds, hence the decrease (Zou et al., 2017).

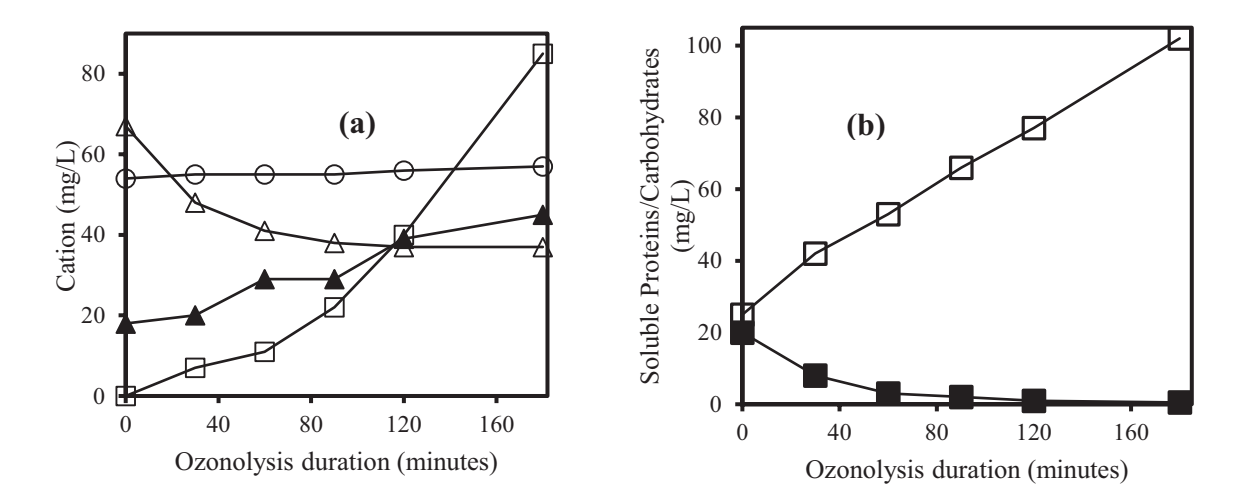


Figure 6.5: Change in (a) cations concentration sulfate (\triangle), nitrate (\square), phosphate (\triangle) and chloride (\circ), and (b) total proteins (\blacksquare) and carbohydrates (\square) concentration during ozonolysis of WAS.

Thermal gravimetric and FTIR analyses of WAS

The effect of ozonolysis on sludge solubilization was further monitored through characterization of raw WAS (before ozonolysis) and treated WAS (after ozonolysis) using TGA (Figure 6.6a) and FTIR analyses (Figure 6.6b). The WAS substrates were first dried at 100°C for 1 hour before analysis. Figure 6.6a gives the thermogravimetric behavior of the WAS before and after ozonolysis, heated from 30 to 1000°C at a constant heating rate of 30°C per minute. Table 6.2 gives the weight loses at the different phases of combustion. The TGA curves were almost similar from 30°C to around 420°C, where they intersected. Beyond 420°C, the curve for WAS before ozonolysis was greater than that after ozonolysis indicating that the residues had a greater mass for the former than the later (Zheng et al., 2018). The reduced mass of residues of the WAS after ozonolysis was caused by the solubilization of the organic content of the sludge such as the hard cell walls, which mainly decomposed in the temperature range between 180 and 480°C.

In phase I of combustion (Table 6.2) for the sludge before and after ozonolysis, weight loses of 34%, and 39% were observed, respectively. Ozonolysis had led to the rapture of cells allowing for the release of the pore and bound water during thermal treatment hence the higher weight loss for the WAS after ozonolysis than the WAS before ozonolysis in this phase. In the subsequent phase II, the WAS before ozonolysis had 20% weight loss as compared to 10% for

the WAS after ozonolysis. The higher weight loss of 20% was attributed to the thermal decomposition of proteins and cellulose in the WAS. In the ozonated WAS, however, ozonolysis had already led to the decomposition and release of the organic compounds such as cellulose and proteins hence the significantly reduced weight lose during the thermal treatment (Lin et al., 2016; Ren et al., 2017).

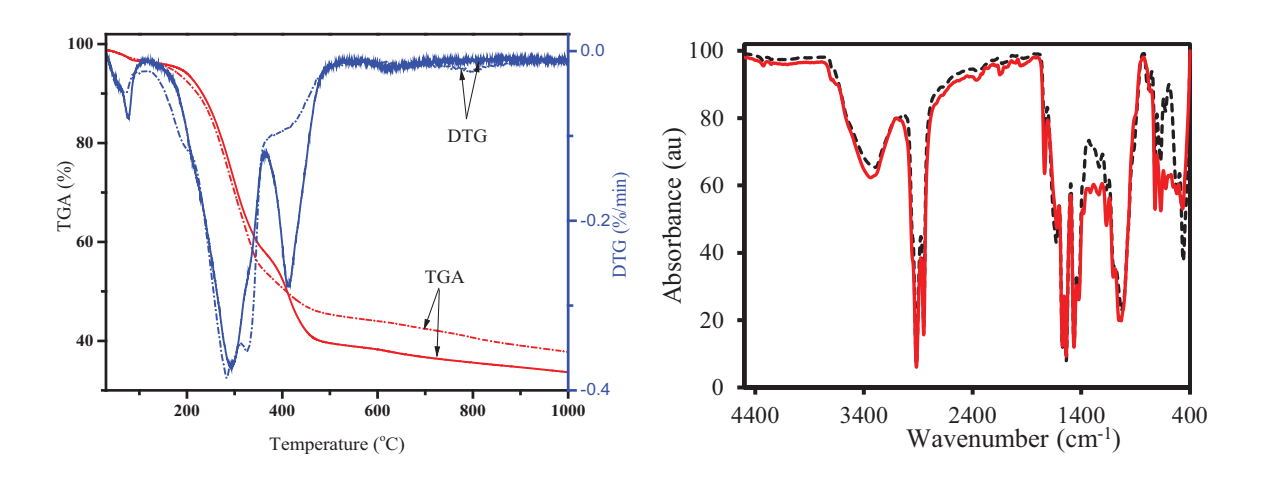


Figure 6.6: (a) DTG and TGA curves of dried sludge before (–) and after (…) ozonolysis, (b) FTIR spectra of dried sludge before (–) and after (…) ozonolysis.

The FTIR spectra of the sludge before and after ozonolysis were almost similar with broad bands between 3300 and 3500 cm⁻¹, attributed to NH or OH stretching vibrations, as shown in Figure 6.6b. The bands around 2900, 1660, 1550, 1040 and 600 cm⁻¹, respectively, corresponded to C-H stretching, CO₂ antisymmetric stretching, NH³⁺ stretching in amino acids, C=O stretching, and C-O stretching in carbohydrates (Xiao et al., 2015). In the ozonated sludge spectrum, the peaks attributed to the proteins and carbohydrates were reduced, indicating their release from the sludge into the aqueous phase during ozonolysis.

Table 6.2: Weight loss at different phases of combustion of dried WAS

| Phase | Before ozonolysis | | After Ozonolysis | |
|-------|------------------------|-----------------|------------------------|-----------------|
| | Temperature range (°C) | Weight loss (%) | Temperature range (°C) | Weight loss (%) |
| I | 30-197 | 7.294 | 30-194 | 5.398 |
| II | 197-395 | 34.127 | 194-349 | 38.922 |
| III | 395-480 | 18.502 | 349-467 | 9.704 |
| IV | 480-997 | 6.203 | 467-997 | 8.393 |
| Total | 30-1000 | 66.126 | 30-1000 | 62.417 |

6.2.6 Effect of ozone pre-treatment on anaerobic digestion of WAS

The COD and TSS reductions during AD of raw WAS and ozone pre-treated WAS are given in Figure 6.7a and b, respectively. The pre-treated WAS had increased COD and TSS reductions as compared to the raw WAS. Ozonolysis pre-treatment led to the rapture of the hard cell walls and partial solubilization of the sludge, availing the cellular contents and leading to improved degradation by the microorganisms. The most significant effect of pre-treatment on AD was observed in biogas production, as shown in Figure 6.7c and d. A comparison of the biogas production profiles showed that the pre-treated WAS had more than double daily biogas production than the raw WAS.

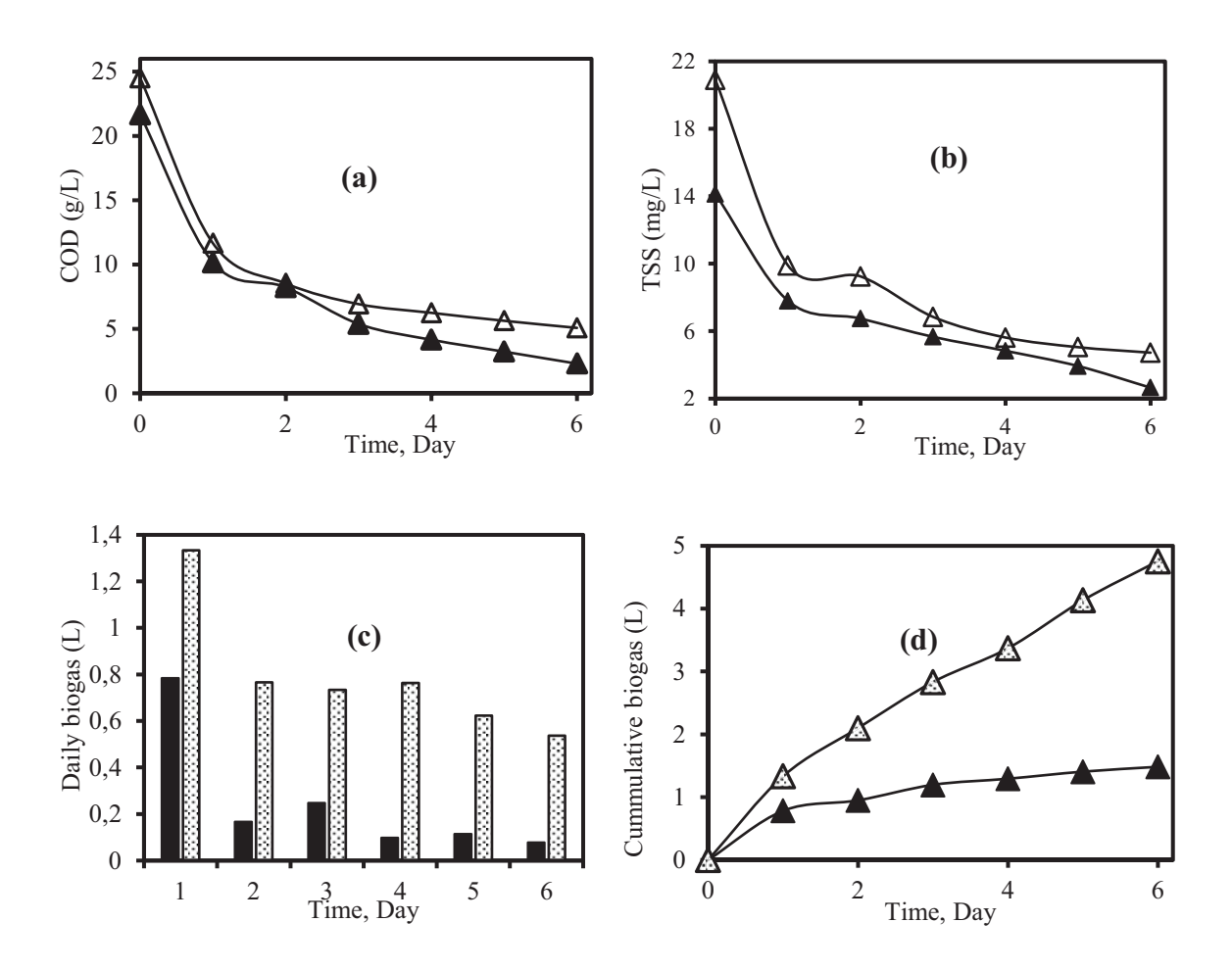


Figure 6.7: (a) COD and (b) TSS reduction, and (d) daily and (c) cumulative biogas production during anaerobic digestion of raw (Δ) and ozone pre-treated (\triangle) waste activated sludge.

The daily biogas production was higher for the pre-treated WAS at the beginning of digestion and remained relatively high with continued digestion than the raw WAS, which had a significantly diminished production after the first day. The pre-treated WAS had a higher cumulative biogas production of 4.75 L on day six as compared to the raw WAS with 1.48 L

(Figure 6.7d). Ozonolysis pre-treatment solubilized part of the organic matter, which was then easily converted to biogas. The significant increase in biogas production indicates that a major fraction of the solubilized matter was converted to biogas (Kim et al., 2013; Sosnowski et al., 2008).

6.2.7 Comparison of ozonolysis with other pre-treatment methods

Table 6.3 shows an overall evaluation of pre-treatment methods with respect to the results of the subsequent anaerobic digestion. Ozonolysis pre-treatment (from the current study) led to the highest increase (230%) in biogas production as compared to other methods. The remarkable increase could be a result of the 50% reduction in TSS, resulting in a 25% increase in DOC during pre-treatment. Ozonolysis pre-treatment is a feasible solution and can overcome the limitations associated with other technologies such as high energy and cost (ultrasonic, microwave), excess water use (wet oxidation), catalyst recovery (catalytic oxidation) and low acidic medium (Fenton) (Anjum et al., 2016).

Table 6.3: Comparison of ozonolysis with other pre-treatment methods

| Pre-treatmen | nt | | | |
|--|--|--|--|--|
| Method | Results | Results of subsequent anaerobic treatment | | |
| ^a Bacterial Extracellular polymeric substance | | Suspended solids reduction=48.5% COD | | |
| enzymatic | decreased to 40mg/L | solubilization =47.3% NR | | |
| ^a Fenton | Sludge disintegration increased by 24% | Methane production increased by 27% | | |
| ^a Thermal | Soluble carbon concentration, nitrogen, and phosphorus increased by 165%, 16%, and 24%, respectively | Methane production increased by 29% | | |
| ^a Alkali | Sludge viscosity reduced | Methane production increased by 34% | | |
| ^a Low thermal | Sludge disintegration increased by 25% | Methane production increased by 21% | | |
| ^a High | 36% of active Heterotrophs | Increase in total mass by 21% | | |
| pressure | converted to readily | | | |
| thermal | biodegradable COD and 64% | | | |
| hydrolysis | remaining to slowly | | | |
| | biodegradable COD | | | |
| ^a UV- | Soluble COD concentration | Methane production= 1266.7 ml/l- sludge, VS | | |
| Photocatalysis | increased from 1087.2 to 1451.6 mg/l for 8h pretreatment | reduction=67.4%,Total COD reduction=60.5% | | |
| ^b Ozonolysis | 50% reduction in TSS, DOC | Improved TSS and COD reductions, and a 230% | | |
| | increased by 25%, nitrates | increase in the cumulative biogas production | | |
| | increased from 0 mg/l to 85 mg/l, | | | |
| | carbohydrates increased four-fold | | | |

References; ^a(Anjum et al., 2016) and ^b(Current study).

CHAPTER 7: CONCLUSION AND RECOMMENDATIONS

7 Project conclusions and recommendation

Alcohol distillation, one of the major industrial processes, generates a copious amount of wastewater known as distillery wastewater (DWW). The DWW due to its characteristics such as high organic load and an intense dark-brown colour pose serious environmental effects if discharged without proper treatment. Also, there is an increasing generation of large amounts of waste activated sludge (WAS) from the various municipal wastewater treatment plants. The WAS, if not properly remediated, can potentially cause health problems due to its pathogenic and toxic pollutant content. The main aim of this study was to integrate anaerobic digestion (AD) and ozonolysis, an advanced oxidation process (AOP), for the treatment of DWW and WAS. The study sought to obtain the optimal conditions of the individual processes and to study reactor hydrodynamics using simulation tools to aid in designing the integrated process. Moreover, energy, cost and environmental analysis of the integrated system was considered for practical applicability purposes.

7.1 Conclusions

The hydrodynamics in a bubble column reactor was simulated using computational fluid dynamics (CFD), and the optimum grid and geometry size, the effect of turbulence model and interfacial forces investigated. A grid of 98,000 nodes was found to be optimum while simulating the full reactor geometry was deemed necessary in order to eliminate errors due to the physics of the flow. A combination of different interfacial forces resulted in different levels of accuracy depending on the hydrodynamic parameter under investigation. Nevertheless, modelling all the interfacial forces during the simulation was observed to result in accurate simulation of all the different hydrodynamic parameters. Using the CFD model from the bubble column simulation and adjusting for the presence of a solid phase, the hydrodynamics in the fluidized bed reactor could be simulated.

For the treatment of DWW, anaerobic digestion achieved a high COD reduction (up to 72%) and biogas production of 0.33 m³/kg COD. However, despite the high COD removal, a considerable amount of biorecalcitrant compounds still existed, contributing to a high residual COD of 4 500 mg/L and biorecalcitrant colour in the anaerobically digested effluent. Ozonolysis post-treatment degraded the biorecalcitrant melanoidins leading to a colour reduction above 80% and solubilized the sludge washed out from the AD unit. For the highly

coloured anaerobically digested DWW, dilution before ozonolysis post-treatment was found necessary. The best operating conditions of pH 4, dilution factor of ×2, and dosage of 45 mg O³/L/min were established. The ×2 dilution required the least energy of 2 kWh/m³ to remove 75% of the colour within 45 minutes. Higher dilutions resulted in rapid colour reduction but with low ozone transfers and increased energy requirements. Due to reduced mass transfer, higher ozone dosages resulted in low colour reductions low ozone transfers. Thus, for wastewater streams with a favourable biodegradability (BOD:COD ratio of 0.48), but with a biorecalcitrant colour, anaerobic digestion followed by ozonolysis can effectively remove the high organic load and colour.

Kinetic analysis of the integrated AD-ozonolysis system treating DWW showed that the HRT of anaerobic digestion was 20 times higher than that of ozonolysis. In an integrated AD-AOP system for DWW treatment, therefore, the AD to ozonolysis reactors ratio should be 20:1 to allow for continuous operation. Alternatively, since AD is a much slower process than ozonolysis post-treatment, a holding tank for the anaerobically digested effluent can be installed to enable the operation of ozonolysis in batch or to allow for an easy control which may lead to reduced power consumption. From the energy analysis, the electricity from biogas could subsidize up to 75% of the energy requirement of the ozonolysis process, while the thermal energy of 34 kWh/m³ could meet > 90% of the heat energy requirement of the AD unit. Using the total bioenergy produced to supplement the total energy requirement of the integrated system (AD and ozonolysis) can lead to 50% savings on energy from the grid, and a carbon dioxide emission reduction CER of 122 kg CO₂e/m³. Thus, based on the pollution removal efficiency, energy, cost, and environmental analysis, the industrial application of the integrated AD-ozonolysis system for DWW treatment is feasible.

For the treatment of waste streams with very low biodegradability (BOD:COD < 0.1) and high solid content such as WAS, application of ozonolysis as a pre-treatment, followed by AD, was found to be effective. Ozonolysis solubilized the suspended organic matter in WAS through the rapture of hard cell walls, thereby releasing the biodegradable cellular contents and significantly improving the BOD₅:COD ratio from 0.06 (non-biodegradable) to 0.16 (biodegradable). In the ensuing AD process, the pre-treatment led to an improved reduction of the total suspended solids and COD and a remarkable increase in biogas production from 0.059 to 0.21L biogas/g feed.

Overall, the study has established that an integrated AD-ozonolysis system can be effective for the treatment of WAS and DWW. The configuration of the AD-ozonolysis process is, however, substrate specific with ozonolysis best applied as a pre-AD and post AD for WAS and DWW, respectively. The main objective, which was to integrate anaerobic digestion and ozonolysis for effective treatment of distillery wastewater and waste activated sludge, has been achieved. The knowledge presented herein is intended to assist in the development of integrated AD-AOP treatment systems for wastewater remediation.

7.2 Recommendations

The effect of hydrodynamics on the performance of the reactors was investigated using nanoparticles. Further studies need to be carried out using catalyst particles of different sizes, and possibly lager than the ones used in the current study. This will provide information on the efficiency of small particles from the reaction kinetics perspective against the backdrop of the cost of separating such small particles. In such a study, CFD simulation could give an insight into the effects of hydrodynamics and mass transfer on the reaction kinetics and the cost of fluidization. This will further help in the energy and economic analysis of integrated processes.

This study has evaluated the application of an integrated AD-AOP DWW treatment with full energy, cost, and environmental analysis. The study has also determined the feasibility of applying the integrated system for waste activated sludge (WAS). Further study on WAS treatment is recommended. In the study focusing on an integrated system for WAS, it is important to carry out energy and economic analysis, including a possible nutrient recovery in the form of struvite (fertilizer) and biosolids for agricultural application.

REFERENCES

- ABELLEIRA, J., PÉREZ-ELVIRA, S.I.I., SÁNCHEZ-ONETO, J., PORTELA, J.R.R. AND NEBOT, E. 2012). Advanced Thermal Hydrolysis of secondary sewage sludge: A novel process combining thermal hydrolysis and hydrogen peroxide addition. *Resources, Conservation and Recycling*, 59, p. 52-57.
- ABELLEIRA-PEREIRA, J.M., PÉREZ-ELVIRA, S.I., SÁNCHEZ-ONETO, J., DE LA CRUZ, R., PORTELA, J.R. AND NEBOT, E. (2015). Enhancement of methane production in mesophilic anaerobic digestion of secondary sewage sludge by advanced thermal hydrolysis pretreatment. *Water Research*, 71, p. 330-340.
- ADEKUNLE, K.F. AND OKOLIE, J.A. (2015). A Review of Biochemical Process of Anaerobic Digestion. *Advances in Bioscience and Biotechnology*, 6, p. 205-212.
- AKPAN, U.G. AND HAMEED, B.H. (2009). Parameters affecting the photocatalytic degradation of dyes using TiO₂-based photocatalysts: A review. *Journal of Hazardous Materials*, 170 (2-3), p. 520-529.
- ALI SHAH, F., MAHMOOD, Q., MAROOF SHAH, M., PERVEZ, A. AND AHMAD ASAD, S. (2014). Microbial ecology of anaerobic digesters: The key players of anaerobiosis. *The Scientific World Journal*.
- AMARAL-SILVA, N., MARTINS, R.C., CASTRO-SILVA, S. AND QUINTA-FERREIRA, R.M. (2016). Ozonation and perozonation on the biodegradability improvement of a landfill leachate. *Journal of Environmental Chemical Engineering*, 4 (1), p. 527-533.
- AMAT, S., SAISRIYOOT, M., THANAPIMMETHA, A. AND SRINOPHAKUN, P. (2014). Decolorization and COD reduction of wastewater from ethanol production by Fenton oxidation. In *The 26" Annual Meeting of the Thai Society for Biotechnology and International Conference*. pp. 417-423.
- ANJUM, M., AL-MAKISHAH, N.H. AND BARAKAT, M.A. (2016). Wastewater sludge stabilization using pre-treatment methods. *Process Safety and Environmental Protection*, 102, p. 615-632.
- APHA-AWWA-WEF (2005). Standard Methods for the Examination of Water and Wastewater, Washington DC.
- APOLLO, S., ONYANGO, S. AND OCHIENG, A. (2014). UV / H 2 O 2 / TiO 2 / Zeolite Hybrid System for Treatment of Molasses Wastewater. *Iranian Journal of Chemistry and Chemical Enginering*, 33 (2), p. 107-117.
- APOLLO, S. AND AOYI, O. (2016). Combined anaerobic digestion and photocatalytic treatment of distillery effluent in fluidized bed reactors focusing on energy conservation. *Environmental technology*, 37 (17), p. 1-9.
- APOLLO, S., ONYANGO, M.S. AND OCHIENG, A. (2013). An integrated anaerobic digestion and UV photocatalytic treatment of distillery wastewater. *Journal of hazardous materials*, 261, p. 435-42.

- APOLLO, S., ONYANGO, M.S.M.S. AND OCHIENG, A. (2016). Modelling energy efficiency of an integrated anaerobic digestion and photodegradation of distillery effluent using response surface methodology. *Environmental Technology*, 3330 (19), p. 1-12.
- ARIMI, M.M., ZHANG, Y., GÖTZ, G., KIRIAMITI, K. AND GEIßEN, S.-U. (2014). Antimicrobial colorants in molasses distillery wastewater and their removal technologies. *International Biodeterioration & Biodegradation*, 87, p. 34-43.
- ARIMI, M.M., ZHANG, Y., GÖTZ, G. AND GEIßEN, S.-U. (2015). Treatment of melanoidin wastewater by anaerobic digestion and coagulation. *Environmental Technology*, 36 (19), p. 2410-2418.
- ARIUNBAATAR, J., PANICO, A., FRUNZO, L., ESPOSITO, G., LENS, P.N.L. AND PIROZZI, F. (2014). Enhanced anaerobic digestion of food waste by thermal and ozonation pretreatment methods. *Journal of Environmental Management*, 146, p. 142-149.
- ARIUNBAATAR, J., PANICO, A., ESPOSITO, G., PIROZZI, F. AND LENS, P.N.L. (2014). Pretreatment methods to enhance anaerobic digestion of organic solid waste. *Applied Energy*, 123, p. 143-156.
- BAR OZ, Y., MAMANE, H., MENASHE, O., COHEN-YANIV, V., KUMAR, R., IASUR KRUH, L. AND KURZBAUM, E. (2018). Treatment of olive mill wastewater using ozonation followed by an encapsulated acclimated biomass. *Journal of Environmental Chemical Engineering*, 6 (4), p. 5014-5023.
- BARUAH, S., PAL, S.K. AND DUTTA, J. (2012). Nanostructured Zinc Oxide for Water Treatment. *Nanoscience and Technology-Asia*, 2 (2), p. 90-102.
- BECHAMBI, O., NAJJAR, W. AND SAYADI, S. (2015). The nonylphenol degradation under UV irradiation in the presence of Ag-ZnO nanorods: Effect of parameters and degradation pathway. *Journal of the Taiwan Institute of Chemical Engineers*, p. 1-6.
- BLETTERIE, U., SCHILLING, K., DELGADO, L. AND ZESSNER, M. (2012). Ozonation as a Post-Treatment Step for Tannery Wastewater to Reduce Foam Formation in a River. *Ozone: Science and Engineering*, 34 (5), p. 397-404.
- BÖGNER, D., SCHMACHTL, F., MAYR, B., FRANZ, C.P., STRIEBEN, S., JAEHNE, G., LORKOWSKI, K. AND SLATER, M.J. (2018). Sludge Pre-Treatment through Ozone Application: Alternative Sludge Reuse Possibilities for Recirculating Aquaculture System Optimization. *Ozone: Science and Engineering*, p. 1-13.
- BORJA, R. AND BANKS, C.J. (1994). Kinetics of an upflow anaerobic sludge blanket reactor treating ice-cream wastewater. *Environmental Technology*, 15 (3), p. 219-232.
- BORJA, R., BANKS, C.J. AND WANG, Z. (1994). Performance and kinetics of an upflow anaerobic sludge blanket (UASB) reactor treating slaughterhouse wastewater. *Journal of Environmental Science and Health. Part A: Environmental Science and Engineering and Toxicology*, 29 (10), p. 2063-2085.
- BORJA, R., GONZALEZ, E., RAPOSO, F., MILLAN, F. AND MARTIN, A. (2002). Kinetic analysis of the psychrophilic anaerobic digestion of wastewater derived from the production of proteins from extracted sunflower flour. *J Agric Food Chem*, 50, p. 4628-4633.

- BOUGRIER, C., ALBASI, C., DELGENÈS, J.P. AND CARRÈRE, H. (2006). Effect of ultrasonic, thermal and ozone pre-treatments on waste activated sludge solubilisation and anaerobic biodegradability. *Chemical Engineering and Processing: Process Intensification*, 45 (8), p. 711-718.
- BRAGUGLIA, C.M., GIANICO, A., GALLIPOLI, A. AND MININNI, G. (2015). The impact of sludge pre-treatments on mesophilic and thermophilic anaerobic digestion efficiency: Role of the organic load. *Chemical Engineering Journal*, 270, p. 362-371.
- BROOMS, T.J., OTIENO, B.O., ONYANGO, M.S. AND OCHIENG, A. (2016). Photocatalytic degradation of aromatic compounds in abattoir wastewater. *International Journal of Environmental Sustainability*, 13 (1).
- BROOMS, T.J., OTIENO, B., ONYANGO, M.S. AND OCHIENG, A. (2018). Photocatalytic degradation of P-Cresol using TiO₂/ZnO hybrid surface capped with polyaniline. *Journal of Environmental Science and Health Part A Toxic/Hazardous Substances and Environmental Engineering*, 53 (2), p. 99-107.
- Buys, W.Y. (2015). Investigating The Effect Of Wine And Distillery Wastewater on The Efficacy of an Upflow Anaerobic Sludge Blanket (UASB) and Enhancing Biomass Immobilisation by the Addition of Magnetisable Foam Glass Particles (MP). *Masters Thesis Submitted to the University of Stellenbosch*.
- CHAIPRAPAT, S. AND LAKLAM, T. (2011). Enhancing digestion efficiency of POME in anaerobic sequencing batch reactor with ozonation pretreatment and cycle time reduction. *Bioresource Technology*, 102 (5), p. 4061-4068.
- CHAVAN, M.N., KULKARNI, M. V, ZOPE, V.P. AND MAHULIKAR, P.P. (2006). Microbial degradation of melanoidins in distillery spent wash by an indigenous isolate. *Indian Journal of Biotechnology*, 5 (3), p. 416-421.
- CHEN, C., LIANG, J., YOZA, B.A., LI, Q.X., ZHAN, Y. AND WANG, Q. (2017). Evaluation of an up-flow anaerobic sludge bed (UASB) reactor containing diatomite and maifanite for the improved treatment of petroleum wastewater. *Bioresource Technology*, 243, p. 620-627.
- CHEN, Y., HE, J., MU, Y., HUO, Y.-C., ZHANG, Z., KOTSOPOULOS, T.A. AND ZENG, R.J. (2015). Mathematical modeling of upflow anaerobic sludge blanket (UASB) reactors: Simultaneous accounting for hydrodynamics and bio-dynamics. *Chemical Engineering Science*, 137, p. 677-684.
- CHOWDHARY, P., RAJ, A. AND BHARAGAVA, R.N. (2018). Environmental pollution and health hazards from distillery wastewater and treatment approaches to combat the environmental threats: A review. *Chemosphere*, 194, p. 229-246.
- CHU, L., YAN, S., XING, X.H., SUN, X. AND JURCIK, B. (2009). Progress and perspectives of sludge ozonation as a powerful pretreatment method for minimization of excess sludge production. *Water Research*, 43 (7), p. 1811-1822.
- CIBIS, E., KRZYWONOS, M. AND MIŚKIEWICZ, T. (2006). Aerobic biodegradation of potato slops under moderate thermophilic conditions: Effect of pollution load. *Bioresource Technology*, 97 (4), p. 679-685.

- CONRADIE, A, SIGGE, G.O. AND CLOETE, T.E. (2014). Influence of Winemaking Practices on the Characteristics of Winery Wastewater and Water Usage of Wineries. *South African Journal of Chemistry*, 35 (1), p. 10-19.
- CROUSIER, C., PIC, J.-S., ALBET, J., BAIG, S. AND ROUSTAN, M. (2016). Urban Wastewater Treatment by Catalytic Ozonation. *Ozone: Science & Engineering*, 38 (1), p. 3-13.
- CRUZ-SALOMÓN, A., MEZA-GORDILLO, R., ROSALES-QUINTERO, A., VENTURA-CANSECO, C., LAGUNAS-RIVERA, S. AND CARRASCO-CERVANTES, J. (2017). Biogas production from a native beverage vinasse using a modified UASB bioreactor. *Fuel*, 198, p. 170-174.
- DAVID, C., ARIVAZHAGAN, M. AND TUVAKARA, F. (2015). Decolorization of distillery spent wash effluent by electro oxidation (EC and EF) and Fenton processes: A comparative study. *Ecotoxicology and Environmental Safety*, 121, p. 142-148.
- DEMIR, O. AND FILIBELI, A. (2012). Fate of return activated sludge after ozonation: An optimization study for sludge disintegration. *Environmental Technology (United Kingdom)*, 33 (16), p. 1869-1878.
- DJALMA NUNES FERRAZ JÚNIOR, A., KOYAMA, M.H., DE ARAÚJO JÚNIOR, M.M. AND ZAIAT, M. (2016). Thermophilic anaerobic digestion of raw sugarcane vinasse. *Renewable Energy*, 89, p. 245-252.
- DOBSLAW, D., SCHULZ, A., HELBICH, S., DOBSLAW, C. AND ENGESSER, K.H. (2017). VOC removal and odor abatement by a low-cost plasma enhanced biotrickling filter process. *Journal of Environmental Chemical Engineering*, 5 (6), p. 5501-5511.
- EBRAHIMI, A., HASHEMI, H., ESLAMI, H., FALLAHZADEH, R.A., KHOSRAVI, R., ASKARI, R. AND GHAHRAMANI, E. (2018). Kinetics of biogas production and chemical oxygen demand removal from compost leachate in an anaerobic migrating blanket reactor. *Journal of Environmental Management*, 206, p. 707-714.
- EQRA, N., AJABSHIRCHI, Y. AND SARSHAR, M. (2014). Effect of ozonolysis pretreatment on enzymatic digestibility of sugarcane bagasse. *Agricultural Engineering International: CIGR Journal*, 16 (1), p. 151-156.
- FATOOREHCHI, E., WEST, S., ABBT-BRAUN, G. AND HORN, H. (2018). The molecular weight distribution of dissolved organic carbon after application off different sludge disintegration techniques. *Separation and Purification Technology*, 194 (November 2017), p. 338-345.
- FUESS, L.T., GARCIA, M.L. AND ZAIAT, M. (2018). Seasonal characterization of sugarcane vinasse: Assessing environmental impacts from fertirrigation and the bioenergy recovery potential through biodigestion. *Science of the Total Environment*, 634, p. 29-40.
- GARCIA-SEGURA, S., BELLOTINDOS, L.M., HUANG, Y.H., BRILLAS, E. AND LU, M.C. (2016). Fluidized-bed Fenton process as alternative wastewater treatment technology—A review. *Journal of the Taiwan Institute of Chemical Engineers*, 67, p. 211-225.

- GHOSH RAY, S. AND GHANGREKAR, M.M. (2018). Comprehensive review on treatment of high-strength distillery wastewater in advanced physico-chemical and biological degradation pathways. *International Journal of Environmental Science and Technology*, 16 (1) p. 527-546.
- GNANAPRAKASAM, A., SIVAKUMAR, V.M.M., SIVAYOGAVALLI, P.L.L. AND THIRUMARIMURUGAN, M. (2015). Characterization of TiO₂ and ZnO nanoparticles and their applications in photocatalytic degradation of azodyes. *Ecotoxicology and environmental safety*, 121, p. 121-5.
- GOMES, A.C., SILVA, L., SIMÕES, R., CANTO, N. AND ALBUQUERQUE, A. (2013). Toxicity reduction and biodegradability enhancement of cork processing wastewaters by ozonation. *Water Science and Technology*, 68 (10), p. 2214-2219.
- GONG, A., BOLSTER, C., BENAVIDES, M. AND WALKER, S. (2009). Extraction and Analysis of Extracellular Polymeric Substances: Comparison of Methods and Extracellular Polymeric Substance Levels in Salmonella pullorum SA 1685. *Environmental Engeneering Science*, 26 (10), p. 1523-1532.
- GUAN, R., YUAN, X., WU, Z., JIANG, L., LI, Y. AND ZENG, G. (2018). Principle and application of hydrogen peroxide based advanced oxidation processes in activated sludge treatment: A review. *Chemical Engineering Journal*, 339, p. 519-530.
- HALDER, J. AND ISLAM, N. (2015). Water Pollution and its Impact on the Human Health. *Journal of Environment and Human*, 2 (1), p. 36-46.
- HAMPANNAVAR, U. AND SHIVAYOGIMATH, C. (2010). Anaerobic treatment of sugar industry wastewater by Upflow anaerobic. *International Journal of Environmental Sciences*, 1 (4), p. 631-639.
- HOARAU, J., CARO, Y., GRONDIN, I. AND PETIT, T. (2018). Sugarcane vinasse processing: Toward a status shift from waste to valuable resource. A review. *Journal of Water Process Engineering*, 24 (January), p. 11-25.
- HREIZ, R., LATIFI, M.A. AND ROCHE, N. (2015). Optimal design and operation of activated sludge processes: State-of-the-art. *Chemical Engineering Journal*, 281, p. 900-920.
- HU, W., THAYANITHY, K. AND FORSTER, C. (2002). A kinetic study of the anaerobic digestion of ice-cream wastewater. *Process Biochemistry*, 37 (9), p. 965-971.
- IBRAHIM, M.A.-R. (2014). Kinetics of anaerobic digestion of labaneh whey in a batch reactor. *African Journal of Biotechnology*, 13 (16), p. 1745-1755.
- IŞIK, M. AND SPONZA, D.T. (2005). Substrate removal kinetics in an upflow anaerobic sludge blanket reactor decolorising simulated textile wastewater. *Process Biochemistry*, 40 (3-4), p. 1189-1198.
- KASIRI, M.B., MODIRSHAHLA, N. AND MANSOURI, H. (2013). Decolorization of organic dye solution by ozonation; Optimization with response surface methodology. *International Journal of Industrial Chemistry*, 4 (1), p. 3.

- KHARAYAT, Y. (2012). Distillery wastewater: bioremediation approaches. *Journal of Integrative Environmental Sciences*, 9 (2), p. 69-91.
- KIM, D.H., CHO, S.K., LEE, M.K. AND KIM, M.S. (2013). Increased solubilization of excess sludge does not always result in enhanced anaerobic digestion efficiency. *Bioresource Technology*, 143, p. 660-664.
- KIM, J., KIM, K., YE, H., LEE, E., SHIN, C., MCCARTY, P.L. AND BAE, J. (2010). Anaerobic Fluidized Bed Membrane Bioreactor for Wastewater Treatment. *Environmental science & technology*, 45 (2), p. 576-581.
- KYTHREOTOU, N., FLORIDES, G. AND TASSOU, S.A. (2014). A review of simple to scientific models for anaerobic digestion. *Renewable Energy*, 71, p. 701-714.
- LEE, J.W., CHA, H.Y., PARK, K.Y., SONG, K.G. AND AHN, K.H. (2005). Operational strategies for an activated sludge process in conjunction with ozone oxidation for zero excess sludge production during winter season. *Water Research*, 39 (7), p. 1199-1204.
- LI, Z., TIAN, Y., DING, Y., WANG, H. AND CHEN, L. (2013). Contribution of extracellular polymeric substances (EPS) and their subfractions to the sludge aggregation in membrane bioreactor coupled with worm reactor. *Bioresource Technology*, 144, p. 328-336.
- LIANG, Z., WANG, Y., ZHOU, Y. AND LIU, H. (2009). Coagulation removal of melanoidins from biologically treated molasses wastewater using ferric chloride. *Chemical Engineering Journal*, 152 (1), p. 88-94.
- LIN, YAN, LIAO, Y., YU, Z., FANG, S., LIN, YOUSHENG, FAN, Y., PENG, X. AND MA, X. (2016). Co-pyrolysis kinetics of sewage sludge and oil shale thermal decomposition using TGA-FTIR analysis. *Energy Conversion and Management*, 118, p. 345-352.
- LIU, C., LEI, Z., YANG, Y. AND ZHANG, Z. (2013). Preliminary trial on degradation of waste activated sludge and simultaneous hydrogen production in a newly-developed solar photocatalytic reactor with AgX/TiO₂-coated glass tubes. *Water Research*, 47 (14), p. 4986-4992.
- LIU, G., YANG, Z., CHEN, B., ZHANG, J., LIU, X., ZHANG, Y., SU, M. AND ULGIATI, S. (2015). Scenarios for sewage sludge reduction and reuse in clinker production towards regional eco-industrial development: a comparative emergy-based assessment. *Journal of Cleaner Production*, 103, p. 371-383.
- LIU, M., ZHU, H., DONG, B., ZHENG, Y., YU, S. AND GAO, C. (2013). Submerged nanofiltration of biologically treated molasses fermentation wastewater for the removal of melanoidins. *Chemical Engineering Journal*, 223, p. 388-394.
- LIU, Y., WANG, H. LIN, XU, Y. XIANG, FANG, Y. YUAN AND CHEN, X. RONG (2017). Sludge disintegration using a hydrocyclone to improve biological nutrient removal and reduce excess sludge. *Separation and Purification Technology*, 177, p. 192-199.
- LOPEZ-LOPEZ, A., LEON-BECERRIL, E., ROSALES-CONTRERAS, M.E. AND VILLEGAS-GARCIA, E. (2015). Influence of alkalinity and VFAs on the performance of an UASB reactor with recirculation for the treatment of Tequila vinasses. *Environmental Technology (United Kingdom)*, 36 (19), p. 2468-2476.

- MABUZA, J., OTIENO, B., APOLLO, S., MATSHEDISO, B. AND OCHIENG, A. (2017). Investigating the synergy of integrated anaerobic digestion and photodegradation using hybrid photocatalyst for molasses wastewater treatment. *Euro-Mediterranean Journal for Environmental Integration*, 2 (1), p. 17.
- MANTEROLA, G., URIARTE, I. AND SANCHO, L. (2008). The effect of operational parameters of the process of sludge ozonation on the solubilisation of organic and nitrogenous compounds. *Water Research*, 42 (12), p. 3191-3197.
- MANTZAVINOS, D., SAHIBZADA, M., LIVINGSTON, A.G., METCALFE, I.S. AND HELLGARDT, K. (1999). Wastewater treatment: Wet air oxidation as a precursor to biological treatment. *Catalysis Today*, 53 (1), p. 93-106.
- MECHA, ACHISA C., ONYANGO, M.S., OCHIENG, A., FOURIE, C.J.S. AND MOMBA, M.N.B. (2016). Synergistic effect of UV-vis and solar photocatalytic ozonation on the degradation of phenol in municipal wastewater: A comparative study. *Journal of Catalysis*, 341, p. 116-125.
- MECHA, ACHISA C, ONYANGO, M.S., OCHIENG, A. AND MOMBA, M.N.B. (2016). Impact of ozonation in removing organic micro-pollutants in primary and secondary municipal wastewater: Effect of process parameters. *Water Science and Technology*, 74 (3), p. 756-765.
- MELAMANE, X.L., STRONG, P.J. AND BURGESS, J.E. (2007). Treatment of wine distillery wastewater: A review with emphasis on anaerobic membrane reactors. *South African Journal of Enology and Viticulture*, 28 (1), p. 25-36.
- MORAES, B.S., JUNQUEIRA, T.L., PAVANELLO, L.G., CAVALETT, O., MANTELATTO, P.E., BONOMI, A. AND ZAIAT, M. (2014). Anaerobic digestion of vinasse from sugarcane biorefineries in Brazil from energy, environmental, and economic perspectives: Profit or expense? *Applied Energy*, 113, p. 825-835.
- MORAES, B.S., ZAIAT, M. AND BONOMI, A. (2015). Anaerobic digestion of vinasse from sugarcane ethanol production in Brazil: Challenges and perspectives. *Renewable and Sustainable Energy Reviews*, 44, p. 888-903.
- MUNTER, R. (2001). Advanced Oxidation Processes Current Status and Prospect. *Proc. Estonian Acad. Sci. Chem.*, 50 (2), p. 59-80.
- NADDEO, V., BELGIORNO, V., LANDI, M., ZARRA, T. AND NAPOLI, R.M.A. (2009). Effect of sonolysis on waste activated sludge solubilisation and anaerobic biodegradability. *Desalination*, 249 (2), p. 762-767.
- NAIDOO, V. (1999). Municipal wastewater characterization: Application of denitrification batch tests. *PhD Thesis Submitted to the University of Natal*.
- NAVGIRE, M., YELWANDE, A., TAYDE, D., ARBAD, B. AND LANDE, M. (2012). Photodegradation of Molasses by a MoO3-TiO₂ Nanocrystalline Composite Material. *Chinese Journal of Catalysis*, 33 (2-3), p. 261-266.

- NGAMSOPASIRISKUN, C., CHARNSETHIKUL, S., THACHEPAN, S. AND SONGSASEN, A. (2010). Removal of Phenol in Aqueous Solution by Nanocrystalline TiO 2 / Activated Carbon Composite Catalyst. *Natural science*, 1182, p. 1176-1182.
- NOGUEIRA, C.E.C., DE SOUZA, S.N.M., MICUANSKI, V.C. AND AZEVEDO, R.L. (2015). Exploring possibilities of energy insertion from vinasse biogas in the energy matrix of Paraná State, Brazil. *Renewable and Sustainable Energy Reviews*, 48, p. 300-305.
- OCHIENG, A., ODIYO, J.O. AND MUTSAGO, M. (2003). Biological treatment of mixed industrial wastewaters in a fluidised bed reactor. *Journal of Hazardous Materials*, 96 (1), p. 79-90.
- OJIJO, V.O., ONYANGO, M.S. AND OCHIENG, A. (2010). Decolourization of Melanoidin Containing Wastewater Using South African Coal Fly Ash. *International Journal of Chemical, Nuclear, Metturllurgical and Materials Engineering*, 4 (1), p. 1-7.
- OLLER, I., MALATO, S. AND SÁNCHEZ-PÉREZ, J.A. (2011). Combination of Advanced Oxidation Processes and biological treatments for wastewater decontamination—A review. *Science of The Total Environment*, 409 (20), p. 4141-4166.
- OTIENO, B. (2017). Adsorption and Photodegradation of Molasses Wastewater using TiO₂-ZnO Hybrid Nanocatalysts Supported on Activated Carbon and Silica. *Masters Thesis Submitted to Vaal University of Technology*.
- OTIENO, B., APOLLO, S., NAIDOO, B. AND OCHIENG, A. (2016). Photodegradation of Molasses Wastewater Using TiO ₂ -ZnO Nanohybrid Photocatalyst Supported on Activated Carbon. *Chemical Engineering Communications*, 6445 (August), p. 1443-1454.
- OTIENO, B.O., APOLLO, S.O., NAIDOO, B.E. AND OCHIENG, A. (2017). Photodecolorisation of melanoidins in vinasse with illuminated TiO ₂ -ZnO/activated carbon composite. *Journal of Environmental Science and Health, Part A*, 52 (7), p. 1-8.
- PANTHI, G., PARK, M., KIM, H.-Y., LEE, S.-Y. AND PARK, S.-J. (2015). Electrospun ZnO hybrid nanofibers for photodegradation of wastewater containing organic dyes: A review. *Journal of Industrial and Engineering Chemistry*, 21, p. 26-35.
- PEÑA, M., COCA, M., GONZÁLEZ, G., RIOJA, R. AND GARCÍA, M.T. (2003). Chemical oxidation of wastewater from molasses fermentation with ozone. *Chemosphere*, 51 (9), p. 893-900.
- Perrone, O.M., Rossi, J.S., Moretti, M.M. de S., Nunes, C. da C.C., Bordignon, S.E., Gomes, E., Da-Silva, R. and Boscolo, M. (2017). Influence of ozonolysis time during sugarcane pretreatment: Effects on the fiber and enzymatic saccharification. *Bioresource Technology*, 224, p. 733-737.
- PRADHAN, A. AND MBOHWA, C. (2014). Development of biofuels in South Africa: Challenges and opportunities. *Renewable and Sustainable Energy Reviews*, 39, p. 1089-1100.
- QUAN, X., Luo, D., Wu, J., Li, R., Cheng, W. and Ge, Shuping (2017). Ozonation of acid red 18 wastewater using O3/Ca(OH)2 system in a micro bubble gas-liquid reactor. *Journal of Environmental Chemical Engineering*, 5 (1), p. 283-291.

- RAJAGOPAL, V., PARAMJIT, S.M., SURESH, K.P., YOGESWAR, S., NAGESHWAR, R.D.V.K. AND AVINASH, N. (2014). Significance of vinasses waste management in agriculture and environmental quality Review. *African Journal of Agricultural Research*, 9 (38), p. 2862-2873.
- REN, H., MA, L., WANG, B., GONG, H., YUAN, Z. AND LI, Z. (2017). Systematic analysis of the biochemical characteristics of activated sludge during ozonation for lowering of biomass production. *Ozone: Science and Engineering*, 39 (2), p. 80-90.
- SALOMON, K.R., LORA, E.E.S., ROCHA, M.H. AND OLMO, O.A. DEL (2011). Cost calculations for biogas from vinasse biodigestion and its energy utilization. *Zuckerindustrie*, 136 (4), p. 217-223.
- SANGAVE, P.C., GOGATE, P.R. AND PANDIT, A.B. (2007). Combination of ozonation with conventional aerobic oxidation for distillery wastewater treatment. *Chemosphere*, 68 (1), p. 32-41.
- SANTAL, A.R. AND SINGH, N.P. (2013). Biodegradation of Melanoidin from Distillery Effluent: Role of Microbes and Their Potential Enzymes. *Biodegradation of Hazardous and Special Products*.
- SANTOS, D.C., SILVA, L., ALBUQUERQUE, A., SIMÕES, R. AND GOMES, A.C. (2013). Biodegradability enhancement and detoxification of cork processing wastewater molecular size fractions by ozone. *Bioresource Technology*, 147, p. 143-151.
- SATYAWALI, Y. AND BALAKRISHNAN, M. (2008). Wastewater treatment in molasses-based alcohol distilleries for COD and color removal: A review. *Journal of Environmental Management*, 86 (3), p. 481-497.
- SEMBLANTE, G.U., HAI, F.I., DIONYSIOU, D.D., FUKUSHI, K., PRICE, W.E. AND NGHIEM, L.D. (2017). Holistic sludge management through ozonation: A critical review. *Journal of Environmental Management*, 185, p. 79-95.
- SHAO, L., WANG, T., LI, T., LÜ, F. AND HE, P. (2013). Comparison of sludge digestion under aerobic and anaerobic conditions with a focus on the degradation of proteins at mesophilic temperature. *Bioresource Technology*, 140, p. 131-137.
- SHENG, G.P., Yu, H.Q. AND LI, X.Y. (2010). Extracellular polymeric substances (EPS) of microbial aggregates in biological wastewater treatment systems: A review. *Biotechnology Advances*, 28 (6), p. 882-894.
- SHIVAJIRAO, P.A. (2012). Treatment of Distillery Wastewater using Membrane Technologies. *International of Advanced Engineering Research and Studies*, 1 (3), p. 275-283.
- SHIVARAJU, H. (2011). Removal of organic pollutants in the municipal sewage water by TiO₂ based Heterogeneous Photocatalysis. *International Journal of Environmental Sciences*, 1 (5), p. 911-923.
- SHU, Z., BOLTON, J.R., BELOSEVIC, M. AND GAMAL EL DIN, M. (2013). Photodegradation of emerging micropollutants using the medium-pressure UV/H₂O₂ Advanced Oxidation Process. *Water Research*, 47 (8), p. 2881-2889.

- SILES, J.A., MARTÍN, M.A., CHICA, A. AND BORJA, R. (2008). Kinetic modelling of the anaerobic digestion of wastewater derived from the pressing of orange rind produced in orange juice manufacturing. *Chemical Engineering Journal*, 140 (1-3), p. 145-156.
- SILVESTRE, G., RUIZ, B., FITER, M., FERRER, C., BERLANGA, J.G., ALONSO, S. AND CANUT, A. (2015). Ozonation as a pre-treatment for anaerobic digestion of waste-activated sludge: Effect of the ozone doses. *Ozone: Science and Engineering*, 37 (4), p. 316-322.
- SINGH CHAUHAN, M. AND KUMAR DIKSHIT, A. (2012). Decolorization of Anaerobically Digested Molasses Spentwash by Coagulation. *American Journal of Environmental Engineering*, 2 (1), p. 12-18.
- SOSNOWSKI, P., KLEPACZ-SMOLKA, A., KACZOREK, K. AND LEDAKOWICZ, S. (2008). Kinetic investigations of methane co-fermentation of sewage sludge and organic fraction of municipal solid wastes. *Bioresource Technology*, 99 (13), p. 5731-5737.
- SPALDING-FECHER, R. (2011). What is the carbon emission factor for the South African electricity grid? *Journal of Energy in Southern Africa*, 22 (4), p. 8-12.
- TAKASHINA, T.A., LEIFELD, V., ZELINSKI, D.W., MAFRA, M.R. AND IGARASHI-MAFRA, L. (2018). Application of Response Surface Methodology for Coffee Effluent Treatment by Ozone and Combined Ozone/UV. *Ozone: Science and Engineering*, 40 (4), p. 293-304.
- TANG, S., ZHENG, C. AND ZHANG, Z. (2018). Effect of inherent minerals on sewage sludge pyrolysis: Product characteristics, kinetics and thermodynamics. *Waste Management*, 80, p. 175-185.
- TANG, Y.-Q., FUJIMURA, Y., SHIGEMATSU, T., MORIMURA, S. AND KIDA, K. (2007). Anaerobic treatment performance and microbial population of thermophilic upflow anaerobic filter reactor treating awamori distillery wastewater. *Journal of Bioscience and Bioengineering*, 104 (4), p. 281-287.
- TITOUHI, H. AND BELGAIED, J.E. (2016). Heterogeneous Fenton oxidation of ofloxacin drug by iron alginate support. *Environmental Technology (United Kingdom)*, 37 (16), p. 2003-2015.
- TOCZYŁOWSKA-MAMIŃSKA, R. (2017). Limits and perspectives of pulp and paper industry wastewater treatment A review. *Renewable and Sustainable Energy Reviews*, 78 (November 2016), p. 764-772.
- Travaini, R., Martin-Juarez, J., Lorenzo-Hernando, A. and Bolado-Rodriguez, S. (2016). Ozonolysis: An advantageous pretreatment for lignocellulosic biomass revisited. *Bioresource Technology*, 199, p. 2-12.
- VAN ZYL, P.J., WENTZEL, M.C., EKAMA, G.A. AND RIEDEL, K.J. (2008). Design and start-up of a high rate anaerobic membrane bioreactor for the treatment of a low pH, high strength, dissolved organic waste water. *Water Science and Technology*, 57 (2), p. 291-295.
- VAVILIN, V.A. (2010). Anaerobic degradation of organic waste: An experience in mathematical modeling. *Microbiology*, 79 (3), p. 334-341.

- VENKATESH, S., QUAFF, A.R., PANDEY, N.D. AND VENKATESH, K. (2015). Impact of Ozonation on Decolorization and Mineralization of Azo Dyes: Biodegradability Enhancement, By-Products Formation, Required Energy and Cost. *Ozone: Science & Engineering*, 37 (5), p. 420-430.
- WAN OMAR, W.N.N. AND AMIN, N.A.S. (2016). Multi response optimization of oil palm frond pretreatment by ozonolysis. *Industrial Crops and Products*, 85, p. 389-402.
- WANG, Q., WEI, W., GONG, Y., YU, Q., LI, Q., SUN, J. AND YUAN, Z. (2017). Technologies for reducing sludge production in wastewater treatment plants: State of the art. *Science of the Total Environment*, 587-588, p. 510-521.
- WARDHANI, P.K. (2017). Mathematical and Experimental Study of Anaerobic Digestion Process and Biogas Generation from Fruit and Vegetable Waste Puteri Kusuma Wardhani Graduate School of Environmental and Life Science (Doctor's Course). *PhD Thesis Submitted to Okayama University*.
- WEI, Z.S., LI, H.Q., HE, J.C., YE, Q.H., HUANG, Q.R. AND LUO, Y.W. (2013). Removal of dimethyl sulfide by the combination of non-thermal plasma and biological process. *Bioresource Technology*, 146, p. 451-456.
- WESTERHOFF, P., DEBROUX, J., AIKEN, G. AND AMY, G. (1999). Ozone-induced changes in natural organic matter (NOM) structure. *Ozone: Science and Engineering*, 21 (6), p. 551-570.
- XIAO, B., LIU, C., LIU, J. AND GUO, X. (2015). Evaluation of the microbial cell structure damages in alkaline pretreatment of waste activated sludge. *Bioresource Technology*, 196, p. 109-115.
- YAN, S.T., CHU, L.B., XING, X.H., YU, A.F., SUN, X.L. AND JURCIK, B. (2009). Analysis of the mechanism of sludge ozonation by a combination of biological and chemical approaches. *Water Research*, 43 (1), p. 195-203.
- YANG, G. AND ANDERSON, G.K. (1992). Determination of bicarbonate and total volatile acid concentration in anaerobic digesters using a simple titration. *Water Environment Research*, 64 (1), p. 53-59.
- YASAR, A., ALI, A., TABINDA, A.B. AND TAHIR, A. (2015a). Waste to energy analysis of shakarganj sugar mills; Biogas production from the spent wash for electricity generation. *Renewable and Sustainable Energy Reviews*, 43, p. 126-132.
- YASAR, A., ALI, A., TABINDA, A.B. AND TAHIR, A. (2015b). Waste to energy analysis of shakarganj sugar mills; Biogas production from the spent wash for electricity generation. *Renewable and Sustainable Energy Reviews*, 43, p. 126-132.
- YETILMEZSOY, K. (2012). Integration of kinetic modeling and desirability function approach for multi-objective optimization of UASB reactor treating poultry manure wastewater. *Bioresource Technology*, 118, p. 89-101.

- YUAN, H., YU, B., CHENG, P., ZHU, N., YIN, C. AND YING, L. (2016). Pilot-scale study of enhanced anaerobic digestion of waste activated sludge by electrochemical and sodium hypochlorite combination pretreatment. *International Biodeterioration and Biodegradation*, 110, p. 227-234.
- ZHANG, S., GUO, H., DU, L., LIANG, J., LU, X., LI, N. AND ZHANG, K. (2015). Influence of NaOH and thermal pretreatment on dewatered activated sludge solubilisation and subsequent anaerobic digestion: Focused on high-solid state. *Bioresource Technology*, 185, p. 171-177.
- ZHANG, Y., Hu, R., TIAN, J. AND LI, T. (2018). Disintegration of waste activated sludge with composite ferrate solution: Sludge reduction and settleability. *Bioresource Technology*, 267, p. 126-132.
- ZHEN, G., LU, X., KATO, H., ZHAO, Y. AND LI, Y.-Y.Y. (2017). Overview of pretreatment strategies for enhancing sewage sludge disintegration and subsequent anaerobic digestion: Current advances, full-scale application and future perspectives. *Renewable and Sustainable Energy Reviews*, 69, p. 559-577.
- ZHOU, Y., ZHENG, H., GAO, B., GU, Y., LI, X., LIU, B. AND JIMÉNEZ, A.M. (2017). Waste activated sludge (WAS) dewatering properties of an original hydrophobically modified polyacrylamide containing a cationic microblock structure. *RSC Advances*, 7 (46), p. 28733-28745.
- ZINATIZADEH, A.A., MIRGHORAYSHI, M., BIRGANI, P.M., MOHAMMADI, P. AND IBRAHIM, S. (2017). Influence of thermal and chemical pretreatment on structural stability of granular sludge for high-rate hydrogen production in an UASB bioreactor. *International Journal of Hydrogen Energy*, 42 (32), p. 20512-20519.
- ZOU, J., ZHANG, L., WANG, L. AND LI, Y. (2017). Enhancing phosphorus release from waste activated sludge containing ferric or aluminum phosphates by EDTA addition during anaerobic fermentation process. *Chemosphere*, 171, p. 601-608.

APPENDICES

Appendix A: Anaerobic reaction kinetic models

To investigate the kinetics of AD, microbial growth, substrate degradation, and product formation should be taken into consideration. At steady-state biodegradation of wastewaters, it can be supposed that the suspended solids (SS) contained in the effluent corresponds to generated biomass. Thus, a mass balance based on the feed concentration can be given by (Borja et al., 2002);

$$S_o = S + S_g + S_{ss} + S_m \tag{8.1}$$

where, S_o and S are the influent and effluent substrate concentration (COD), respectively. S_g , S_{ss} , S_m are the fractions of the influent COD converted to biogas and suspended solids, and used for cell maintenance, respectively. Various kinetics models can be used to predict substrate removal, biomass formation, and biogas production.

Kinetics of substrate removal; First-order model

The kinetics of anaerobic reactors can be simulated by the first order substrate removal model given by (Ibrahim, 2014; Ebrahimi et al., 2018);

$$-\frac{dS}{dt} = \frac{QS_o}{V} - \frac{QS}{V} - k_1 S \tag{8.2}$$

where, k_1 , Q and V are the substrate removal rate constant (hr⁻¹), the inflow rate (L/hr), and the volume of the reactor (L). Since at steady-state (-dS/dt) is negligible, Eq. 8.2 can be expressed as;

$$\frac{S_o - S}{t} = k_1 S \tag{8.3}$$

where, t is the retention time (hrs), and S is the substrate concentration at time t. The substrate removal constant can be obtained from a plot of $S_o - S$ vs t. The first-order model is easy to handle but has limited accuracy to confined requirements. Moreover, models based on the first-order cannot predict the optimum conditions required for maximum biological activity (Kythreotou et al., 2014). Models based on bacterial growth are thus important for adequate modelling of anaerobic processes.

Kinetics of biomass formation; Monod and Contois models

The substrate consumption or product formation can be used to determine the biomass growth kinetics. Using the substrate balance and growth kinetics, a mathematical model can be developed to describe substrate reduction with time. The substrate balance is given by;

$$\frac{dS}{dt} = -Y_{xs}\mu X \tag{8.4}$$

where, Y_{xs} , μ and X are the yield coefficient (g/g), specific growth rate (hr⁻¹) and, the biomass concentration (g/L). At a constant biomass yield coefficient, the biomass concentration is calculated by;

$$X = X_o + Y_{xs}(S_o - S_e) (8.5)$$

The Monod model describes a non-linear relationship between substrate concentration and the specific growth rate based on the Michaelis-Menten equation. The model proposes that specific microbial growth rate is inversely proportional to the concentration of substrate. The microbial growth can be formulated by the Monod equation (Ibrahim, 2014);

$$\mu = \mu_{max} \frac{s}{K_s + s} \tag{8.6}$$

where, K_s is the Monod-constant, μ_{max} is the specific growth rate at saturation. The maximum specific bacterial growth rate is described by the Monod-constant. At a higher substrate concentration greater than K_s , the specific growth rate is nearly linear, and K_s is greater than zero. Therefore, $\frac{S}{K_s+S}$ becomes less than one, and μ_{max} is greater than the specific growth rate.

The Monod model has high accuracy when applied to homogeneous pure culture and simple substrates. However, for heterogeneous complex substrates such as municipal wastes, the model has been found unsuitable (Kythreotou et al., 2014). This has led to the development of more kinetic models such as the Contois model, which can adequately describe the anaerobic degradation of complex substrates. Apart from the Monod model, the specific growth and the rate-limiting substrate concentration can be related by the Contois equation given by;

$$\mu = \frac{\mu_{max}S}{BX+S} \tag{8.7}$$

where, B is the kinetic parameter (g COD/g biomass).

Kinetics of biogas production; Modified Gompertz equation

The cumulative biogas production during anaerobic digestion is widely described by the modified Gompertz equation. The equation assumes that the biogas production rate by the methanogens corresponds to the specific growth rate. The equation is given by;

$$B_t = B_p exp \left\{ -exp \left[\frac{R_b e}{B_p} (\lambda - t) + 1 \right] \right\}$$
 (8.8)

where, B_t , B_p , R_b and λ are the cumulative biogas produced (L) at a given time, biogas production potential (L), maximum biogas production rate (L/hr), and the lag phase (hrs). The lag phase is the duration taken before biogas production starts after feeding.

Appendix B: Photocatalytic and ozonolysis reaction processes

The essential photocatalytic process is given by;

$$MO + hv \rightarrow MO (e^{-} + h^{+})$$
(8.9)

where MO is the metal oxide semiconductor (TiO₂ or ZnO). The photogenerated electrons lead to the formation of ${}^{\bullet}O_2$, H_2O_2 , and ${}^{\bullet}HO_2$, as shown in Eq. 8.10 to 8.17.

$$MO(e^{-}) + O_{2} \rightarrow MO + {}^{\bullet}O_{2}^{-}$$
 (8.10)

$$MO(e^{-}) + {}^{\bullet}O_{2} - +2H^{+} \rightarrow MO + H_{2}O_{2}$$
 (8.11)

$$MO (e^{-}) + H_2O_2 \rightarrow MO + {}^{\bullet}OH + OH^{-}$$
 (8.12)

$${}^{\bullet}\text{O}_2^- + \text{H}_2\text{O}_2 \rightarrow {}^{\bullet}\text{OH} + \text{OH}^- + \text{O}_2$$
 (8.13)

$${}^{\bullet}\mathrm{O}_{2}^{-} + \mathrm{H}^{+} \rightarrow {}^{\bullet}\mathrm{O}_{2}\mathrm{H}$$
 (8.14)

$$MO (e^{-}) + {}^{\bullet}O_{2}H \rightarrow MO + HO_{2}^{-}$$
 (8.15)

$$HO_2^- + H^+ \to H_2O_2$$
 (8.16)

$$2^{\bullet}O_2H \rightarrow O_2 + H_2O_2$$
 (8.17)

The excited electrons can react with oxygen molecules forming superoxide radicals $(O_2^{\bullet-})$, which further react with H⁺ providing more hydroxyl radicals (Ngamsopasiriskun et al., 2010). Eq. 8.18 and Eq. 8.19 give the oxidation reactions activated by the photogenerated holes.

$$MO (h^{+}) + H_{2}O \rightarrow MO + {}^{\bullet}OH + H^{+}$$
 (8.18)

$$MO (h^{+}) + H_{2}O \rightarrow MO + {}^{\bullet}OH + H^{+}$$
 (8.19)

$$MO(h^+) + OH^- \rightarrow MO + {}^{\bullet}OH$$
 (8.20)

The reactions are terminated as follows (Baruah et al., 2012):

$$^{\bullet}$$
OH + H⁺ + 2e⁻ → H₂O (8.21)

$$\frac{1}{2}O_2 + 2H^+ + 2e^- \to H_2O$$
 (8.22)

Ozone is an effective chemical oxidant which easily reacts with several multiple bonds containing (C=N, C=C, N=N) organic compounds/species, but not with single bonds (O-H, C-C, C-O) containing species (Bar Oz et al., 2018; Peña et al., 2003; Travaini et al., 2016). Degradation of organic compounds in water by ozone occurs via two routes and is dependent on the medium pH. The first, which mostly occurs under acidic conditions, involves direct oxidation by my molecular O₃ involving selective reactions such as nucleophilic, electrophilic, or dipolar addition reactions, but with low reaction rates (Achisa et al., 2016).

In the second route, which occurs mainly under basic pH conditions, ozone decomposes, producing the non-selective and highly reactive hydroxyl radicals in several reaction steps. Firstly, according to Eq. 8.23 (Munter, 2001), ozone is decomposed by hydroxide ions forming hydroperoxyl (HO₂•) and superoxide (O₂•) radicals. The O₂• radicals react with O₃ forming ozonide anion (O₃•) radicals, as depicted in Eq. 2.31. The ozonide radicals immediately decompose to form OH• radicals and oxygen (O₂) according to Eq. 8.25, via hydrogen trioxide. The hydroxyl radicals react with ozone forming hydroperoxyl radicals (HO₃•), thereby terminating the chain reaction and initiating a new one. Overall, three ozone molecules can theoretically produce two hydroxyl radicals (Achisa et al., 2016).

$$O_3 + OH^- \rightarrow O_2^{\bullet} + HO_2^{\bullet}$$
(8.23)

$$HO_2^{\bullet} \leftrightarrow O_2^{\bullet^-} + H^+$$
 (8.24)

$$O_3 + O_2^{\bullet -} \rightarrow O_3^{\bullet -} + H^+ \leftrightarrow HO_3^{\bullet}$$
(8.25)

$$HO_3^{\bullet} \rightarrow OH^{\bullet} + O_2$$
 (8.26)

Overall;

$$3O_{3+}OH^{-}+H^{+} \rightarrow 2OH^{\bullet}+4O_{2}$$
 (8.27)

Appendix C: CFD modelling

The continuity equation is given as:

$$\frac{\partial}{\partial t}(\alpha_k \rho_k) + \nabla(\alpha_k \rho_k u_k) = 0 \tag{8.28}$$

where α_k , ρ_k and \boldsymbol{u}_k refer to the volume fraction, density, and velocity of phase k.

The momentum equation for the bubble column reactor is given as:

$$\frac{\partial}{\partial t}(\alpha_k \rho_k u_k) + \nabla(\alpha_k \rho_k u_k u_k + \alpha_k \tau_k) = -\nabla(\alpha_k \tau_k) - \alpha_k \nabla P + \alpha_k \rho_k g + F_{l,g}$$
(8.29)

The terms on the right-hand side of the momentum equation describe the viscosity, pressure, gravity, and interfacial forces acting on phase k.

For the fluidized bed reactor, the momentum equation included an additional term for the solid pressure:

$$\frac{\partial}{\partial t}(\alpha_k \rho_k u_k) + \nabla(\alpha_k \rho_k u_k u_k + \alpha_k \tau_k) = -\nabla(\alpha_k \tau_k) - \alpha_k \nabla P - \nabla P_s + \alpha_k \rho_k g + F_{l,s}$$
(8.30)

The sum of the volume fractions of the phases equal to unity:

$$\sum_{k=g,l} \alpha_k = 1 \tag{8.31}$$

Turbulence

Fluid turbulence consists of a mean and fluctuating part of the flow. The mean flow, which is usually important, can be obtained by averaging the Navier-Stokes equations to give Reynolds-averaged Navier-Stokes (RANS) equations. In order to solve the RANS equations, the components of velocity fluctuations, known as the Reynolds stress, must be determined as a function of the mean flow. One attempt at this, the Boussinesq eddy viscosity concept, hypothesizes that Reynolds stresses can be expressed as a function of the mean strain rate. The resulting eddy viscosity model can be expressed as:

$$\tau_k = -\mu_{eff,k} \left(\nabla u_k + (\nabla u_k)^T - \frac{2}{3} I(\nabla u_k) \right)$$
(8.32)

where τ_k is the stress tensor and $\mu_{eff,k}$ is the effective viscosity. The effective viscosity of the liquid phase $(\mu_{eff,L})$ consists of molecular viscosity $(\mu_{I,L})$, shear induced turbulent viscosity $(\mu_{L,L})$ and a term due to bubble induced turbulence $(\mu_{BIT,L})$:

$$\mu_{eff,L} = \mu_{I,L} + \mu_{t,L} + \mu_{BIT,L} \tag{8.33}$$

The effective gas viscosity was calculated from the effective liquid viscosity as:

$$\mu_{eff,G} = \frac{\rho_G}{\rho_L} \mu_{eff,L} \tag{8.34}$$

Similarly, the effective solid viscosity was calculated as:

$$\mu_{eff,S} = \frac{\rho_S}{\rho_I} \mu_{eff,L} \tag{8.35}$$

The bubble induced turbulence ($\mu_{BIT,L}$), was calculated using the model of Sato and Sekoguchi (1975):

$$\mu_{BIT,L} = \rho_L C_{\mu,BIT} \alpha_G d_b |u_G - u_L| \tag{8.36}$$

where d_b is the bubble diameter and the model constant $C_{\mu,BIT}$ was 0.6.

Several models such as the standard k- ϵ , renormalization group (RNG), k- ϵ and Reynolds Stress Model (RSM) have been proposed for computing the liquid phase shear induced turbulent viscosity ($\mu_{t,L}$).

The standard k- ε and RNG k- ε models calculate the $\mu_{t,L}$ as:

$$\mu_{t,L} = \rho_L C_\mu \frac{k^2}{\varepsilon} \tag{8.37}$$

For the standard k- ε model, the turbulent kinetic energy (k) and the turbulent dissipation rate (ε) are calculated using differential transport equations:

$$\frac{\partial}{\partial t}(\alpha_L \rho_L k) + \nabla(\alpha_L \rho_L k u_L) = -\nabla \left(\alpha_L \left(\frac{\mu_{eff,L}}{\sigma_k}\right) \nabla k\right) + \alpha_L (G - \rho_L \varepsilon)$$
(8.38)

$$\frac{\partial}{\partial t}(\alpha_L \rho_L k) + \nabla(\alpha_L \rho_L k u_L) = -\nabla \left(\alpha_L \left(\frac{\mu_{eff,L}}{\sigma_{\varepsilon}}\right) \nabla \varepsilon\right) + \alpha_L \frac{\varepsilon}{k} (C_{\varepsilon 1} G - C_{\varepsilon 2} \rho_L \varepsilon)$$
(8.39)

where the model constants are $C_{\mu}=0.09,\,\sigma_{k}=1.00,\,\sigma_{\varepsilon}=1.00,\,C_{\varepsilon 1}=1.44,\,C_{\varepsilon 2}=1.92$

For the RNG k- ε model, different scales of motion are considered by making the $C_{\varepsilon 2}$ term a function of the local strain rate. The differential equation for k was calculated using equation (3.9) while that for ε was calculated as:

$$\frac{\partial}{\partial t}(\alpha_L \rho_L k) + \nabla(\alpha_L \rho_L k u_L) = -\nabla \left(\alpha_L \left(\frac{\mu_{eff,L}}{\sigma_{\varepsilon RNG}}\right) \nabla \varepsilon\right) + \alpha_L \frac{\varepsilon}{k} (C_{\varepsilon 1RNG} G - C_{\varepsilon 2RNG} \rho_L \varepsilon)$$
(8.40)

where

$$C_{\varepsilon 1RNG} = 1.42 - f_{\eta} \tag{8.41}$$

and

$$f_{\eta} = \frac{\eta(1 - \eta/4.38)}{(1 + \beta_{RNG}\eta^3)} \tag{8.42}$$

Eddy viscosity models depend on the assumption of isotropic turbulence. This assumption can be valid for some flows; however, inflows with high degrees of anisotropy, strong streamline curvature, recirculating flow, and rotational effects, k- ε based models have been observed to be inaccurate. In order to address this, the RSM model was developed in which the individual Reynolds stresses ($\overline{u_i'u_j'}$) are calculated using differential transport equations. This provides the most accurate solution to the Reynolds stresses. However, this good accuracy comes with a high computational cost. Six Reynolds stress differential equations (equation 3.16) are solved along with a dissipation rate equation (equation 3.17).

$$\frac{\partial}{\partial t} \left(\alpha_L \rho_L \overline{u_i' u_j'} \right) + \frac{\partial}{\partial x_k} \left(\alpha_L \rho_L u_k \overline{u_i' u_j'} \right) \\
= \alpha_L P_{ij}' + \alpha_L \phi_{ij} + \frac{\partial}{\partial x_k} \left(\alpha_L \left(\mu_L + \frac{2}{3} C_s' \rho \frac{k^2}{\varepsilon} \right) \frac{\partial \overline{u_i' u_j'}}{\partial x_k} \right) - \frac{2}{3} \delta_{ij} \alpha_L \rho_L \varepsilon \tag{8.43}$$

$$\frac{\partial}{\partial t} (\alpha_{L} \rho_{L} \varepsilon) + \frac{\partial}{\partial x_{k}} (\alpha_{L} \rho_{L} \varepsilon u_{i})$$

$$= \frac{\partial}{\partial x_{i}} \left(\alpha_{L} \left(\mu_{L} + \frac{\mu_{t,L}}{\sigma_{\varepsilon}} \right) \frac{\partial \varepsilon}{\partial x_{i}} \right) + \alpha_{L} \rho_{L} C_{\varepsilon 1} \left(\overline{u'_{i} u'_{k}} \frac{\partial u_{i}}{\partial x_{k}} \right) \frac{\varepsilon}{k} - \alpha_{L} \rho_{L} C_{\varepsilon 2} \frac{\varepsilon^{2}}{k} \tag{8.44}$$

Gas-liquid interfacial forces

The gas-liquid interfacial forces ($F_{l,g}$) are due to drag, lift, wall lubrication and turbulent dispersion forces:

$$F_{l,g} = F_D + F_L + F_{WL} + F_{TD} (8.45)$$

A bubble rising through a fluid experiences resistance due to drag force which is given by:

$$F_D = \frac{3}{4} C_{D,GL} \alpha_G \rho_L \frac{1}{d_h} |u_G - u_L| (u_G - u_L)$$
 (8.46)

The drag coefficient ($C_{D,ls}$) which accounts for the character of the flow around the bubble was determined using the Ishii and Zuber (1979) model, which accounts for spherical, elliptical and cap regimes:

$$C_{D,GL} = \frac{2}{3}E_o^{0.5} \tag{8.47}$$

where E_o Eotvos number was calculated using equation (3.26). The drag model by Ishii and Zuber (1979) has been used successfully by Ekambara et al. (2010) to simulate a similar bubble column. Masood and Delgado (2014) also found the drag model to be accurate for the square bubble column reactor.

A rising bubble also experiences a lift force acting perpendicular to the direction of flow:

$$F_L = C_L \alpha_G \rho_L (u_G - u_L) \times \nabla \times u_L \tag{8.48}$$

The lift coefficient (C_L) was determined using the model by Tomiyama et al. (2002) as (Ansys, 2017):

$$C_{L} = \begin{cases} \min[0.288 \tanh(0.121 \text{Re}_{b}), f(E'_{o})], & E'_{o} < 4 \\ f(E'_{o}), & 4 < E'_{o} \le 10 \\ -0.27, & 10 < E'_{o} \end{cases}$$
(8.49)

where

$$f(E_0') = 0.00105(E_0')^3 - 0.0159(E_0')^2 - 0.0204E_0' + 0.474$$
(8.50)

and E'_{o} is the modified Eotvos number based on d_{H} , the long axis of the deformable bubble:

$$E_o' = \frac{g\Delta\rho d_H^2}{\sigma} \tag{8.51}$$

$$d_H = d_b (1 + 0.163 E_o^{0.757})^{1/3}$$
(8.52)

$$E_o = \frac{g\Delta\rho d_b^2}{\sigma} \tag{8.53}$$

where $\Delta \rho$ is the density difference between gas and liquid.

Due to the difference in liquid flow rate between the wall and in the middle of the reactor, bubbles experience a wall lubrication force that pushes them away from the wall. This effect has been modelled by Tomiyama (2002) as:

$$F_{WL} = C_{WL} \frac{d_b}{2} \left(\frac{1}{y_W^2} - \frac{1}{(D - y_W)^2} \right)$$
 (8.54)

where D is the reactor diameter, y_W is the distance to the nearest wall and C_{WL} is a coefficient which depends on Eotvos number (E_o) . C_{WL} is presented in modified form as (Ansys, 2017):

$$C_{WL} = \begin{cases} 0.47 & E_o < 1 \\ \exp(-0.933E_o + 0.179) & 1 \le E_o \le 5 \\ 0.00599E_o + 0.0187 & 5 \le E_o \le 33 \\ 0.179 & 33 < E_o \end{cases}$$
 (8.55)

The turbulent dispersion force arises from the turbulent diffusion of the bubbles by liquid eddies. It has been formulated by Lopez de Bertonado as (de Bertodano, 1992):

$$F_{TD} = -C_{TD}\rho_L k \nabla \alpha_L \tag{8.56}$$

where k is the turbulent kinetic energy and the turbulent dispersion coefficient (C_{TD}) was specified as 0.3, as suggested by Ekambara et al. (2010).

Liquid-solid interfacial forces

For the fluidized bed reactor, in addition to the gas-liquid interfacial forces, the liquid-solid interfacial drag force was modelled as:

$$F_D = \frac{3}{4} C_{D,LS} \alpha_S \rho_L \frac{1}{d_S} |u_S - u_L| (u_S - u_L)$$
(8.57)

The drag coefficient ($C_{D,LS}$) was modelled using the Schiller Naumann drag model as:

$$C_{D,LS} = \max \left[\frac{24}{\text{Re}} (1 + 0.15 \text{Re}^{0.687}), 0.44 \right]$$
 (8.58)

where

$$Re = \frac{\rho_L d_S |u_S - u_L|}{\mu_L}$$
(8.59)

Appendix D: Effect of turbulence CFD models

Axial liquid velocity

The axial liquid velocity is an important hydrodynamic parameter as it gives an indication of mixing efficiency and dead zones in the reactor. The effect of different turbulent models on the axial liquid velocity radial profiles at different axial locations was investigated. The time-averaged liquid velocity vectors (Figure 8.1a-c) show a well-established flow pattern in which liquid flows upwards in the middle of the reactor and downwards near the reactor wall. This is further clarified by the radial axial liquid velocity profiles (Figure 8.2). The upward flow of liquid was highest in the middle of the reactor reducing in the radial direction towards the wall. At a normalized radial location of roughly 0.7, the axial liquid velocity reduced to zero, followed by a reversal in the flow direction downward before rising back to zero at the wall. This kind of flow pattern is typical of a bubble column reactor as indicated by Kulkarni et al. (2007). Furthermore, as observed in the liquid velocity vectors and experimental radial axial liquid velocity profiles, the centreline axial liquid velocity increases with the height of the distributor. This is due to the migration of bubbles towards the centre of the column with an increase in height which results in an increase in the gas holdup and liquid velocity.

The experimental axial liquid velocity radial profiles at different axial locations were compared to those obtained using different turbulent models. The typical axial liquid velocity radial profiles were captured by the CFD simulation. At an axial location of h/H=0.03, near the distributor, a poor agreement between the simulation and experimental profiles was observed for all the turbulent models. The prediction improved higher up in the column between h/H=0.39 and h/H=0.75, although all the turbulent models underpredicted the centreline axial velocity profiles. The RSM model showed the best prediction of the centreline axial liquid velocity while the standard k-smodel gave the worst prediction, with the RNG k-s model giving an intermediate prediction. This is also evident from the liquid velocity vectors which show high centreline liquid velocity using the RSM model followed by the RNG k-s model with the standard k-s model with the lowest values. This was attributed to the better accuracy of the RSM model in modelling the turbulence parameters. The RNG k-s turbulence model showed a better prediction than the standard model due to a correction in the turbulence dissipation rate.

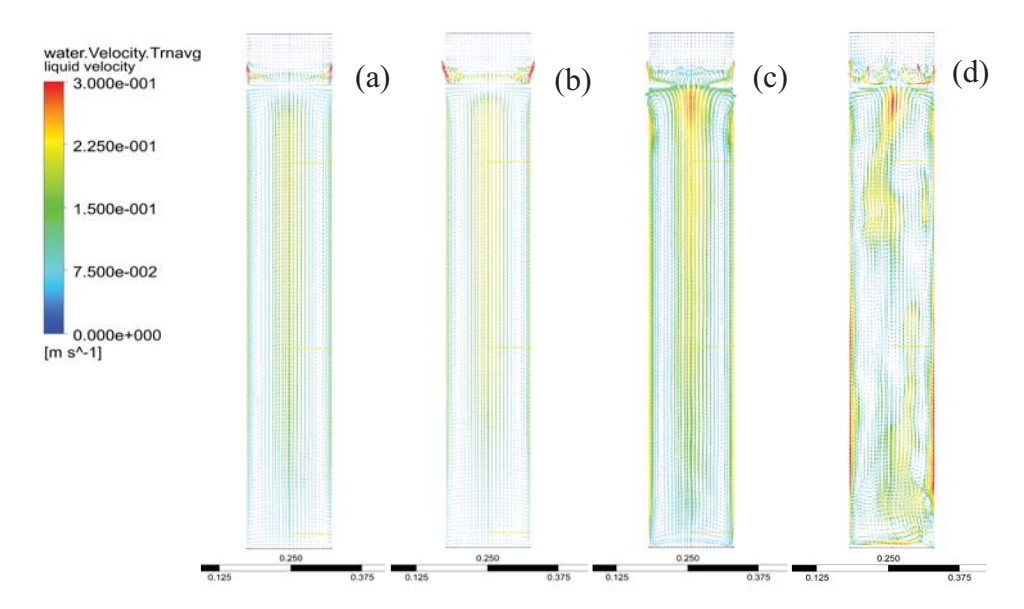


Figure 8.1: Liquid velocity vectors using different turbulence models (a) Standard k-ε (average), (b) RNG k-ε (average), RSM model (average), RSM model (transient).

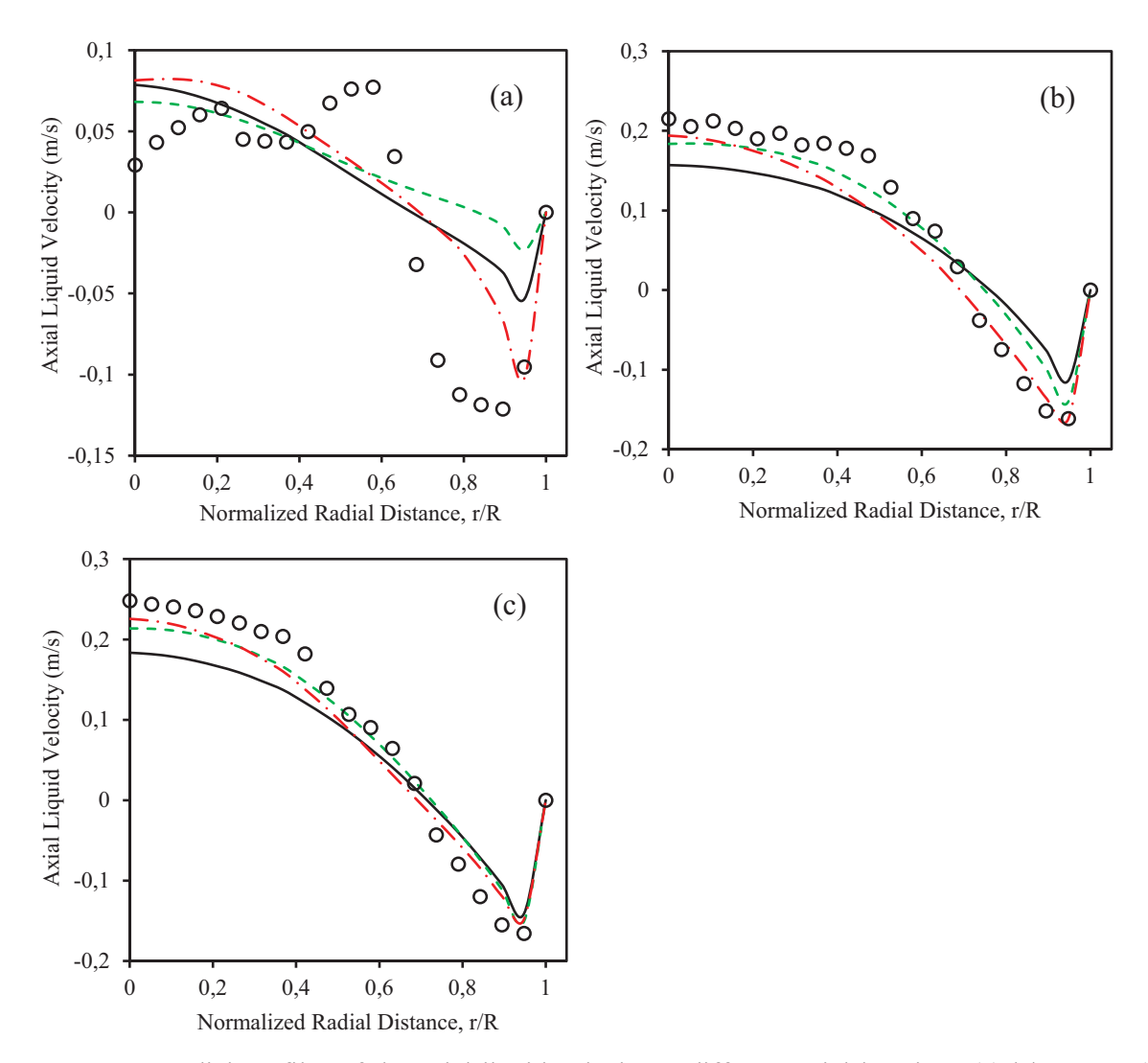


Figure 8.2: Radial profiles of the axial liquid velocity at different axial locations (a) h/H=0.03, (b) h/H=0.39, (c) h/H=0.75 (\circ) experimental, (\longrightarrow) Standard k- ε , (- - -) RNG k- ε and (\frown -) RSM models.

With an increase in the distance from the distributor, bubbles tend to move towards the centre of the column resulting in an increase in the centreline axial liquid velocity at higher column levels (Kulkarni et al., 2007). The fact that all the turbulent models underpredicted the centreline axial liquid velocity higher up in the column can be attributed to the inaccuracy of the model, which only considered a single bubble size. Significant bubble coalescence is expected in the centreline, and this would result in an increase in the bubble size. The larger bubbles would rise faster in the liquid resulting in a higher axial liquid velocity. The use of bubble coalescence and break up models would have captured this phenomenon more accurately.

Gas holdup

The effect of different turbulent models (Standard k-ε, RNG k-ε, and RSM models) on the radial gas holdup at different axial locations was investigated. Radial gas holdup profiles were observed to decrease from the middle of the reactor towards the wall (Figure 8.3a-c). This is so since, in a bubble column, the bubbles tend to move away from the wall and accumulate in the middle of the column. In the region near the distributor, this effect is not very pronounced, consequently, the gas holdup radial profile appears flat. Further up the column, the gas bubbles start to move towards the centre of the column resulting in a parabolic shape when the flow is fully developed (Kulkarni et al., 2007). The flat profile near the distributor (h/H=0.03) was poorly captured by the different turbulent models. However, the fully developed profile between the axial location of h/H=0.39 and h/H=0.75 was captured fairly well especially near the centreline and wall.

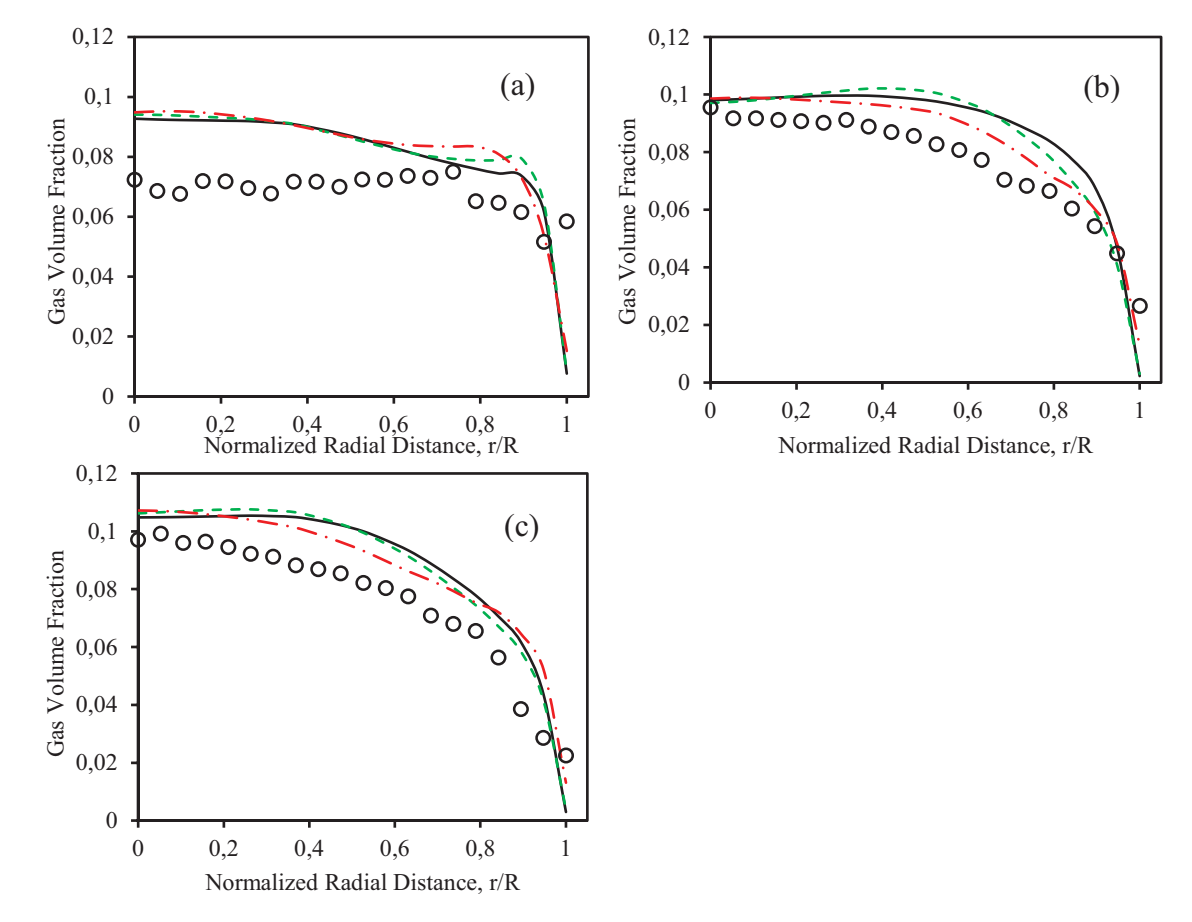


Figure 8.3: Radial profiles of the gas holdup at different axial locations (a) h/H=0.03, (b) h/H=0.39, (c) h/H=0.75 (\circ) experimental, (\longrightarrow) Standard k- ε , (- - -) RNG k- ε and (\longrightarrow - -) RSM models

The different turbulent models resulted in the same degree of prediction accuracy near the column centre and near the wall. However, at the intermediate radial location near the point of flow reversal, all the turbulent models overpredicted the gas holdup. Generally, the RSM

model was more accurate, followed by the RNG k-ε with the standard k-ε model showing the least accurate prediction. The higher accuracy of the RSM model was since it modelled all the six Reynolds stresses. The RNG k-ε model was found to be more accurate than the standard k-ε model, and this can be attributed to the fact that the RNG k-ε model could account for different turbulence scales while the standard k-ε model considers only one turbulence length scale (Masood and Delgado, 2014). The more accurate turbulence models were found to be better at predicting gas holdup. This can be attributed to the dependence of turbulent dispersion force on the turbulent kinetic energy. Therefore, accurate turbulence models resulted in a more accurate prediction of the dispersion of bubbles by liquid eddies and thus the radial gas holdup profiles.

Turbulent kinetic energy

Turbulent kinetic energy gives an indication of the intensity of turbulence at different locations in the reactor. This, in turn, can give valuable insight into the degree of mixing. The effect of different turbulent models on the radial turbulent kinetic energy profiles at different axial locations was investigated (Figure 8.4). The turbulent kinetic energy increases with an increase in the axial distance from the distributor. This is due to an increase in the gas velocity with height, which can be attributed to the increase in bubble size as a result of the decreasing hydrostatic pressure and bubble coalescence. The larger sized bubbles rise faster since they experience less drag due to their low surface to volume ratio. At the region near the distributor (h/H=0.03), the radial turbulent kinetic energy profile is relatively flat due to a uniform gas holdup profile. At this region, a significant difference in the prediction using the different turbulent models was observed. At this region of high anisotropy, only the RSM model provided accurate simulation. The 2-equation k-ε models overpredicted the turbulent kinetic energy since these models were developed under the assumption of isotropic flow. Higher up the column, where the flow is well developed, gas holdup increases near the centreline, resulting in high turbulent kinetic energy at the centre of the column. A second high turbulence kinetic energy zone is observed at the point of flow reversal which drops drastically near the wall. The high turbulent kinetic energy at the point of flow reversal has been attributed to the large gradients and fluctuations in the liquid velocity (Ekambara et al., 2008). Simulation using the different turbulent models managed to capture the high turbulent kinetic energy at the point of flow reversal and the reduction at the wall; however, all the models underpredicted the high turbulent kinetic energy at the centreline. This could be attributed to the low axial liquid

velocity predicted by the turbulence models which could be due to inaccurate prediction of the interfacial forces.

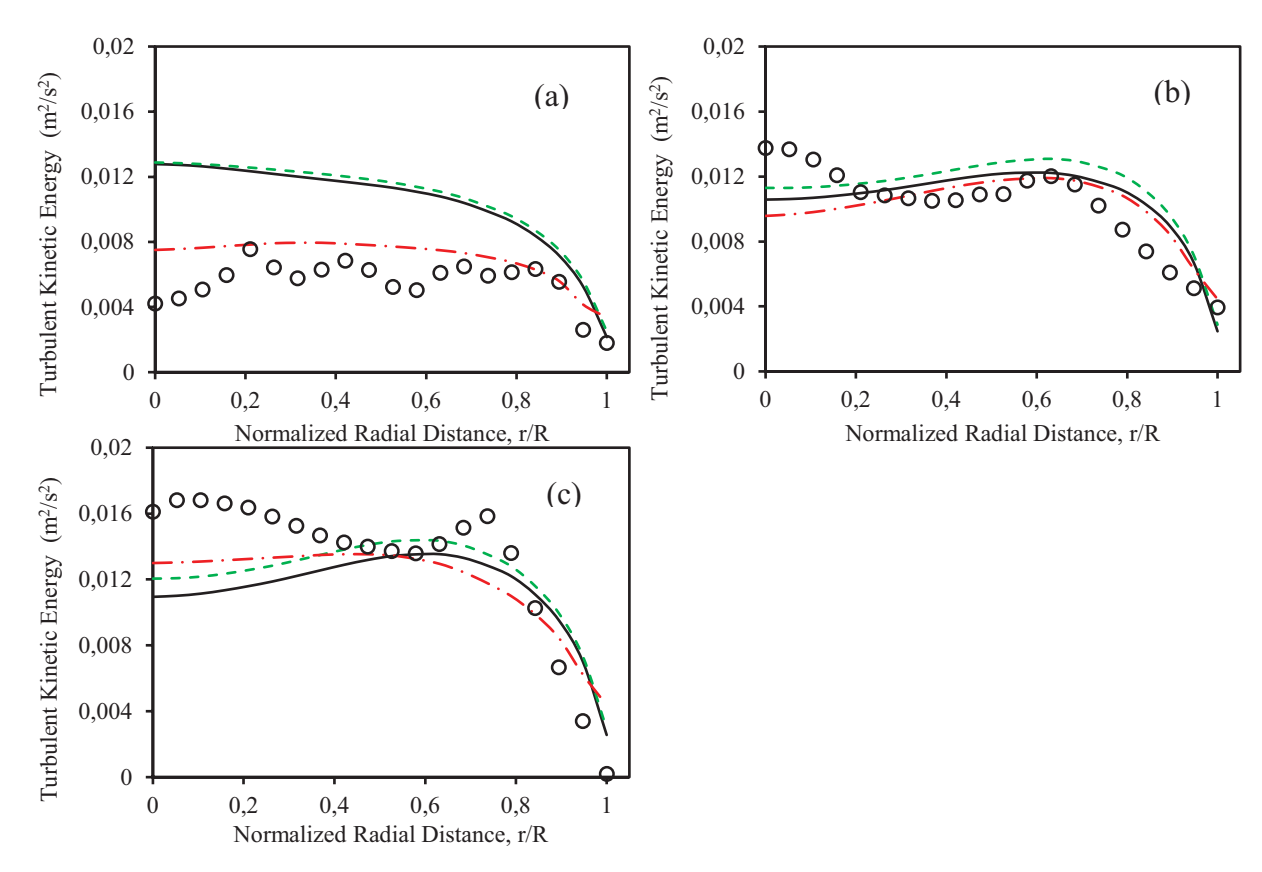


Figure 8.4: Radial profiles of the turbulent kinetic energy at different axial locations (a) h/H=0.03, (b) h/H=0.39, (c) h/H=0.75 (\circ) experimental, (\longrightarrow) Standard k- ε , (- - -) RNG k- ε and ($-\cdot$ -) RSM models

Turbulent dissipation rate

The effect of different turbulent models on the radial turbulent dissipation rate profiles at different axial locations was also investigated (Figure 8.5). The turbulent dissipation rate profile is usually low in the middle of the reactor and increases rapidly near the reactor wall. The dissipation rate is also observed to increase with an increase in axial distance from the distributor as the flow becomes more developed. All the turbulent models captured the low turbulent dissipation rate at the reactor centreline; however, a poor agreement was observed at intermediate radial locations and at the centre line. While all the models underpredicted the dissipation rate at intermediate radial locations, the RSM model overpredicted the turbulent dissipation rate at the wall while the k- ϵ based models underpredicted it. All the turbulent models failed to capture the hump observed near the region of flow reversal. Other studies have reported the difficulty in capturing this hump region (Ekambara et al., 2008).

Generally, the RNG k- ε turbulence model predicted a higher turbulence dissipation rate than the standard k- ε model. This was due to the $C_{\varepsilon 2RNG}$ term in the dissipation rate equation, which is set to a constant in the standard k- ε turbulence model. However, in the RNG k- ε turbulence model, that term is a function of the local strain rate and enables the RNG k- ε turbulence model to capture turbulence effects at different length scales (Masood and Delgado, 2014). As a result, the RNG k- ε turbulence model predicts a higher turbulent dissipation rate and a lower turbulent viscosity since the dissipation rate is inversely proportional to the induced turbulent viscosity. The effective liquid velocity consists of molecular and turbulent viscosity. Therefore, lower turbulent viscosity results in lower effective liquid viscosity which allows gas bubbles to rise faster in the liquid which leads to a high centreline liquid velocity using RNG k- ε as compared to standard k- ε (Laboude-Boutet et al., 2009). This also explains why the RSM model with the highest dissipation rate also predicted a high centreline liquid velocity.

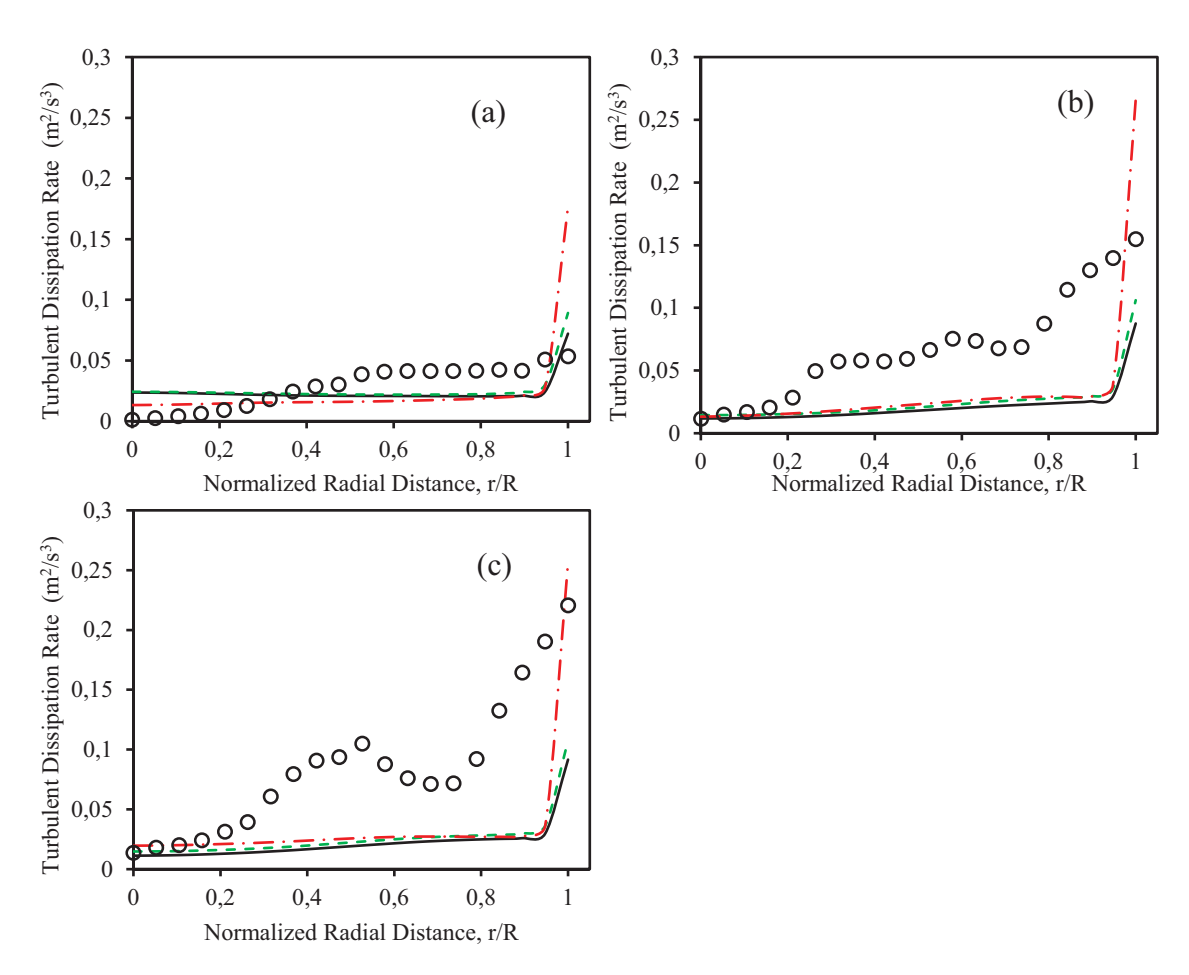


Figure 8.5: Radial profiles of the turbulent dissipation rate at different axial locations (a) h/H=0.03, (b) h/H=0.39, (c) h/H=0.75 (\circ) experimental, (\longrightarrow) Standard k- ε , (- - -) RNG k- ε and (\frown -) RSM models.

Appendix E: Effect of interfacial forces during CFD modelling

Axial liquid velocity

The effect of a combination of interfacial forces on the axial liquid velocity was also investigated. The results (Figure 8.6) show that modelling drag and lift forces resulted in a general overprediction of the axial liquid velocity near the distributor. Further up the column, the combination of drag and lift forces underpredicted the centreline axial liquid velocity while overpredicted the velocity near the reactor wall. This could be due to the high gas holdup region near the reactor wall after including the lift force (Figure 8.7). A further improvement in the prediction was observed by combining the drag, lift and wall lubrication forces. This was possibly due to the shift in the bubbles from the reactor wall to the bulk as a result of the low pressure zone created at the centre of the reactor by the fast-moving liquid.

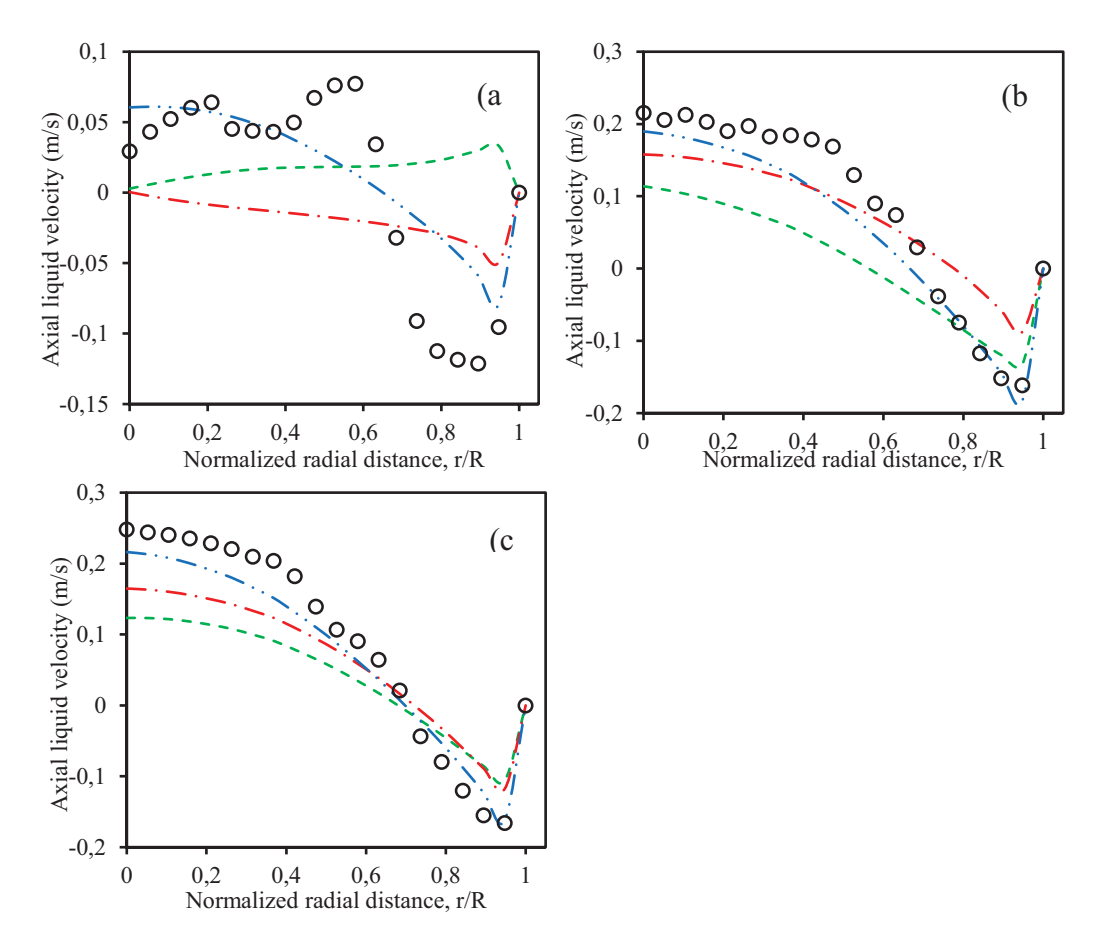


Figure 8.6: Radial profiles of the axial liquid velocity at different axial locations (a) h/H=0.03, (b) h/H=0.39, (c) h/H=0.75 (o) experimental, (- - -) Drag+Lift, (- · -) Drag+Lift+Wall lubrication, (- · · -) Drag+Lift+Wall lubrication+Turbulent dispersion.

The bubble redistribution resulted in an increase in the centreline axial velocity. The most accurate prediction was given when all the four forces (drag, lift, wall lubrication and turbulent forces) were modelled where only a slight underprediction was observed at the reactor

centreline. The addition of the turbulent dispersion force ensured that the effect of liquid turbulence on the bubble movement was captured, resulting in a more accurate liquid velocity profile.

Gas holdup

Interfacial forces modify the movement of the bubble swarm in the reactor, and this effect is most evident in the radial gas holdup profiles. The influence of a combination of different interfacial forces on the radial gas holdup profiles was investigated at different axial locations. The results (Figure 8.7) show that modelling the drag and lift forces resulted in a parabolic gas holdup profile, at the fully developed region, with an accurate simulation at the central and intermediate locations. However, using the drag and lift force resulted in an increase of the gas holdup near the reactor wall. In this work, a bubble diameter of 6 mm was specified. The lift force model of Tomiyama et al. (2002), specifies a negative lift coefficient for bubbles which are 6 mm and larger. Such a negative lift coefficient results in the movement of bubbles towards the reactor centreline; however, some bubbles remain near the reactor wall.

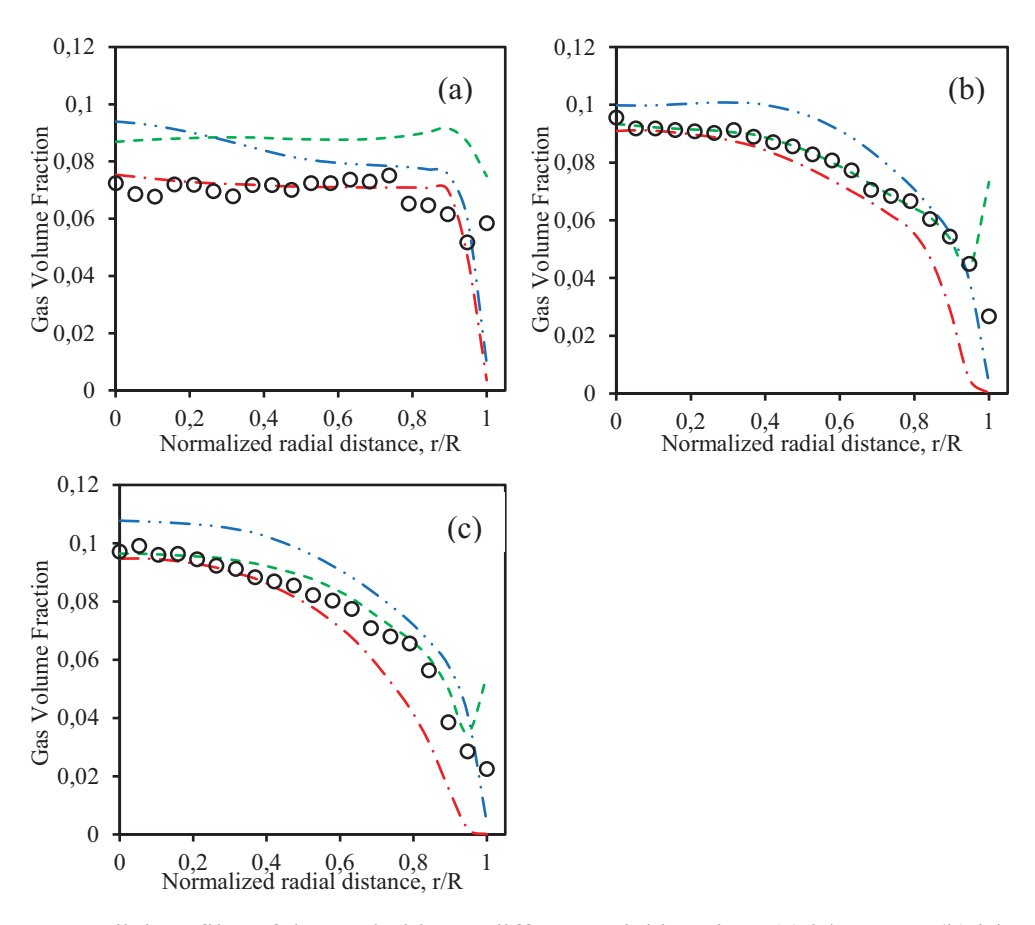


Figure 8.7: Radial profiles of the gas holdup at different axial locations (a) h/H=0.03, (b) h/H=0.39, (c) h/H=0.75 (o) experimental, (- - -) Drag+Lift, (- · -) Drag+Lift+Wall lubrication, (- · · -) Drag+Lift+Wall lubrication+Turbulent dispersion

Modelling the drag, lift, and wall lubrication forces improved gas holdup prediction near the distributor. Further up the column, the addition of the wall lubrication force to the drag and lift forces pushed the bubbles that remained near the wall towards the centreline which resulted inaccurate prediction of the gas holdup near the reactor centreline and an underprediction near the reactor wall. This can be attributed to a very strong wall lubrication force that pushed the bubbles away from the wall. Inclusion of all four forces (drag, lift, wall lubrication and turbulent dispersion forces) resulted in a general overprediction of the gas holdup at the centreline and intermediate locations, with an accurate prediction near the wall. The parabolic gas holdup profile along the radial direction was less steep as compared to the profile which was obtained using a combination of drag, lift and wall lubrication forces. This can be attributed by the tendency of the turbulence dispersion force to redistribute bubbles along the radial direction (Tabib et al., 2008).

Turbulent kinetic energy

The effect of different interfacial forces on the radial turbulent kinetic energy profiles was also investigated. The results (Figure 8.8) show that the combination of drag and lift forces generally resulted in accurate prediction of the turbulent kinetic energy at the different axial locations. However, combining drag, lift, and wall lubrication forces grossly overpredicted the turbulent kinetic energy at all locations. This can be attributed to the steep gas holdup profile predicted by this combination of forces. Further addition of the turbulent dispersion force significantly improved the prediction due to better redistribution of bubbles. The good prediction observed using drag+lift and drag+lift+wall lubrication+turbulent dispersion can be attributed to the broader distribution of gas holdup while using this combination of forces. This reduced the shear stresses, resulting in a lower turbulent kinetic energy profile.

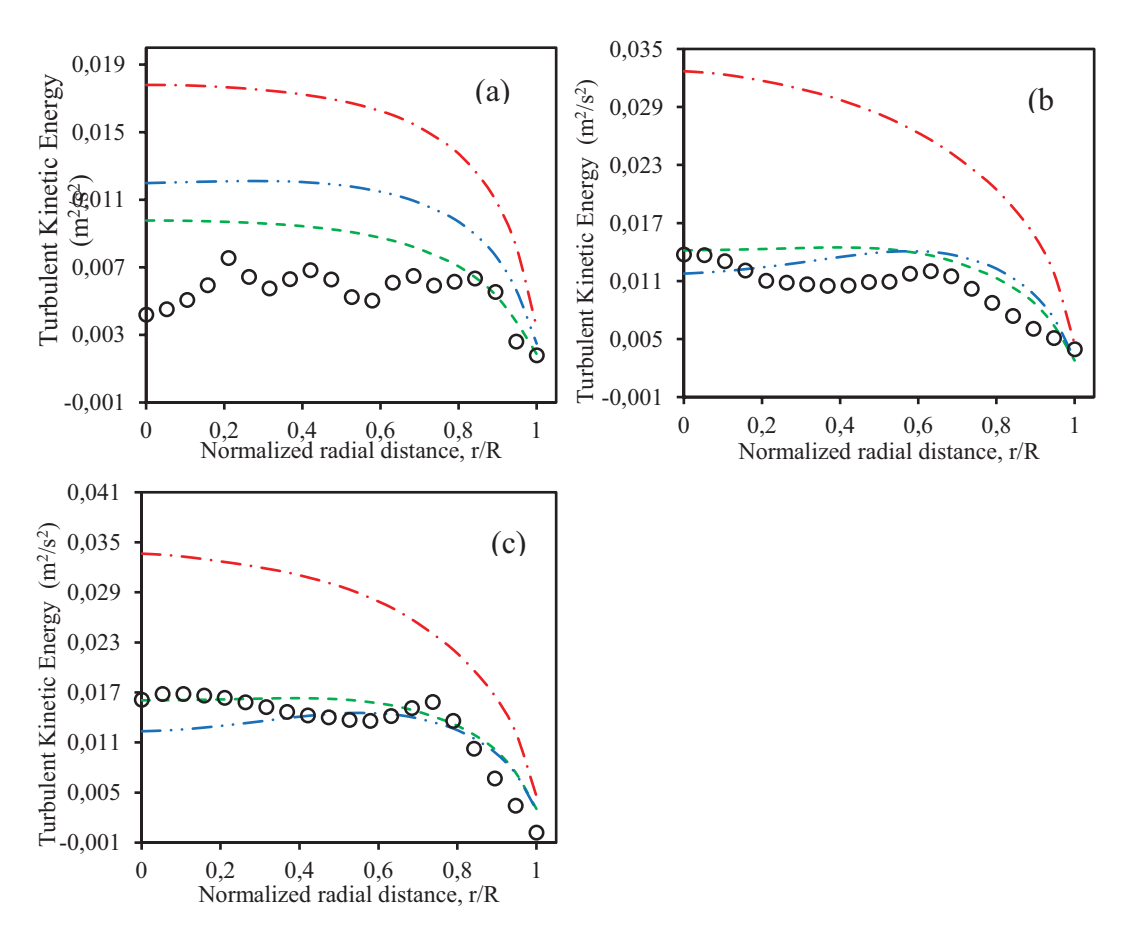


Figure 8.8: Radial profiles of the turbulent kinetic energy at different axial locations (a) h/H=0.03,(b) h/H=0.39, (c) h/H=0.75 (○) experimental, (- - -) Drag+Lift, (— · —) Drag+Lift+Wall lubrication, (— · · —) Drag+Lift+Wall lubrication+Turbulent dispersion.

Turbulent dissipation rate

The influence of the different combinations of forces on the radial turbulent dissipation rate profiles was investigated. The results (Figure 8.9) show that the turbulent dissipation rate at the centreline was predicted accurately by most of the combinations of interfacial force (except drag+lift+wall lubrication). Most of the combinations of interfacial forces, except drag+lift combination, overpredicted the turbulent dissipation rate at the wall of the reactor near the distribution. Further up the column, all other combinations of interfacial forces underpredicted the turbulent dissipation rate at the wall of the reactor except drag+lift+wall lubrication forces. The unique prediction by the combination of drag+lift+wall lubrication forces can be attributed to its relatively rapid change in gas volume fraction in the radial direction, as shown by the steep gas holdup profile. This resulted in high shear stresses.

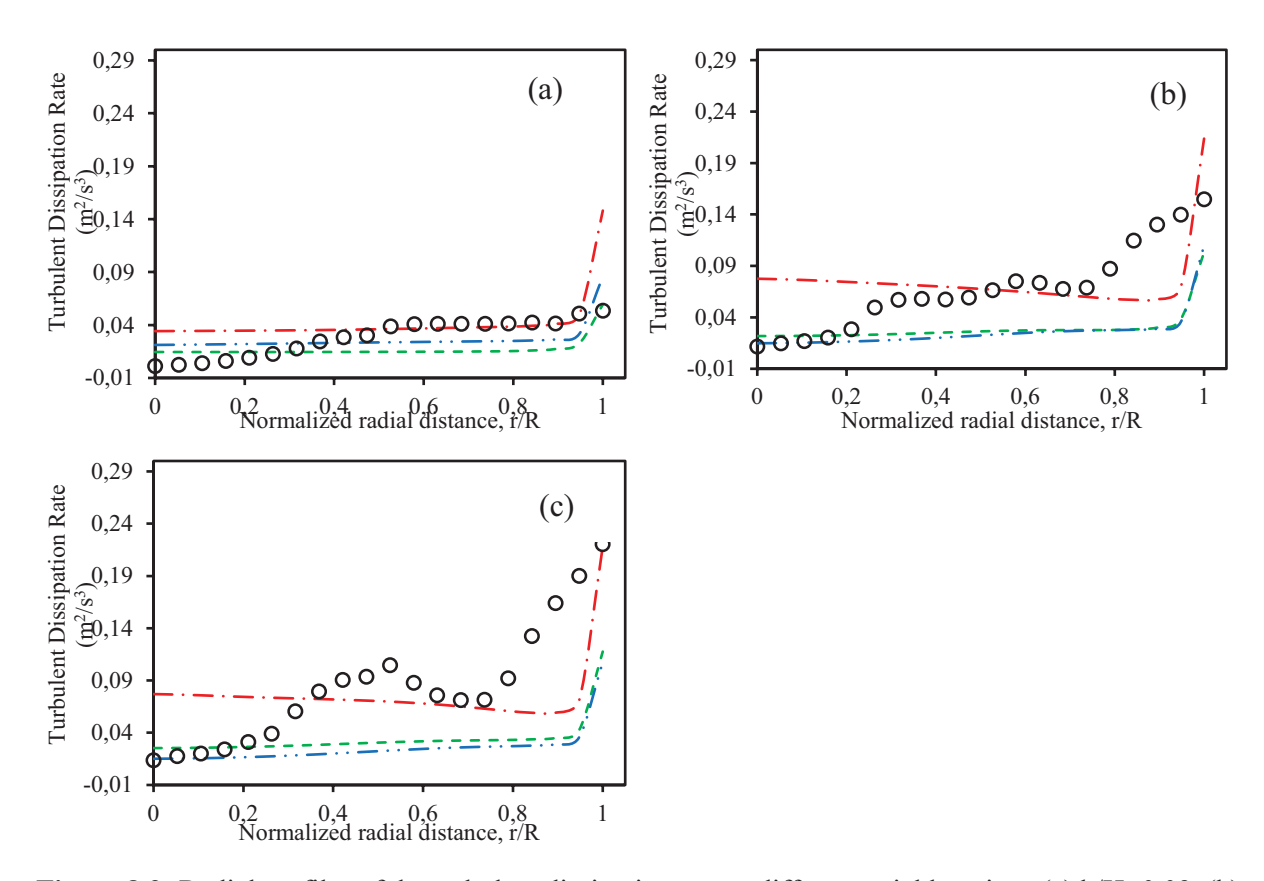


Figure 8.9: Radial profiles of the turbulent dissipation rate at different axial locations (a) h/H=0.03, (b) h/H=0.39, (c) h/H=0.75 (○) experimental, (- - -) Drag+Lift, (- · -) Drag+Lift+Wall lubrication, (- · · -) Drag+Lift+Wall lubrication+Turbulent dispersion

Appendix F: Anaerobic reaction kinetic

Kinetic parameters of anaerobic digestion

The kinetic model based on the Monod equation for the UASB reactor, without recycling biomass, can be expressed as (Hu et al., 2002);

$$\frac{dS}{dt} = \frac{Q}{V}S_o - \frac{Q}{V}S + \mu X - K_d X \tag{8.60}$$

where, K_d is the death rate (hour⁻¹). If suspended solids concentration in the influent is negligible, then dX/dt = 0 at steady state. HRT is defined as the retention time (t, hrs). Since the specific growth rate and rate limiting substrate concentration can be expressed by the Monod model, Eq. 8.60 can be combined with the Monod equation to give;

$$\frac{\mu_{max}S}{K_S + S} = \frac{1}{t} + K_d \tag{8.61}$$

To estimate the substrate concentration in the effluent at steady state, Eq. 8.61 can be rearranged as;

$$S = \frac{K_s(K_d + (\frac{1}{t}))}{\mu_{max} - K_d - (\frac{1}{t})}$$
(8.62)

The rate of change in the concentration of the substrate is given by;

$$\frac{dS}{dt} = \frac{Q}{V}(S_o - S) - \frac{\mu X}{V}$$
(8.63)

where, Y is the biomass yield coefficient (g TSS g COD⁻¹). Since under steady-state conditions, the rate of change in substrate concentration is negligible, Eq. 8.63 can be simplified to;

$$\frac{1}{t}(S_o - S) = \frac{X}{Y} \left(\frac{1}{t} + K_d\right) \tag{8.64}$$

To estimate the biomass concentration in the effluent under steady-state conditions, Eq. 8.64 can be rearranged as;

$$X = \frac{Y(S_o - S)}{(1 + K_d t)} \tag{8.65}$$

For the kinetic model based on the Contois equation, substituting the Contois equation into Eq. 8.60 instead of the Monod equation gives;

$$\frac{\mu_{max}S}{BX+S} = \frac{1}{t} + K_d \tag{8.66}$$

Substitution of Eq. 8.65 into Eq. 8.66 followed by rearranging can allow for the expression of the effluent substrate concentration at steady-state as;

$$S = \left(\frac{BY}{(\mu_{max} - K_d)t + BY - 1}\right) \times S_o \tag{8.67}$$

The kinetic parameters K_d and Y can be obtained by rearranging Eq. 8.64 as;

$$\frac{(S_o - S)}{tX} = \frac{1}{Y} \left(\frac{1}{t} \right) + \left(\frac{1}{Y} \right) K_d \tag{8.68}$$

The values of K_d and Y can be calculated from a linear plot of Eq. 8.68 from the intercept and the slope, respectively. The μ_{max} and K_s can be obtained by rearranging Eq. 8.61 as;

$$\frac{t}{1+tK_d} = \frac{K_s}{\mu_{max}} \frac{1}{S} + \frac{1}{\mu_{max}}$$
(8.69)

The values of μ_{max} and K_s , respectively, can be obtained from the intercept and the slope of a linear plot of Eq. 8.69.

Also, the values of μ_{max} and B can be determined by rearranging Eq. 8.66 as;

$$\frac{t}{1 + tK_d} = \frac{BX}{\mu_{max}S} + \frac{1}{\mu_{max}}$$
 (8.70)

A linear plot of Eq. 8.70 allows for the estimation of μ_{max} and B from the intercept and slope, respectively.

